Δ^{++} Resonance Measurements in a High Multiplicity Environment

Karim El Chenawi

Department of Physics
Lund University
1999

Δ^{++} Resonance Measurements in a High Multiplicity Environment

Karim El Chenawi
Department of Physics
Lund University, Sweden

Thesis for the degree of Doctor of Philosophy

To be presented under the auspices of the Faculty of Mathematics and Natural Sciences of Lund University and publicly defended in lecture hall B of the Department of Physics on March 4 1999, at 10.15.

Organization	Document Name
LUND UNIVERSITY Department of Physics Box 118 S-221 00 LUND, Sweden	DOCTORAL DISSERTATION
	Date of issue 18 Jan 1999
	CODEN: ISRN LUNFD6/NFFK-1016-SE-140P
Author(s) Karim El Chenawi	Sponsoring organization

Title and subtitle

Δ^{++} Resonance Measurements in a High Multiplicity Environment

Abstract

The very large multiplicity of charged particles encountered in lead on lead collisions in the WA98 experiment at the CERN SPS provided new experimental challenges. Tracking detectors read out with high granularity were developed to achieve accurate position information in two dimensions, with the aim of re-constructing tracks with a minimum of combinatorial difficulties. A tracking system based on multi-step avalanche chambers equipped with a new electronic readout system was developed and implemented in the experiment during 1996. The different aspects of the tracking system and its performance are described.

The extraction of the Δ^{++} resonance from high statistics, high multiplicity samples of FRITIOF events has been studied in order to find a reliable method to reconstruct the number of produced Δ^{++}. The first measurement on Δ^{++} production in 158 A GeV Pb+Pb collisions, using the high resolution tracking system in WA98 is presented.

Key words

pad readout, electronic, VLSI, ASIC, chip-on-board, multi-step avalanche chamber, MSAC, tracking, position resolution, efficiency, heavy-ion collisions, delta resonance, freeze-out temperature

Classification system and/or index terms (if any)

Supplementary bibliographical information	Language English
ISSN and key title 1101-4202 Cosmic and Subatomic Physics Dissertation	ISBN 91-628-3377-4
Recipient's notes	Number of pages 140 / Price
	Security classification

Distribution by (name and address)

Karim El Chenawi, Department of Physics,
Box 118, S-221 00 LUND, Sweden

Signature Karim El Chenawi Date 18 Jan 1999

This thesis is based on the following publications:

I L. Carlén et al.
Fabrication and test of a 70 000 channels electronic pad readout system for multi-step avalanche chambers
Nucl. Instr. and Methods A **413** (1998) 92-104.

II L. Carlén et al.
Performance of multi-step avalanche chambers equipped with two-dimensional electronic readout
Nucl. Instr. and Methods A **412** (1998) 361-373.

III L. Carlén et al.
A large-acceptance spectrometer for tracking in a high multiplicity environment, based on space point measurements and high resolution time-of-flight
Submitted to Nucl. Instr. and Methods A.

IV M.M. Aggarwal et al. (WA98 collaboration).
Δ^{++} abundance in 158 A GeV ^{208}Pb+^{208}Pb interactions at the CERN, SPS
To be submitted.

Preface

This thesis summarizes my four years of doctoral studies in the field of high energy heavy-ion physics. The content focuses on results obtained from my work within the WA98 collaboration.

Chapter one gives some of the necessary background on the interests in the field of high energy heavy-ion physics, the tools needed for the study and some of the terminology for the physics description. The second chapter introduces the experiment on which construction I spent most of my time during the first two years. Chapter three describes the basic steps in the analysis of the data, leading to extracted physical variables. Chapter four turns to the main physics topic in this thesis. My studies presented here, tries to find a reliable method to determine the abundance of Δ^{++} in high multiplicity data. It is shown in chapter five, that the yield of Δ^{++} can give important information on the temperature of the system created in the collisions. The results from our measurements as well as their implications are presented.

This work would not have been possible without several peoples effort and hard work. I am very grateful for all the help and support from the staff at the Division of Cosmic and Subatomic Physics. In particular, I would like to express my sincere thanks to: Professor Ingvar Otterlund for offering me the position in his team and for all his encouragement during the past four years. Sten Garpman for all his help in the development of software analysis tools. Lennart Österman, Lars Carlén and Kaj Söderström for all their efforts in the construction of the experiment.

My fellow students for the discussions about physics and everything else. Sven Lundborg for his support on our what sometimes seemed endless stays at CERN. My supervisor Hans-Åke Gustafsson, Anders Oskarsson and Evert Stenlund for their never ending help and enthusiasm in our work together.

I gratefully acknowledge the financial support from *Kungliga Fysiografiska Sällskapet i Lund*, *Knut och Alice Wallenbergs Stiftelse* and *Naturvetenskapliga Forskningsrådet.*

Finally I would like to express my deepest gratitude to my parents for their endless encouragement and understanding throughout the years.

Contents

Chapter 1

Introduction

Over the past few decades the interest in the field of high energy heavy-ion collisions has been growing. The main reason for this is the possibility of creating and studying nuclear matter under conditions of extreme temperatures and densities. It was revealed in the 1960's that the nucleons have internal structures called quarks[1]. Quarks play a fundamental role in heavy-ion interactions. In quantum chromodynamics, the theory that describes strongly interacting matter in the standard model, the nucleons are described as bound states of three valence quarks surrounded by virtual quarks and antiquarks (called seaquarks). The trapping of the quarks inside the nucleon is referred to as confinement. The quarks exchange gluons and are thus "glued together" in the form of hadrons.

Quarks carry electric as well as color charge, whereas gluons only carry color charge. There are three color charges, red, green and blue (and the corresponding anti colors). No isolated quarks have been found and will never be found if our theoretical concepts are valid. The reason for this is that the strong interaction requires that all observed states must have zero net color charge. These states can be formed by a combination of three quarks qqq with different colors or three antiquarks $\bar{q}\bar{q}\bar{q}$ with

[1]Murray Gell-Mann called these subunits quarks. He came across the word "quark" in the phrase "Three quarks for Muster Mark" in James Joyce's book Finnegan's Wake. In 1969 Gell-Mann was awarded the Nobel Prize in physics for his work on the theory of elementary particles.

different anti colors (called baryon and antibaryon respectively) or from a combination of a quark q with color and an antiquark $\bar{q}$ with anti color of the same kind (called meson).

When colliding heavy nuclei head-on at relativistic energies, a large amount of energy is deposited into a small volume during a short time-interval. The obtained high energy density could lead to the formation of a new form of matter in which the quarks and gluons are free to move within a volume much larger than the extension of a single nucleon. This is referred to as deconfinement and the new form of matter is called *Quark-Gluon Plasma*, QGP. The detection and investigation of the QGP is the ultimate goal of todays high energy heavy-ion research.

1.1 Quark-Gluon Plasma

An illustrative way of describing high energy nucleus-nucleus collisions is the space-time scenario suggested by Bjorken[1], Fig. 1.1. In this picture, the collision between the two nuclei takes place at $(z,t) = (0,0)$ where z is the longitudinal coordinate and t the time coordinate. If the energy density is sufficiently high, a quark-gluon plasma might be formed and brought to local thermal equilibrium at a proper time $\tau = \tau_0$ where τ is given by

$$\tau = \sqrt{t^2 - z^2} \tag{1.1}$$

After reaching equilibrium the plasma will go through a hydrodynamical phase where its temperature will drop and hadronization will appear at a later proper time. Using this picture as a starting point, Bjorken derived a very important relationship between the initial energy density and the rapidity density, which can be measured. Bjorken estimated the proper time τ_0 to be $\sim$1 fm/c.

According to the Big Bang model, the matter of the Universe is believed to have been in a very hot and dense state of quarks and gluons when the age of the Universe was less than 10 μs.[2] Thus the detection and studying of the QGP could give us new knowledge about conditions similar to those prevailing during the early evolution of the Universe. The method we employ today to study these extreme conditions is by

colliding heavy ions at high energies. The higher the energy we use, the further back in time we expect to be able to look.

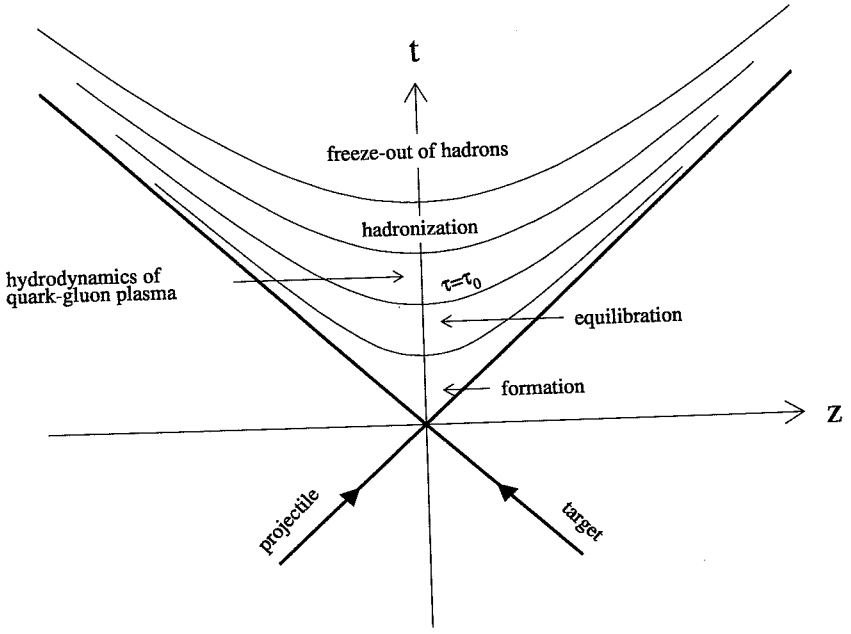

Figure 1.1: *Bjorken's space-time picture of a high energy heavy-ion collision.*

1.2 Quark-Gluon Plasma Signals

Several characteristic QGP signals have been proposed to determine if a plasma has been formed in a high energy heavy-ion collision. Some of these signals have been observed but none of them are unambiguous since they also can be obtained in hadronic scenarios under specific conditions. The final evidence for the detection of the QGP may need several of these signals to be observed in the same collision. Experiments with the capability of observing several of these signals have been proposed and

are under construction (e.g. the PHENIX experiment at the RHIC and the ALICE experiment at the LHC). Below follows a short description of some of the proposed QGP signals.

Strangeness enhancement: The strangeness content of a QGP in thermal and chemical equilibrium differs from that of nuclear matter.[3] The valence quarks of nuclear matter are up (u) and down (d) quarks, but as soon as the excitation energy becomes high enough, other quark flavors can be created. The third lightest quark after the u quark (current mass $\sim$ 5 MeV/c^2) and the d quark (current mass $\sim$ 10 MeV/c^2) is the strange[2] s quark (current mass $\sim$ 200 MeV/c^2). The presence of strange quarks is expected to be enhanced since quarks are fermions and the creation of u and d quarks are Pauli blocked due to their high concentration and due to the high Fermi energy they would have to overcome. The creation of $s\bar{s}$ pairs might therefore be energetically favorable over the creation of $u\bar{u}$ or $d\bar{d}$ pairs. Experiments both at the AGS[3] and SPS[4] have observed strangeness enhancement.[4, 5]

J/Ψ suppression: The J/Ψ particle is a bound state of a pair of charmed quarks, one quark c and one antiquark $\bar{c}$. In a quark-gluon plasma, the color charge of a quark is screened due to the presence of quarks, antiquarks and gluons, analogous to the Debye screening of an electrical charge. This screening would lead to a weaker interaction between the quarks. Also the high temperature in the plasma reduces the string tension between the quarks. Therefore if a J/Ψ particle is created in a plasma the $c\bar{c}$ pair could be separated since the interaction between them is screened. The charmed quarks might then rather combine with u or d quarks forming D-mesons which would lead to a reduction in the production rate for J/Ψ particles in high energy heavy-ion collisions. Recent results from experiments at SPS studying J/Ψ production show a strong suppression in Pb+Pb collisions which could be an indication of deconfinement.[6]

[2]They were given the name strange since they were created in strong interactions but decayed by weak interactions.

[3]Alternating Gradient Synchrotron at the Brookhaven National Laboratory (BNL) New York.

[4]Super Proton Synchrotron at the Conseil Europeen pour la Recherche Nucleaire (CERN) Geneva.

Properties of light vector mesons: The masses, widths, branching ratios and yields of light vector mesons (ρ, ω, ϕ) differs in hot, dense, strongly interacting matter from that of normal nuclear matter. This has been suggested by several authors.[7] Among these vector mesons, the ϕ-meson is of special interest. If the mass of the ϕ-meson should change, the branching ratio between the decay channels $\phi \rightarrow e^+ + e^-$ (0.0031% in normal matter) and $\phi \rightarrow \mathrm{K}^+ + \mathrm{K}^-$ (49.3% in normal matter) would change drastically. Since the mass of the ϕ-meson (1019.5 MeV/c^2) is just slightly above (32.16 MeV/c^2) the mass of two kaons (2·493.67=987.34 MeV/c^2), the ratio should be very sensitive to mass changes. An experiment measuring both these channels will be well suited to look for this effect. Such experiments are under construction (e.g. the PHENIX experiment). Since the ϕ-meson only consists of strange quarks ($\phi = s\bar{s}$) its yield could also be a signal for the plasma.

Thermal photons: Photons are suggested to be an important signal since they do not interact strongly with the plasma and thus can escape, carrying information about the early evolution of the plasma. Photons can be produced in several ways in the plasma: $q + \bar{q} \rightarrow \gamma + g$ (annihilation process), $g + g \rightarrow \gamma + q$ and $g + \bar{q} \rightarrow \gamma + \bar{q}$ (Compton processes). The photons can give information about the thermodynamical state of the environment in which they are produced, since their production rate and momentum distribution are determined by the momentum distributions of the quarks, antiquarks and gluons in the plasma. It is however a difficult task to distinguish between photons which come from the plasma (called thermal photons) and photons from all other sources. Photons can be emitted from the hadron gas (e.g. $\pi^+ + \pi^- \rightarrow \gamma + \rho^0$), parton collisions (e.g. a quark of one nucleon interacts with an antiquark of another nucleon and produces a photon and a gluon). The decay of hadrons is also a copious source of photons. For example, many neutral mesons are produced in the interactions which predominantly decay into two photons: $\pi^0 \rightarrow \gamma\gamma$ with a branching ratio of 98.8% and $\eta \rightarrow \gamma\gamma$ with a branching ratio of 39.3%. Theoretical estimates of expected yield of photons from the plasma have been made.[8] Experiments that have reported on photon yields are the WA80 and WA93 experiments[9, 10, 11] (both predecessors of WA98) and the CERES experiment[12]. Several uncertainties still have to be removed and further theoretical calculations have to be made before any strong conclusions can be drawn.

Charged hadrons: A thermodynamical model can be useful to describe high energy heavy-ion collisions.[1] In such a model, when two nuclei collide, a hot and dense fireball of nuclear matter is produced. As it expands, its temperature drops and hadronization of the plasma occurs, producing the hadrons we detect in experiments. In this picture, interesting global variables such as temperature and energy density can be calculated from the hadronic spectra. Transverse momentum (p_T) spectra for produced particles can give an estimate of the temperature of the plasma. $<p_T>$ versus the rapidity distribution (dN/dy) (two easily measurable quantities) could show a structure resulting from a phase transition.[13]

1.3 Experimental Facilities

Cosmic rays were the only source of high energy particles until accelerators became available. Many important discoveries have emerged from the studies of cosmic rays, but the advantages of using accelerators are of course numerous. Mono-energetic beams of one particle species with very high intensity can be produced. But experiments using cosmic rays are still interesting since particles with energies of more than 10^{11} GeV have been observed[14], which is far greater than any accelerator can produce today.

In Table 1.1 the most important accelerators, existing and future, for high energy heavy-ion studies are listed. One distinguishes between *fixed-target* accelerators and *colliders*. High energy ($E_{lab} > 10$ A GeV) heavy-ion experiments have been conducted at the fixed-target accelerators AGS and SPS and the colliders RHIC and LHC will be utilized in the near future.

1.4 Common Variables and Terminology

Below are some of the variables and terminology that is part of the language of high energy heavy-ion collisions presented.

Accelerator	*Beam*	$\sqrt{s}$ [A GeV]	*Startup year*
AGS, BNL	^{16}O, ^{28}Si	5.4	1986
	^{197}Au	4.4	1992
SPS, CERN	^{16}O, ^{32}S	19.4	1986
	^{208}Pb	17.4	1994
RHIC, BNL	^{197}Au	200	1999
LHC, CERN	^{208}Pb	5500	2005

Table 1.1: *Accelerators for current and future studies of high energy heavy-ion collisions.*

Heavy-ion collisions are divided into different event classes depending on the centrality of the collision. It can experimentally be determined in different ways. The transverse energy E_T, measured by a calorimeter is one way of determining the centrality. Transverse energy measured by a calorimeter is experimentally defined as

$$E_T = \sum_{i=1}^{N} E_i \cdot sin(\theta) \tag{1.2}$$

The index i runs over the number of calorimeter modules, and E_i is the energy measured by a module placed at an angle θ relative to the beam axis.

To be able to compare data from different centrality classes with models and other experiments, the transverse energy measurement must be translated into some variable which means the same independent of which model or experiment we wish to compare with. The quantity used is the impact parameter b, which is the transverse distance between the two centers of the colliding nuclei, as shown in Fig. 1.2. If we assume that the target nuclei are uniformly distributed and that we have a thin target so that the likelihood of one target nucleus shadowing another is low, the number of target nuclei per unit area seen by the beam is $\rho_N \cdot d$, where ρ_N is the number of target nuclei per unit volume and d the target thickness. The probability of one beam particle interacting

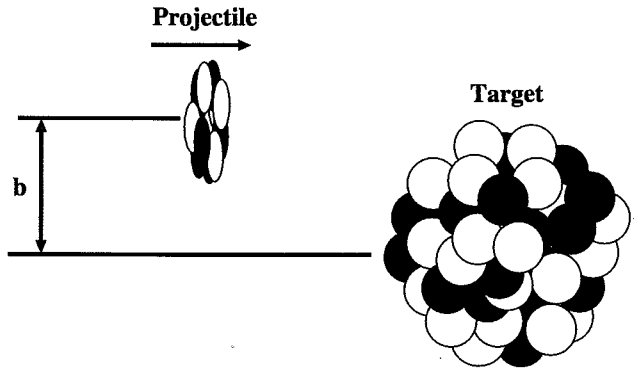

Figure 1.2: *Schematic drawing of a collision between two nuclei in a fixed target experiment. The projectile is drawn pancake-like to indicate the Lorentz contraction. The transverse distance between the two centers is called the impact parameter b.*

in the target P_{int}, can then be written as

$$P_{int} = \rho_N \cdot d \cdot \sigma_{int} \tag{1.3}$$

where σ_{int} is the interaction cross section. P_{int} can also be expressed in the quantities we measure in the experiment, the number of beam interactions in the target, N_{int} and the number of beam particles, N_{beam} as

$$P_{int} = \frac{N_{int}}{N_{beam}} \tag{1.4}$$

To calculate the minimum bias cross section σ_{mb}, N_{int} and N_{beam} is taken from the number of minimum bias triggers and the number of beam triggers respectively, obtained from the trigger system (see Chapter 2.2 for the WA98 trigger system). To obtain the total cross section σ_{tot}, a Glauber model[15] calculation can be used. Assuming a monotonic relationship between b and E_T, we can transform our $(d\sigma/dE_T)_{mb}$ spectrum and obtain the corresponding impact parameter b, for any chosen percentage of σ_{tot}.

The longitudinal rapidity of a particle is a useful quantity given by

$$y = \frac{1}{2} ln \frac{1+\beta_z}{1-\beta_z} \tag{1.5}$$

where β_z is the velocity of the particle along the beam axis. Rapidity can thus be treated as a relativistic measure of the 'velocity' of the particle. The 'normal' velocity is not a very good quantity since a large change in energy and momentum of the particle results in a small change in velocity. Rapidity can be either positive or negative. The rapidity of a particle in one frame of reference is related to the rapidity in another Lorentz frame of reference by an additive constant. The rapidity can also be expressed in terms of the total energy E and the momentum of the particle along the beam axis, p_z as

$$y = \frac{1}{2} ln \frac{E+p_z}{E-p_z} \tag{1.6}$$

The rapidity coincides with the pseudorapidity, given by Eq. 1.7, when the momentum is large, $|\bar{p}| \simeq E$ or when the mass of the particle is low relative to its transverse momentum and can be ignored.

$$\eta = \frac{1}{2} ln \left(\frac{|\bar{p}|+p_z}{|\bar{p}|-p_z}\right) \tag{1.7}$$

The pseudorapidity can also be expressed in terms of the angle between the particle momentum an the beam axis as

$$\eta = -ln[tan(\frac{\theta}{2})] \tag{1.8}$$

Another important quantity in this thesis is the invariant mass of a set of N particles defined by

$$M_{inv}^2 = E^2 - \bar{p}^2 \tag{1.9}$$

where

$$E = E_1 + E_2 + ... + E_N, \qquad \bar{p} = \bar{p}_1 + \bar{p}_2 + ... + \bar{p}_N \tag{1.10}$$

It is called invariant since it can be shown that it has the same value in any frame of reference.

Chapter 2

The WA98 Experiment

The fixed target experiment WA98[16] at the CERN SPS was proposed as a successor to the WA93 experiment. WA98 was a large acceptance spectrometer for high statistics measurements of hadrons and photons in Pb+Pb collisions at 158 A GeV. The aim was to study highly excited and compressed nuclear matter and to look for a possible phase transition to the Quark Gluon Plasma. Since WA98 measured both multiplicities of charged particles and photons, possible fluctuations in the yield of charged particles or photons could be detected simultaneously. Event-by-event, the N_γ/N_{charge} ratio could be formed to look for events with an excess of photons which could signal a plasma formation or be used as a trigger to look for other signatures in E_T, p_T etc. in very special interactions. The 10 000 module lead glass calorimeter provided high precision data on neutral pions and eta mesons at midrapidity and determination of the thermal photon to neutral pion ratio. WA98 ended its data taking in November 1996 but the analysis of data is still actively going on.

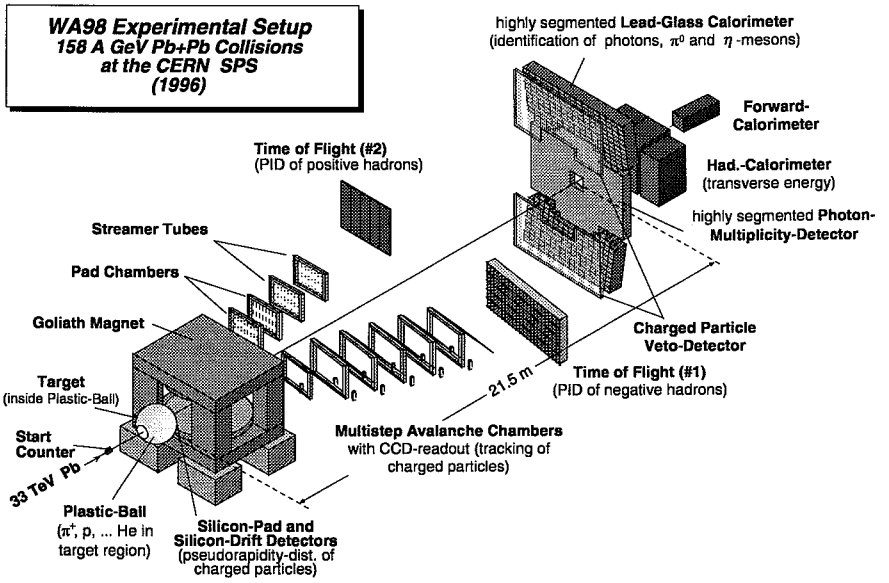

Figure 2.1: *View of Experiment WA98.*

2.1 Overview of Detectors in WA98

Starting upstream where the beam enters the experiment area from the left in Fig. 2.1 was the start-counter[17], located 3.5 m upstream of the target. The start-counter was a Cherenkov detector with Nitrogen gas as the radiator and Photo-Multiplier-Tube (PMT) readout. The intrinsic time resolution was 30-40 ps and its purpose was to count the number of beam particles traversing it and to provide a start signal for the Time-Of-Flight (TOF) measurements. To reject any interactions upstream of the start-counter and in the start-counter itself, a halo detector and veto-counter (not shown in Fig. 2.1) were utilized in anti-coincidence with the signal from the start-counter. They consisted of a set of scintillators with a hole for the beam to pass through. The halo detector was located at a distance of 5.7 m and the veto-counter 2.7 m upstream of the target.

The target was located at the center of the Plastic Ball spectrometer[18]. The Plastic Ball consisted of 655 $\Delta E - E$ modules arranged in a sphere. It detected and identified light charged particles and ions (π,p,d,t,^{3}He) in the angular range $30^o \leq \theta \leq 160^o$ with full azimuthal coverage. The corresponding coverage expressed in pseudorapidity was $-1.7 \leq \eta \leq 1.3$. Plastic Ball has been used for reaction plane determination and to study the directed flow of protons and π^+ in 158 A GeV Pb+Pb collisions.[19] Before being a part of WA98, this detector was used at the Bevalac in the Plastic Ball experiment to study collective flow.[20]

The Silicon Pad Multiplicity Detector (SPMD)[21] located 32.8 cm downstream of the target, measured the multiplicity of charged particles in the rapidity interval $2.35 \leq \eta \leq 3.75$ with full azimuthal coverage. This interval overlapped with the interval covered by the photon multiplicity detector to enable an event-by-event measurement of N_γ/N_{charge}. The measured efficiency in test beam of detecting a charged particle was better than 99%. Since only 0.2% of the photons were expected to interact in the silicon, it was very transparent to photons coming from the collision region.

Two Silicon-Drift Detectors, (SDDs) placed 8.0 and 35.7 cm downstream of the target respectively, measured the multiplicity and pseudorapidity of charged particles. They covered the pseudorapidity interval $1.50 \leq \eta \leq 4.55$ and overlapped with the interval covered by the photon multiplicity detector.

The Goliath dipole magnet, was operated with a bending power ($\int Bdl$) of 1.6 Tm, bending particle trajectories horizontally into the two tracking arms. The field was mainly set to bend positively charged particles into the left tracking arm in Fig. 2.1, but a smaller amount of data was also taken with reversed field and field off.

The first tracking arm consisted of six Multi-Step Avalanche Chambers (MSACs)[22, 23, 24, 25] with CCD camera readout together with a TOF wall. The first chamber was located 3.4 m from the center of the magnet, and the last at 9.4 m. The momentum resolution $\Delta p/p$ was, in per cent, approximately given by $2.7p - 2.2$. The TOF wall allowed particle identification of π,K,p with a time resolution of $\sigma_t \simeq 120$ ps.

The second tracking arm was implemented late (fall 1996) in the experiment. The motivation for the construction of a second tracking arm was primarily to study the ϕ-meson production through the decay channel $\phi \rightarrow K^+ + K^-$ (one of the proposed signals of a plasma formation, see Chapter 1.2). Fine granularity and good two track resolution chambers in combination with a new TOF wall were constructed to deal with the high particle density. The final configuration of the second arm consisted of two MSACs with pad readout, two planes of streamer tube detectors with pad readout and a TOF wall, $\sigma_t \simeq 90$ ps. The TOF wall was originally designed for the PHENIX experiment at the BNL and its usage in WA98 was the first full scale operation. The momentum resolution $\Delta p/p$ was, in per cent, approximately given by $0.40p + 0.21$. The development and construction of, the second tracking arm, was the main contribution from the Lund group to WA98. The development of the new pad readout concept for the MSACs and the streamer tube detectors is described in detail in paper I. The performance of the MSACs equipped with this pad readout is described in detail in paper II and the performance of the whole tracking arm is described in detail in paper III. A signal studied with the second tracking arm is the Δ^{++} resonance in the decay channel $p\pi^+$, described in paper IV.

The Photon Multiplicity Detector (PMD)[26], located 21.5 m downstream of the target, measured the multiplicity of photons N_γ. It was divided into four quadrants which were symmetrically placed around the beam-pipe. Each quadrant consisted of a 17 mm thick lead converter plate with plastic scintillator pads behind it detecting the shower electrons. The light from the pads (a total of 41 800) were read out with the technique of image intensified CCD cameras. The acceptance in pseudorapidity was $2.8 \leq \eta \leq 4.4$. As mentioned above, this is part of the interval covered by the SDDs. The PMD has together with the information from SPMD studied possible fluctuations in the N_γ/N_{charge} ratio, on an event-by-event basis, to search for disoriented chiral condensates.[27]

One of the main components of the experiment was the Lead Glass Calorimeter (LGC)[28]. This detector was designed to cover the p_T range from 0.7 to 4.5 GeV/c. This range in p_T was chosen based on calculations of the thermal photon production from a possible QGP formation.[29] The detector consisted of 10 000 modules of lead-glass

arranged in two halves, one above and one below the PMD. The coverage in pseudorapidity was $2.28 \leq \eta \leq 2.95$ corresponding to an angular range of $6^o \leq \theta \leq 11.6^o$. The LGC has reported on neutral pion production and has observed a saturation of the $<p_T>$ for large system size.[30] The LGC will also (like the TOF wall in the second tracking arm) be used in the PHENIX experiment at BNL.

In front of the LGC halves, two planes of streamer tube detectors[31] with pad readout were placed. They served as a charged particle veto detector improving the reconstruction of photons in the LGC. The design and readout were the same as for the two planes of streamer tube detectors used in the second tracking arm (except for the pad size and tube length).

The Zero Degree Calorimeter (ZDC) measured the forward flux of energy at angles less than 0.3 degrees relative to the beam. The ZDC consisted of layers of lead sandwiched with plastic scintillators.

The Mid-Rapidity Calorimeter (MIRAC)[32], measured the transverse energy flow. It consisted of 180 calorimeter modules, each module measuring the energy of particles entering it. The modules were made of layers of lead for the electromagnetic part and layers of iron for the hadronic part, sandwiched between sheets of plastic scintillator. The detector response was linear within 2% for incident electrons in the momentum range 10-50 GeV/c and linear within 4% for incident pions in the momentum range 4-50 GeV/c. The MIRAC proved to be an effective trigger selector for central events.

2.2 The WA98 Trigger System

To determine the degree of violence in the collisions a trigger system in WA98 was utilized dividing the events into four centrality classes called *central*, *not-so-central*, *peripheral* and *minimum bias* trigger.[33] During the 1996 lead run the trigger was formed using the information from the following detectors: The halo detector, the start-counter the veto-counter and the MIRAC. A valid beam trigger was defined as

$$\overline{halo} \cdot start \cdot \overline{veto}$$

This means that there should be a valid signal in the start-counter in anti-coincidence with any signal from the halo detector and the veto-counter ensuring that no interaction took place upstream of the start-counter, or in the start-counter itself. Together with a valid beam trigger the physics trigger is then formed by using the logic given in Table 2.1. E_T is the online measurement of the transverse energy defined by Eq. 1.2.

Trigger	Logic
central	$E_T^{high} \cdot E_T^{intermediate} \cdot E_T^{low}$
not-so-central	$\overline{E_T^{high}} \cdot E_T^{intermediate} \cdot E_T^{low}$
peripheral	$\overline{E_T^{high}} \cdot \overline{E_T^{intermediate}} \cdot E_T^{low}$

Table 2.1: *The WA98 trigger logic.*

The data presented in this thesis is taken from the *central* trigger sample. Figure 2.2 shows the raw E_T distribution for this centrality class. The E_T distribution can offline be checked against the ZDC distribution for consistency.

To calculate the minimum bias cross section, the method described in Chapter 1.4 is used. However, the number of interactions must be corrected for background contributions such as interactions in the target frame, beam pipe etc. This is achieved by rescaling the number of interactions obtained from a target out run with the same run conditions and correcting the number of interactions as (using the notation from Chapter 1.4)

$$N_{int}^{Corrected} = N_{int} - N_{int}^{no\ target} \cdot \frac{N_{beam}}{N_{beam}^{no\ target}} \tag{2.1}$$

For ^{208}Pb+^{208}Pb we obtain $\sigma_{mb} \simeq 6451$ mb for a typical run corrected for target out and with the magnet turned on. A Glauber calculation gives the total cross section, $\sigma_{tot} = 7360$ mb for ^{208}Pb-^{208}Pb collision.[34] In the WA98 experiment as in many other experiments, the 10% most

central collisions (10% of σ_{tot}) are said to belong to the *central trigger*. This corresponds to an impact parameter of $b = 0 - 5$ fm, obtained from the Glauber calculation. This range in b is used in the simulations described in Chapter 4.3 to select central collisions. The corresponding range in E_T is $E_T \geq 326$ GeV. This E_T criterion is used together with the hardware trigger to differentiate between the central and not-so-central events in the analysis.

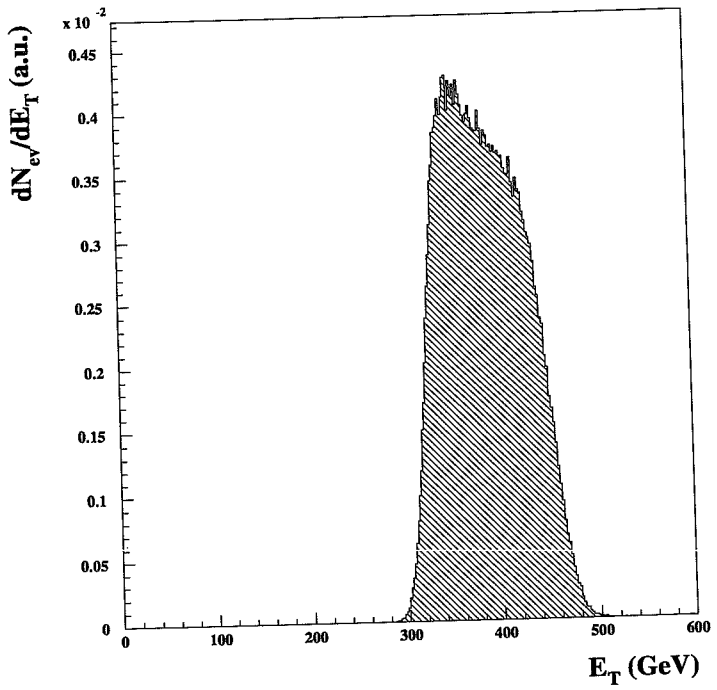

Figure 2.2: *The transverse energy distribution measured by MIRAC for the hardware centrality class central used during the lead-run 1996. The collection of central events was favored by scale-down of the other centrality classes during data taking.*

Chapter 3

Data Analysis

We will discuss the most important steps in the process of analyzing data from the second tracking arm in the WA98 experiment. The reconstruction of hit positions in the tracking planes, the track and momentum reconstruction. Particle identification and acceptance for the different particle species will be described. The different aspects of the performance of the system is described in detail in papers I, II and III.

3.1 Hit Reconstruction

The first step in the analysis is to process the raw data from the four tracking planes (two MSACs and two planes of streamer tube detectors) and the TOF wall to obtain the position of hits. A hit is defined as a collection of two or more fired adjacent pads (cluster) in the MSACs and as one or more fired pad in the planes of streamer tube detectors. A pad is defined as fired when its ADC-value is above the set threshold value. The threshold value of each channel is determined online from the pedestal distributions. The coordinates of the hit (x, y) in the MSACs are then calculated as the weighted average over the N pads in the

cluster with the pad positions (x_i, y_i) and ADC-values ADC_i as

$$x = \frac{\sum_{i=1}^{N} x_i \cdot ADC_i}{\sum_{i=1}^{N} ADC_i}, \qquad y = \frac{\sum_{i=1}^{N} y_i \cdot ADC_i}{\sum_{i=1}^{N} ADC_i} \tag{3.1}$$

In the streamer tube detectors, the hit coordinate in x is given by the wire position (see Fig. 3 in paper III) and in y by Eq. 3.1.

The TOF wall consisted of 480 vertical scintillator bars with PMT read-out in each end, giving a total of 960 channels. The x-position of a hit in the TOF wall is simply given by the bar position, and the y-position relative the center of the bar is calculated from

$$y = \frac{v}{2}(t_{up} \cdot c_{up} - t_{down} \cdot c_{down}) \tag{3.2}$$

where t_{up} and t_{down} are the times measured by the upper and lower PMTs of the bar (including the time-of-flight), v is the velocity of light in the scintillator and c_{up} and c_{down} are the time calibration constants for each PMT. After obtaining the hit coordinates for all four tracking planes together with the xy-information from the TOF wall, tracks can be reconstructed. Outside the magnetic field the particles are assumed to travel in straight line trajectories. We require that a track has to consist of hits in at least three of the four tracking planes. The xy-information from the TOF wall is not used in the tracking algorithm but included for particle identification.

3.2 Track and Momentum Reconstruction

The tracking algorithm connects the reconstructed hits from the four tracking planes by means of straight line fits. Since the number of hits in each tracking plane is of the order of 30 (see Fig. 3.2), fitting all possible combinations of hits would give 30^4 least-square fits which would be unacceptable in terms of computer time considering the amount of data to be analyzed. Therefore, to reduce the number of trial fits, all hits in plane i (i=1,2) were combined with all hits in plane j such that $i + 2 \leq j \leq 4$ (which yields the combinations: 1-3, 1-4, 2-4). For each combination, a search is performed in plane k such that $i+1 \leq k \leq j-1$

for hits within seven times the typical plane resolution, from the line combining i and j. When a hit is found, the combination of hits is kept as a track candidate. The track candidates are then fitted to the hits by minimizing the χ^2 function

$$\chi^2 = \sum_i \frac{(w_i - w(z))^2}{\sigma_i^2} \tag{3.3}$$

where w_i is the measured x_i or y_i and $w(z)$ is $x(z) = a_x z + b_x$ or $y(z) = a_y z + b_y$ and σ_i is the standard deviation for each x or y.

Since the magnet mainly bends the particles in the xz-plane and real tracks have to point to the target in the yz-plane, a cut in y at $z = 0$ is made. Together with a cut in χ^2, this reduced the number of tracks significantly, mainly due to tracks formed by false combinations of three planes hits. The remaining tracks are then ordered after the number of hits in the fit and the χ^2. Finally, tracks which share hits with a higher order track are rejected.

This tracking method proved to be very successful in finding the real tracks based on a full GEANT[35] simulation taking into account the resolution and efficiency of each plane and the multiple scattering in the air between the magnet and the tracking planes (see paper III). With the knowledge of the trajectory of each particle and the magnetic field, the momentum is determined by *the Tchebycheff method* described in detail elsewhere.[36]

3.3 Cuts to Clean up Data

To reject double-beam particles (two Pb ions within the same time window of the start-counter) and particles with charge less than Pb, an offline event-cut on the start-counter ADCs was applied. Figure 3.1 shows a scatter plot of the amount of light measured by the up and down PMTs of the gas Cherenkov start-counter. The solid rectangle in the figure indicates the applied cut. At the actual beam intensity of $3{\cdot}10^5$ ions/s, and a gate width of 100 ns, this cut rejected about 4% of the events. A cut in the start-counter TDCs was also applied to re-

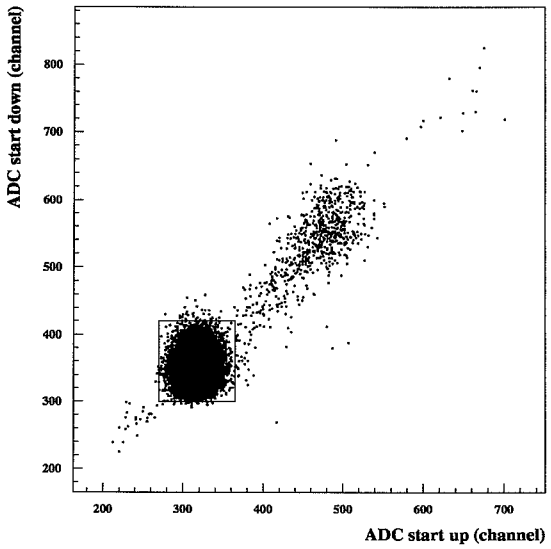

Figure 3.1: *Scatter plot of the ADC values of the up and down start-counter.*

ject overflows and underflows (caused by problems with start and stop signals), this cut rejected about 16% of the events.

Figure 3.2 shows the number of reconstructed hits in the second MSAC versus the first MSAC for *central* trigger sampled over several runs. There is a strong correlation between the two as expected, but there is also a substantial amount of entries where only one of the chambers is sensitive. This inefficiency is caused by the time it takes for a chamber to restore its electric field for full efficiency after a spark. This is discussed in more detail in paper II where also the number of found tracks as a function of the time after a spark is shown (Fig. 6 in paper II). In this plot it is evident that events collected during the first 500 ms after a spark, should be removed from the analysis. By using the spark information and online clock information written on the data tape, this can be done.

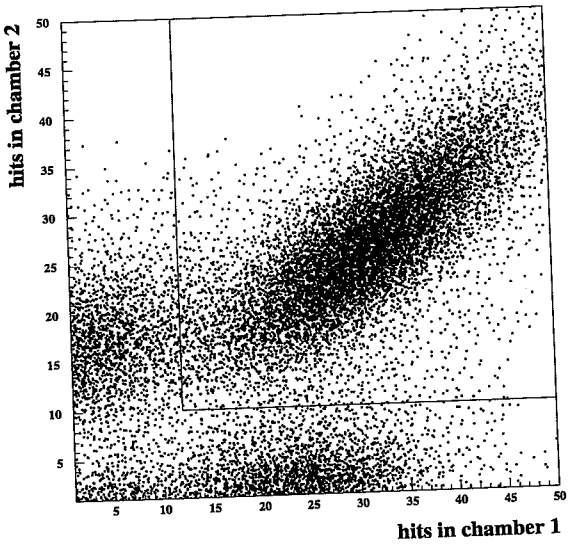

Figure 3.2: *Number of hits in chamber two versus number of hits in chamber one for central collisions.*

An alternative way of obtaining the rejection of events with only one MSAC sensitive, is to make a cut directly in Fig. 3.2. This is indicated by the two solid lines below which no events are accepted in the analysis. This cut can only be done for *central* trigger.

3.4 Particle Identification

The last step in the basic analysis of data is to assign particle identity to the reconstructed tracks. One way of doing this is to study the difference between the measured time in the TOF wall and the expected time assuming the mass of one of the possible particles. Starting with the relativistic relationship

$$p = m_0 \beta c \gamma \tag{3.4}$$

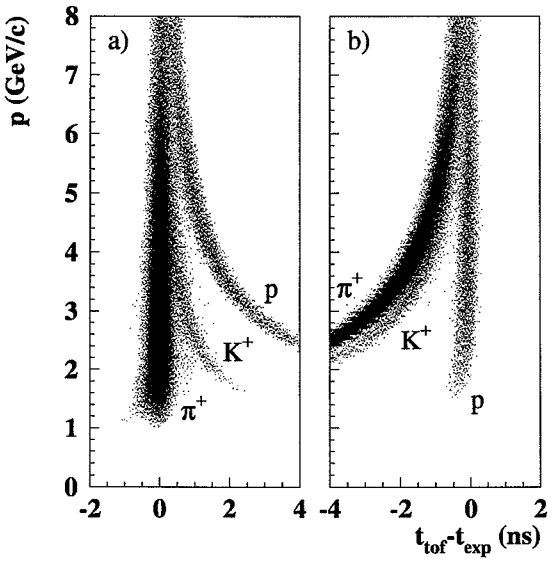

Figure 3.3: *The difference between the measured TOF and the expected TOF assuming the mass of a) pion and b) proton.*

which can be rewritten in terms of the expected flight time t_{exp}, the path length L and the momentum p as

$$t_{exp} = \frac{L}{c}\sqrt{1 + (\frac{m_0 c}{p})^2} \tag{3.5}$$

we can calculate $\Delta_{tof} = t_{tof} - t_{exp}$ where t_{tof} is the measured flight time of the particle and plot the momentum versus Δ_{tof} assuming the mass of either a pion or a proton, see Fig. 3.3. In this plot it is straightforward to assign a particle identity since the separation between the different particle species, especially pions and protons, is good over a wide range of momenta. The advantage of making the particle identification in this plot and not in e.g. a momentum versus mass plot, is that Δ_{tof} is independent of the momentum, whereas the error in the mass resulting from an error in the timing measurement is nonlinear and depends on the momentum.

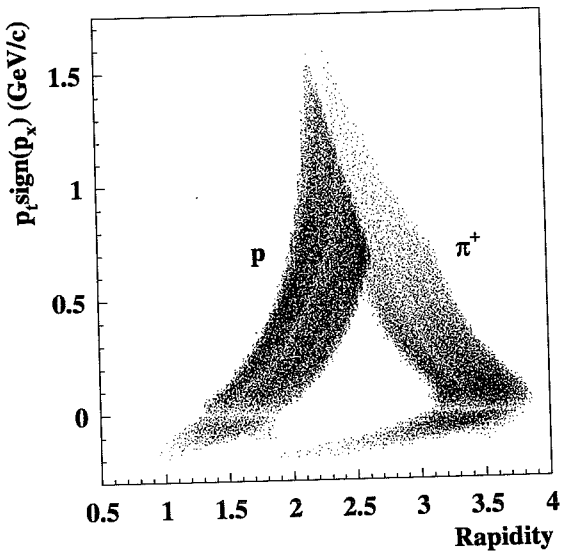

Figure 3.4: *The acceptance for protons and pions in terms of transverse momentum and rapidity.*

3.5 Acceptance

Figure 3.4 shows the acceptance in terms of rapidity and transverse momentum for the identified pions and protons. Note that p_t is multiplied with the sign of p_x. In this way, the particles, with a low enough momenta to bend over the beam line into the acceptance are clearly seen. Also seen in Fig. 3.4 is the limited overlap in phase space between p and π^+ which limits the study of ratios between the yield of different particles. But the ratio between the yield of the same particles with opposite charge is possible with the use of data with the magnetic field reversed.

Chapter 4

Studies on $\Delta(1232)$ Production

A central problem in high energy heavy-ion experiments is to determine the temperature of the system formed in the collisions. If the system reaches thermal equilibrium and a thermodynamic model is applied, the temperature can be deduced from the slopes of the transverse momentum spectra of different particle species. There are however several complications in interpreting the results from these studies. If flow is present, acceptable fits can be obtained for a range of temperatures and flow velocities. Also, since the hot dense matter formed, expands and cools before freeze-out when the particles leave the system and finally are detected, we have to extrapolate back to the early collision phase. There is a lot of work being done on this subject to try to understand what the measurements really say about the temperature. The results from these studies will not be discussed here. Instead we conclude that it is of great interest to obtain an independent measurement of the temperature at freeze-out, than what comes out from the slopes of the particle spectra. If thermal equilibrium is assumed, it has been suggested that from the ratio $\Delta(1232)$/nucleons, the temperature of the system can be determined.[37] It is therefore of great interest to determine the abundance of $\Delta(1232)$.

4.1 The Δ(1232) Resonance

The direct detection of the Δ(1232) resonance is impossible due to its short lifetime ($\tau \sim 10^{-23}$ s), instead we reconstruct the Δ(1232) by measuring its decay products, N+π. The Δ(1232) has four isospin states, $\Delta^{++}, \Delta^{+}, \Delta^{0}$ and Δ^{-}. The fraction of Δ(1232) decaying into a nucleon and a pion is > 99% and the different isospin states decay according to

$$\begin{aligned}
\Delta^{++} &\rightarrow 1(p+\pi^{+}) \\
\Delta^{+} &\rightarrow \tfrac{2}{3}(p+\pi^{0}) + \tfrac{1}{3}(n+\pi^{+}) \\
\Delta^{0} &\rightarrow \tfrac{2}{3}(n+\pi^{0}) + \tfrac{1}{3}(p+\pi^{-}) \\
\Delta^{-} &\rightarrow 1(n+\pi^{-})
\end{aligned}$$

Using the tracking arms of WA98, the Δ^{++} and Δ^{0} resonances are possible to reconstruct. Of these two, the most favorable to detect is the Δ^{++} since > 99% decays into a pπ^{+}-pair whereas the Δ^{0} goes undetected in two thirds of the cases. Higher lying resonances such as N(1440) and N(1535) which can decay into a pπ^{-}-pair could also disturb the reconstruction of Δ^{0}. Worth mentioning is that the Δ^{+} could possibly be reconstructed in the pπ^{0} decay channel using the second tracking arm together with neutral pions reconstructed by the lead glass calorimeter. But based on the arguments above, the production of Δ^{++} was investigated using data from the second tracking arm (see Chapter 5).

The Δ^{++} resonance is very hard to reconstruct in heavy ion collisions due to the high combinatorial background of uncorrelated pπ^{+}-pairs and the broad width of the Δ^{++}. Also, the peak value of the invariant mass distribution for the combinatorial background (uncorrelated pπ^{+}-pairs) is almost the same as for real Δ^{++}. To be able to extract the amount of correlated pπ^{+}-pairs (Δ^{++}) we need to subtract the combinatorial background from the invariant mass distribution. The combinatorial background can not directly be determined from data and therefore the technique of mixed events is used to describe the combinatorial background. This is schematically illustrated in Fig. 4.1, where the Δ^{++}

resonance (given the abundance as expected from simulations) is indicated as the grey area sitting on top of the spectrum of $p\pi^+$-pairs produced in the same event, which we call *Data*. This spectrum can not by the eye be distinguished from the spectrum of $p\pi^+$-pairs from the mixed event sample, which we call *Mix*.

4.2 Reconstruction Methods

To find a method to reliable reconstruct the number of produced Δ^{++}, high statistics samples of FRITIOF[38] events were generated, where the number of Δ^{++} given by FRITIOF was compared with the number obtained from different reconstruction methods.

Tail method: Here the two spectra *Data* and *Mix* are normalized in the high mass tail region, i.e. above some invariant mass cut, M_{cut}. M_{cut} has to be chosen with caution. If it is chosen too low, the Δ^{++} peak itself will influence the normalization, and if it is chosen too high, the lack of statistics will produce a too large error on the reconstructed number.

Rescale method: Here, the normalization is made over all masses. When subtracting *Data* from *Mix* normalized to the same content, the Δ^{++} peak is slightly positive above a negative background. The area of the positive Δ^{++} peak is calculated and subtracted from *Data* before a new normalization is performed. This procedure is repeated iteratively until the reconstructed number has converged.

Fitting method: Here it is assumed that the *Data* distribution is composed of a correlated part which should follow the shape of a modified Breit-Wigner distribution and a non-correlated part which shape is given by the *Mix*. The *Data* spectrum, $F(M_{inv})$ can then be written as

$$F(M_{inv}) = N_{ev} \cdot N_{pair}(\xi \cdot BW(M_{inv}, M_0, \Gamma) + (1 - \xi)g(M_{inv})) \quad (4.1)$$

$\mathrm{BW}(M_{inv}, M_0, \Gamma)$ is a modified Breit-Wigner function, corrected for our geometrical acceptance, normalized to unity. M_0 and Γ are the peak position and width respectively of the acceptance-corrected modified

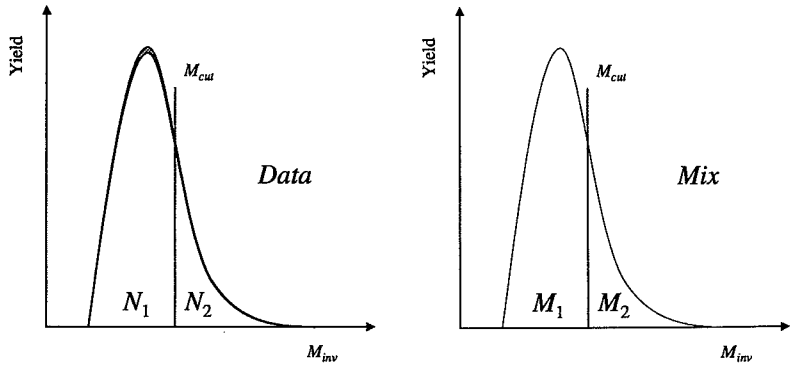

Figure 4.1: *Schematic illustration of the similarity between the invariant mass, M_{inv}, of $p\pi^+$-pairs within events (Data) and the M_{inv} of $p\pi^+$-pairs in mixed events (Mix). The Δ^{++} resonance is indicated as the grey area sitting on top of the spectrum of $p\pi^+$-pairs produced in the same event, (Data).*

Breit-Wigner function. N_{ev} is the number of events, $g(M_{inv})$ is the unit normalized mixed events spectrum and ξ is the fraction of Δ^{++} among the $p\pi^+$-pairs, N_{pair}. The (uncorrected) modified Breit-Wigner function is given by

$$BW(M_{inv}, M_0, \Gamma) \propto \frac{q^3}{(q^3+\mu^3)} \frac{1}{((M_{inv}-M_0)^2+(\Gamma/2)^2)} \tag{4.2}$$

where q is the momentum of one of the decay products of the pair in the pair rest-frame and μ=180 MeV/c.[39] The best fit to the data points (x_i, y_i) is then given by the parameter values M_0, Γ and ξ which minimize

$$\chi^2 = \sum_i \frac{(F(x_i)-y_i)^2}{\sigma_i^2} \tag{4.3}$$

where y_i is the given yield for an invariant mass bin around x_i and $\sigma_i = \sqrt{y_i}$.

4.3 Simulations

In the first attempt of applying the reconstruction methods above on simulated data, it was desirable to start with small system sizes (small combinatorial background) and then move to larger system sizes (large combinatorial background). Therefore, FRITIOF (version 7.02) events were generated for p+p, p+Pb, Si+Pb and Pb+Pb collisions, all with a beam energy of 158 A GeV. With the generated p+p, p+Pb and Si+Pb events, the Δ^{++} were reconstructed in full phase space, and with Pb+Pb, the events were filtered through the geometrical acceptance of the second tracking arm. The impact parameter choice was b=0, for p+p and p+Pb and b=0-5 fm for Si+Pb and Pb+Pb.

Figure 4.2 - 4.5 show the results for p+p, p+Pb, Si+Pb and Pb+Pb respectively. The points reflect the resulting invariant mass spectrum after background subtraction using the tail method described above. The solid histogram is the mass spectrum of the FRITIOF generated Δ^{++}. Table 4.1 summarizes the investigation on FRITIOF events.

System	*Events*	$\Delta^{++}_{FRITIOF}$	$\Delta^{++}_{FittingMethod}$	χ^2	$\Delta^{++}_{TailMethod}$
p+p	10 000	1 215	1 399 ± 100	1.3	838 ± 108
p+Pb	10 000	3 818	4 371 ± 489	1.1	3 093 ± 377
Si+Pb	2 500	11 353	17 197 ± 2 891	1.3	9 290 ± 2 819
Pb+Pb	50 000	2 117	2 891 ± 1 460	1.3	1 753 ± 1 754

Table 4.1: *The table lists the reconstructed number of Δ^{++} using the fitting method and tail method. These numbers agree reasonably well with the known number in column three, given by FRITIOF. For p+p, p+Pb and Si+Pb the Δ^{++} were reconstructed in full phase space, whereas for Pb+Pb, the events were filtered through the geometrical acceptance of the second tracking arm before the reconstruction.*

The extracted values in Table 4.1 using the tail method was obtained with an M_{cut} at 1.37 GeV/c^2. The choice of this M_{cut} is based on the knowledge of the mass M_0 and width Γ of the Δ^{++} resonance, which nominally are 1232 MeV/c^2 and 120 MeV/c^2 respectively. Both the fitting method and tail method reconstruct the number of produced

Δ^{++} reasonably well. Although the tail method gives reasonable values on the reconstructed numbers, it is very sensitive to the chosen M_{cut}. In the case of p+p, p+Pb and Si+Pb, going from M_{cut} =1.2 - 1.7, the reconstructed number rises up to $M_{cut} \simeq 1.4$ and then flattens out. In the case of Pb+Pb however, the method becomes too unstable to be of any use. This is also reflected in the large error obtained for Pb+Pb as seen in Table 4.1 (as large as the signal). The rescale method, although quite good in many cases, occasionally resulted in values with very large errors, rendering the method without any practical use. Thus in our continuing studies we concentrate on the fitting method. The estimation of the errors in Table 4.1 will be discussed in Chapter 4.4 below.

Table 4.2 gives the calculated signal to background ratio, i.e. the number of produced Δ^{++} given by FRITIOF divided by the number of $p\pi^+$-pairs within events. The ratio decreases more than two orders of magnitude in going from p+p to Pb+Pb which indicates the level of difficulty in reconstructing the Δ^{++} in Pb+Pb collisions.

System	S/B $[10^{-4}]$
p+p	889
p+Pb	131
Si+Pb	11
Pb+Pb	3

Table 4.2: *Signal to background ratio for the four different systems investigated in FRITIOF. The ratio is calculated as the number of produced* Δ^{++} *given by FRITIOF divided by the number of* $p\pi^+$*-pairs, within events.*

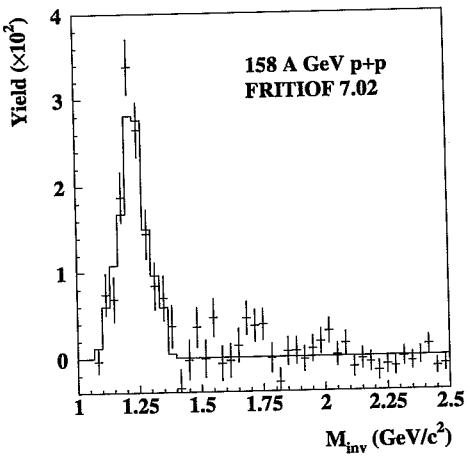

Figure 4.2: *The resulting invariant mass distribution of $p\pi^+$-pairs after background subtraction using the tail method (points) and the the mass spectrum of the FRITIOF generated Δ^{++} (histogram).*

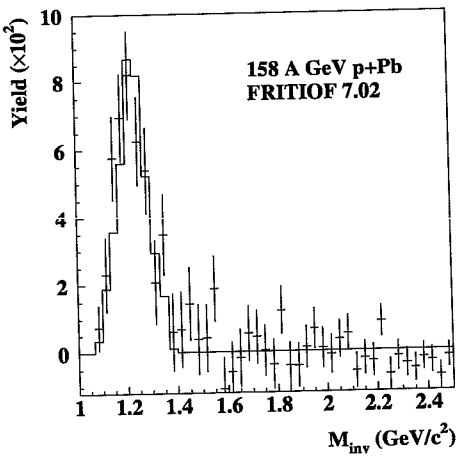

Figure 4.3: *The resulting invariant mass distribution of $p\pi^+$-pairs after background subtraction using the tail method (points) and the the mass spectrum of the FRITIOF generated Δ^{++} (histogram).*

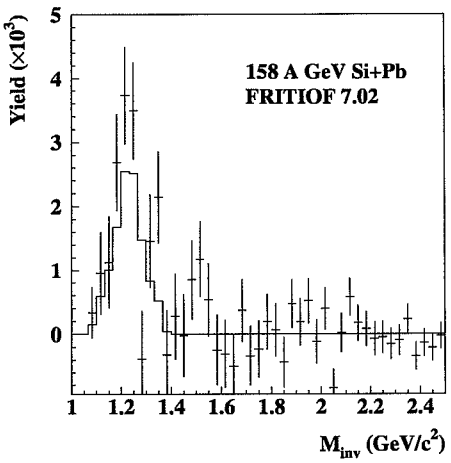

Figure 4.4: *The resulting invariant mass distribution of $p\pi^+$-pairs after background subtraction using the tail method (points) and the the mass spectrum of the FRITIOF generated Δ^{++} (histogram).*

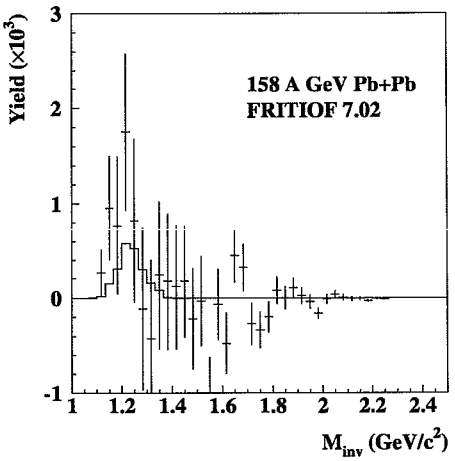

Figure 4.5: *The resulting invariant mass distribution of $p\pi^+$-pairs after background subtraction using the tail method (points) and the the mass spectrum of the FRITIOF generated Δ^{++} (histogram).*

4.4 Error Estimation

In the fitting method, the error in the reconstructed number of Δ^{++}, δN^{++}, is obtained from

$$\delta N^{++} = \delta\xi \cdot N_{pair} \tag{4.4}$$

where $\delta\xi$ is the error in the ξ-parameter obtained from the best fit (see Eq. 4.1).

In the tail, method the number of Δ^{++}, N^{++}, is calculated from (see Fig. 4.1)

$$N^{++} = N_1 - \lambda \cdot M_1 = N_1 - \frac{N_2 \cdot M_1}{M_2} \tag{4.5}$$

where the combinatorial background fraction, λ is

$$\lambda = \frac{N_2}{M_2} \tag{4.6}$$

and N_1, N_2 the number of pairs in *Data* before and after M_{cut} respectively, M_1, M_2 the number of pairs in *Mix* before and after M_{cut} respectively. If we denote N^{++} with $f(x_1, x_2, x_3, x_4)$ where $(x_1, x_2, x_3, x_4) = (N_1, N_2, M_1, M_2)$, the variance of f becomes

$$V(f) \simeq \sum_{i=1}^{4}\sum_{j=1}^{4} \frac{\partial f}{\partial \bar{x}_i}\frac{\partial f}{\partial \bar{x}_j} cov(\bar{x}_i, \bar{x}_j) \tag{4.7}$$

where

$$\bar{x}_i = \frac{1}{N}\sum_{k=1}^{N} x_{ik} \tag{4.8}$$

N is the total number of measurements, i.e. events and

$$cov(x_i, x_j) = \frac{1}{N}\sum_{k=1}^{N}(x_{ik} - \bar{x}_i)\cdot(x_{jk} - \bar{x}_j) \tag{4.9}$$

The errors on the reconstructed Δ^{++} calculated with Eq. 4.4 (for the fitting method) and Eq. 4.7 (for the tail method) are listed in the fourth and sixth column of Table 4.1 respectively. Both methods yield similar errors.

Chapter 5

Δ^{++} Production in Pb+Pb Collisions at 158 A GeV

Using the second tracking arm of WA98, the production of Δ^{++} has been studied in 158 A GeV ^{208}Pb+^{208}Pb collisions at the CERN SPS. The method employed was to construct the invariant mass spectrum of all pπ^+-pairs within events and subtracting a mixed events background using the fitting method as described in Chapter 4.2. Our results in comparison with a thermodynamic model as well as other experiments at lower energies will be presented.

5.1 Δ^{++} Acceptance

Figure 5.1 shows the geometrical acceptance of the second tracking arm in terms of transverse momentum and rapidity for Δ^{++} obtained from FRITIOF events filtered through the geometrical acceptance, i.e. for Δ^{++} where both decay particles fall inside the acceptance of the arm. Note that the spectrum is unfolded in the same way as in the acceptance plot for protons and pions, Fig. 3.4.

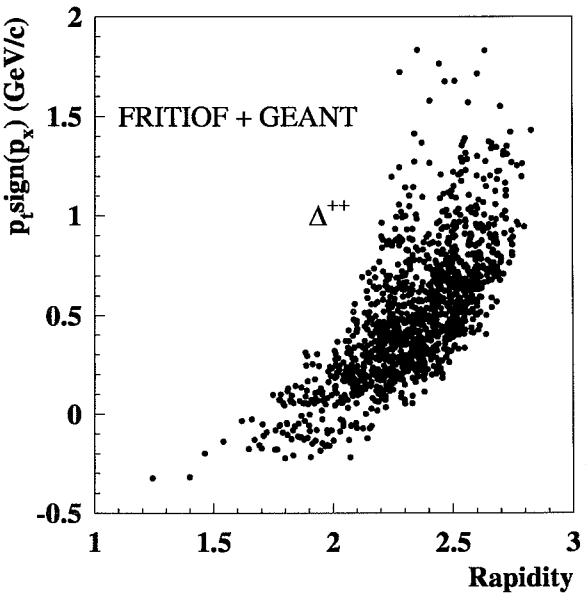

Figure 5.1: *The geometrical acceptance of the second tracking arm for Δ^{++}, i.e. when both decay products fall inside the acceptance of the arm. The Δ^{++} were generated with FRITIOF 7.02, 158 A GeV central Pb+Pb collisions and used as input to GEANT.*

5.2 Combinatorial Background

Figure 5.2 a) and b) show the invariant mass distribution of all $p\pi^+$-pairs within events and in mixed events respectively. To reduce the statistical errors the mixed events spectrum contains about ten times the statistics in that of the real spectrum. Figure 5.2 c) shows the correlation-signal, i.e. the difference between the distribution in a) and b) normalized to the same content. At the invariant mass where we would expect the $\Delta(1232)$ resonance, a signal is clearly observed. It is now important to show that our starting point is true, i.e. the background in data is the same as in the mix, otherwise the correlation-signal will be distorted. This is done in Fig. 5.3 in two ways. Figure 5.3 a) shows the invariant mass

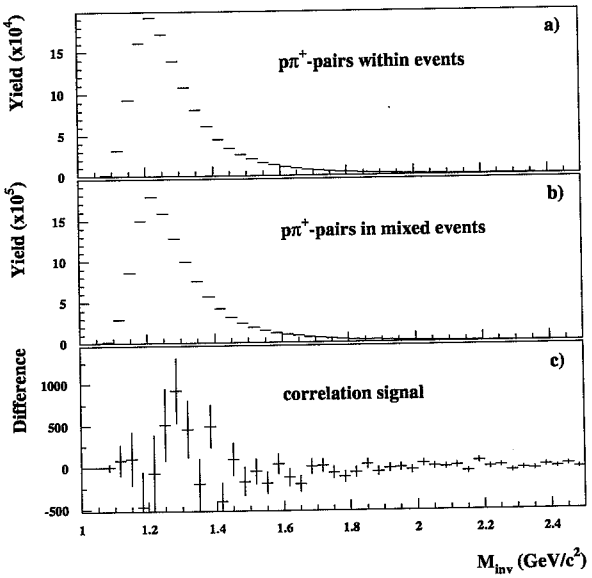

Figure 5.2: *a) The invariant mass distribution of all $p\pi^+$-pairs within events and b) in mixed events and c) the difference between the distribution in a) and b) normalized to the same number of pairs.*

distribution for *Data* divided by *Mix* normalized to the same content. The ratio is one as expected and do not vary with the invariant mass, except for a few bins in the high mass tail. Figure 5.3 b) shows *Data* (solid histogram) and *Mix* (points) normalized to the same content. The points fall on top of each other as expected and there are small deviations only in the high mass tail.

By taking the difference between *Data* and *Mix* as in Fig. 5.2 c), we are sensitive to small differences where we have a lot of pairs, i.e. where the Δ^{++} peak is located. But we are not very sensitive to differences in the tail, where the number of pairs is small. By taking the ratio between *Data* and *Mix* as in Fig. 5.3 a), we become sensitive to the overall shape, especially in the tail region. In this representation the tiny delta signal vanishes. The ratio being constant indicates that the

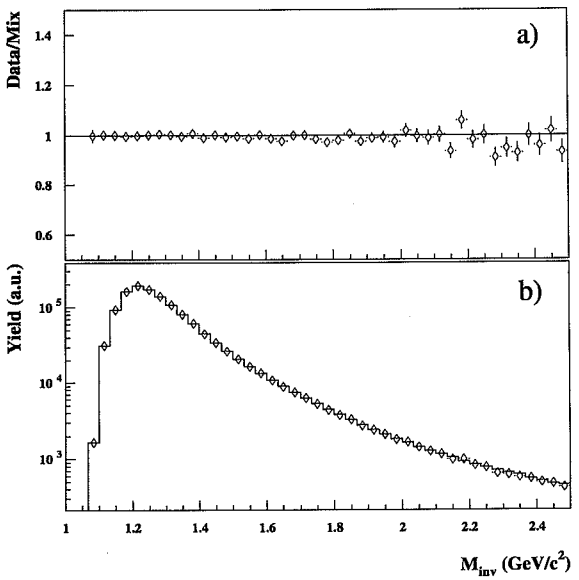

Figure 5.3: *Two ways of illustrating the quality of the mixed events technique. a) The invariant mass distribution for Data divided by Mix, normalized to the same content. b) Data (diamonds) and Mix (histogram), normalized to the same content, plotted on top of each other.*

assumption, that the combinatorial background can be described by the mixed event technique, is reasonable.

The fitting method described in Chapter 4.2 applied on the data yields 2461±1105 Δ^{++} using the full sample of 119 677 central events. Figure 5.4 shows the extracted signal with the best fit ($\chi^2 = 1.2$). With the amount of statistics and the accuracy in the measurement, we are not sensitive enough to quote the mass or width of the signal. As an effect of the limited acceptance, the apparent width in the raw spectrum is narrower than the natural width of the Δ^{++}. This is also observed in the FRITIOF simulation with Pb+Pb where the events were filtered through our acceptance.

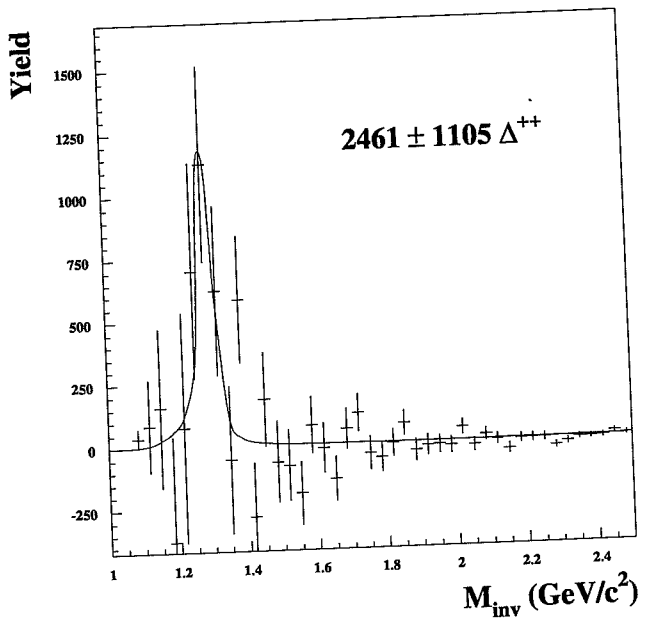

Figure 5.4: *The extracted Δ^{++} resonance obtained from the fitting method. Also shown is the acceptance filtered modified Breit-Wigner function obtained from the best fit.*

5.3 Corrections

To be able to compare our result with models and other experiments it is necessary to correct for acceptance and inefficiencies. In Table 5.1, the tracking efficiency factor k_{eff}, for Δ^{++} is the probability for both the pion and proton from the Δ^{++}, entering the arm, to result in valid tracks. k_{eff} for Δ^{++} is obtained as the product of the efficiency factors for protons and pions, which are the same. These factors essentially include two effects. The first one takes into account the inefficiency of the individual tracking planes and the second one the inefficiencies introduced in the tracking reconstruction algorithm.

119677 Central events	Protons	Δ^{++}
Particles observed	120906	2461±1105
Particles/Event (uncorrected)	1.01027	0.02056
Tracking efficiency, k_{eff}	0.8777	0.7704
Identification efficiency, k_{pid}	0.6168	0.3804
Particles/Event (eff. corrected)	1.8662	0.0702
Geometrical acceptance, k_{geo}	0.1127	0.0163
Particles/Event (full ϕ)	16.56	4.30

Table 5.1: *Summary of the different correction factors and results.*

The geometrical acceptance factor k_{geo}, corrects for the limited azimuthal coverage of the arm and is estimated by GEANT simulations. The procedure for obtaining k_{geo} is given below.

Step 1: A $p_t p_z$ distribution taken from data for protons and pions respectively given a random ϕ-angle is used as input. Two histograms are filled, generated particles (full ϕ) and geometrically accepted particles (particles traversing at least three tracking planes and the TOF wall). By dividing these two spectra with each other a correction factor for every $p_t p_z$-bin is obtained. The total correction factor k_{geo}, for protons or pions is then obtained by summing over all bins as

$$k_{geo} = \frac{\sum w(p_z, p_t) \cdot k_{geo}(p_z, p_t)}{\sum w(p_z, p_t)} \tag{5.1}$$

where the weight $w(p_z, p_t)$ is given by the acceptance corrected spectrum.

Step 2: Whenever the invariant mass of a proton and a pion is within three σ from the Δ^{++} mass ($M_0 \simeq 1232$ MeV/c^2, $\sigma \simeq 51$ MeV/c^2) the pair is regarded as a Δ^{++} candidate. Those candidates are counted, weighted with the correction factors obtained for protons and pions in step 1.

Step 3: The Δ^{++} candidates obtained in step 2 are read into GEANT given a random ϕ-angle and are sent to a decay routine. Here, the cases where both the proton and pion are seen in at least three out of the four tracking planes and the TOF wall are counted, again weighted with

the correction factors obtained for protons and pions in step 1. The geometrical acceptance for Δ^{++} given in Table 5.1 is obtained by the ratio between the two numbers obtained in step 2 and step 3.

In this procedure it is implicitly assumed that the Δ^{++} candidates have the same momentum distribution as real Δ^{++}. Alternatively a Δ^{++} momentum distribution from some model could have been used, but since different models predict different momentum distributions it can not be done in a model independent way. Since the momentum distribution of Δ^{++} to a high extent reflects the momentum distribution of protons we prefer to take this approach, i.e. that the false Δ^{++} candidates approximately have the same distribution as the real ones.

Finally the identification efficiency k_{pid}, is the probability that a particle, registered as a valid track, has an association in the TOF wall which provides an unambiguous identification. This relatively small factor results from a timing problem in the TOF wall, reducing the particle identification considerably. In every event, about 40% of the TOF modules failed. The exact cause of this is not yet understood, but the effect has been studied in detail and no correlation between module number and particle type or location has been found. We thus have no indication of that the identification efficiency for protons should differ from that of pions. In Table 5.1, k_{pid} for the Δ^{++} is thus the square of k_{pid} for protons and pions.

5.4 Interpretation of the Results

To interpret our result we can compare with a thermal model, where the ratio of $\Delta(1232)$/nucleons can be used to determine the freeze-out temperature of the system. We must then assume chemical and thermal equilibrium. A system is said to have reached chemical equilibrium when the interactions of the constituents do not alter the densities of different types of particles. Thermal equilibrium is reached when the momentum distributions of the particles do not change, even though momentum exchanges continue through the interaction between particles. If we consider our system as a gas of hadrons at thermal and chemical equi-

librium, the occupation probabilities of the hadrons are given by the Fermi-Dirac distribution. To obtain the occupation probabilities of the nucleon and all non-strange baryonic resonances as a function of the temperature we thus have to calculate

$$\rho_i \propto g_i \int_0^\infty \frac{p^2}{e^{\frac{\epsilon_i - \mu}{T}} + 1} dp \tag{5.2}$$

where $\epsilon_i = \sqrt{p^2 + m_i^2}$ is the total energy, $g_i = (2J+1)(2I+1)$ the statistical weight, J the spin, I the isospin, T the temperature and μ the chemical potential.

Our calculation follows that of [37] but instead of using a fixed value on the total density, the chemical potential μ, is calculated from Eq. 5.2 for every temperature using the $\bar{\text{p}}$/p ratio found to be 0.01 in our data[40].

Table 5.2 gives the results of the calculation at T=150 MeV. The total occupation probability ρ_t, is the sum over the occupation probabilities of all states listed. The error in our $\bar{\text{p}}$/p measurement is large but ρ_i/ρ_t turns out to be almost insensitive to the chemical potential μ. In Fig. 5.5 the relative occupation probability of the $\Delta(1232)$ resonance, is plotted as a function of the temperature. Now, to obtain the total number of $\Delta(1232)$ resonances from data, i.e. Δ^{++}, Δ^{+}, Δ^{0} and Δ^{-}, we multiply the number of Δ^{++} by an isospin factor 4. In the same way, the number of nucleons, including those from resonance decays, can be estimated by multiplying the measured number of protons with a factor two. The $\Delta(1232)$/nucleons ratio obtained from our analysis is 0.52±0.23, i.e. 52% of the nucleons at central rapidities originate from a $\Delta(1232)$. As we see from Fig. 5.5, a ratio of 0.52 is greater than the maximum given by the model, which is 0.33 at T=150 MeV. This is what we would expect since the model tells us how many $\Delta(1232)$ we have at freeze-out, but what we measure in the experiment is also those $\Delta(1232)$ which decay before freeze-out and where the decay products escape without further interactions. Thus our high value is in no conflict with a thermal model.

Regarding the statistical error of the found ratio it is to the first order given by the statistical fluctuations in the number of combinatorial pairs under the resonance peak. In our case this error coincides with the error obtained from the fitting method. It is thus impossible to obtain

State	J	I	g_i	$\rho_i/\rho t$
p	1/2	1/2	2	0.204
n	1/2	1/2	2	0.202
N(1440)	1/2	1/2	4	0.025
N(1520)	3/2	1/2	8	0.032
N(1535)	1/2	1/2	4	0.014
N(1650)	1/2	1/2	4	0.074
N(1675)	5/2	1/2	12	0.019
N(1680)	5/2	1/2	12	0.019
N(1700)	3/2	1/2	8	0.011
N(1710)	1/2	1/2	4	0.005
N(1720)	3/2	1/2	8	0.001
N(2190)	7/2	1/2	16	0.001
N(2220)	9/2	1/2	20	0.001
N(2250)	9/2	1/2	20	0.001
N(2600)	11/2	1/2	24	0.000
Δ(1232)	3/2	3/2	16	0.327
Δ(1600)	3/2	3/2	16	0.040
Δ(1620)	1/2	3/2	8	0.018
Δ(1700)	3/2	3/2	16	0.022
Δ(1900)	1/2	3/2	8	0.003
Δ(1905)	5/2	3/2	24	0.010
Δ(1910)	1/2	3/2	8	0.003
Δ(1920)	3/2	3/2	16	0.006
Δ(1930)	5/2	3/2	24	0.009
Δ(1950)	7/2	3/2	32	0.010
Δ(2420)	11/2	3/2	48	0.000

Table 5.2: *Given is the spin J, isospin I, statistical weight g_i and relative occupation probability ρ_i/ρ_t for the nucleon ground state (p,n) and all non-strange baryonic resonances.*

the ratio with higher accuracy with the given statistics, independent of the extraction method used. From our studies with event generators, extraction methods and variation of cuts implied on the data, we find that the systematic errors are considerably smaller than the obtained statistical errors. The systematic errors are thus neglected in the results.

The presented data are the first measurement of the Δ^{++} abundance at these energies. Comparison of the results can therefore only be made with other experiments at lower energies. This has been done in paper IV.

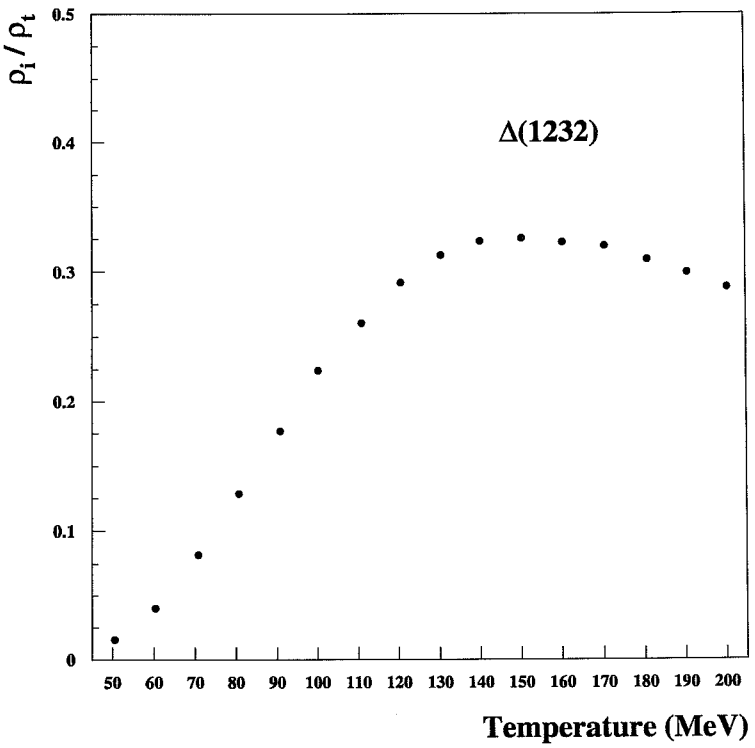

Figure 5.5: *The relative occupation probability ρ_i/ρ_t of the $\Delta(1232)$ resonance as a function of the temperature.*

Chapter 6

Summary

The experiences from the construction of a large-acceptance tracking arm in the WA98 experiment have been presented. The newly developed readout system for multi-step avalanche chambers, based on a specially designed readout chip, was exhibited. The performance of the readout system confirm the design goals of high uniformity, reliability and sensitivity. The 70 000 channel readout system was installed and run in the experiment in the fall 1996. The results show that straight-line tracking using only four space points along the track, is possible at the encountered particle density. The momentum resolution was in the range 1-3% and π/K separation was achieved up to 4 GeV/c and p/π separation up to 8 GeV/c.

A reliable method on the extraction of Δ^{++} resonance from high multiplicity data was demonstrated using high statistics FRITIOF events. Using the high resolution spectrometer, the production of Δ^{++} has been studied in 158 A GeV Pb+Pb collisions. The presented data are the first measurement of the Δ^{++} abundance at these energies. The results are in general agreement with a thermal model and measurements performed at lower energies by other experiments.

The analysis of data from the tracking arm shows that high quality spectra of π,K,p can be produced and that a study of ϕ-meson production is possible.

The analysis of data from the other detectors in the experiment is in an advanced stage on topics such as directed and elliptic flow, thermal photon production and search for disoriented chiral condensates.

Chapter 7

The Papers

Paper I: Fabrication and test of a 70 000 channels pad readout system for multi-step avalanche chambers

Nucl. Instr. and Methods A **413** (1998) 92.

This paper describes a new electronic readout concept which was developed and built for the second tracking arm of experiment WA98 at the CERN SPS. The readout concept is based on the use of Multi-Step Avalanche Chambers equipped with a very large number of readout channels (58 000/m^2). Due to the large number of readout channels, it was necessary to mount the electronics directly onto the backplane of the detector. The technique of Chip-On-Board (COB) mounting using thin printed circuit boards, was used to minimize secondary interactions in the backplane material. This was the first time the COB technique was applied to a large scale fabrication of electronics used in high energy physics. The experiences of mounting and testing a large readout system based on a custom-design readout chip containing both amplifier and analog-to-digital conversion in the same chip are presented. The electronic performance of the system as well as the complete readout concept is discussed.

Paper II: Performance of multi-step avalanche chambers equipped with two-dimensional electronic readout

Nucl. Instr. and Methods A **412** (1998) 361.

This paper presents results from studies of Multi-Step Avalanche Chambers equipped with an electronic readout system designed for the WA98 experiment. A detailed description of different aspects of the chambers such as gas and high-voltage features as well as the influence of the chambers on the readout electronics are given. Results from the system in lead-beam reveal a reconstruction efficiency of the chambers in the range 91-96%, depending on the density of charged particles. The position resolution was found to be 0.5 mm and 1.7 mm in the horizontal and vertical directions, respectively.

Paper III: A large-acceptance spectrometer for tracking in a high multiplicity environment, based on space point measurements and high resolution time-of-flight

Submitted to Nucl. Instr. and Methods A.

A large acceptance tracking system for tracking at very high particle densities in the WA98 experiment at the CERN SPS is described. The system is based upon Multi-Step Avalanche Chambers (MSACs) in combination with streamer tube detectors all equipped with a new electronic pad readout system with a large number of channels. The MSACs, with higher position resolution and the streamer tube detectors with coarse position resolution, yet enough for safe track recognition, together with a high resolution time of flight detector make up the full tracking system. Particle identification up to 8 GeV/c for pions and protons and pion/kaon separation up to 4 GeV/c was achieved. Important results such as efficiency, momentum resolution and two-track resolution are presented.

Paper IV: Δ^{++} Abundance in 158 A GeV ^{208}Pb+^{208}Pb interactions at the CERN, SPS

To be submitted.

It has been suggested that if the abundance of $\Delta(1232)$ at freeze-out can be determined, then from the ratio $\Delta(1232)$/nucleons, the temperature of the system can be determined. This would give an independent measurement of the temperature than what comes out from the slopes of the particle spectra. We present measurements on the production of Δ^{++} by means of invariant mass analysis of $p\pi^+$-pairs in 158 A GeV central ^{208}Pb+^{208}Pb collisions at the CERN SPS. The measurement utilizes the new high resolution tracking arm of WA98. Being the first measurement of the Δ^{++} abundance at these energies, comparison of the results are made with other experiments at lower energies and with a thermal model calculation assuming thermal and chemical equilibrium.

Bibliography

[1] J.D. Bjorken, Phys. Rev. D **27** (1983) 140.

[2] G. Baym, Nucl. Phys. A **447** (1986) 463c.

[3] P. Koch, B. Müller and J. Rafelski, Phys. Rep. **142** 167 (1986).

[4] M. Gonin et al. (E802/E866 collaboration), Nucl. Phys. A **566** (1994) 601c.

[5] D. Rörich et al. (NA35 collaboration), Nucl. Phys. A **566** (1994) 35c.

[6] M. Gonin et al. (NA50 collaboration), Nucl. Phys. A **610** (1996) 404c.

[7] D. Lissauer and E.V. Shuryak, Phys. Lett. B **253** (1991) 15.

[8] D.K. Srivastava and B. Sinha, Phys. Rev. Lett. **73** (1994) 2421.

[9] R. Santo et al. (WA80 collaboration), Nucl. Phys. A **566** (1994) 61c.

[10] T.C. Awes et al. (WA80 collaboration), Nucl. Phys. A **590** (1995) 81c.

[11] M.M. Aggarwal et al. (WA93 collaboration), Phys. Rev. C **56** (1997) 1160.

[12] P. Wurm et al. (CERES collaboration), Nucl. Phys. A **590** (1995) 103c.

[13] L. van Hove, Phys. Lett. B **118** (1982) 138.

[14] Physics World, September 1996

[15] R.J. Glauber, in Lectures in Theoretical Physics, edited by W.E. Brittin and L.G. Dunham (Interscience, N.Y., 1959), Vol. 1, p. 315.

[16] WA98 collaboration, *Proposal for a Large Acceptance Hadron and Photon Spectrometer*, 1991, Preprint CERN/SPSLC 91-17, SPSLC/P260.

[17] T. Chujo et al., Nucl. Instr. and Methods A **383** (1996) 409.

[18] A. Baden et al., Nucl. Instr. and Methods A **203** (1982) 189.

[19] M.M. Aggarwal et al. (WA98 collaboration), submitted to Physical Review Letters.

[20] H.Å. Gustafsson, et al., Phys. Rev. Lett **52**, (1984) 1590.

[21] W.T. Lin et al. Nucl. Instr. and Methods A **389** (1997) 415.

[22] A. Breskin et al., Nucl. Instr. and Methods A **161** (1979) 19.

[23] A. Breskin et al., Nucl. Instr. and Methods A **178** (1980) 11.

[24] G. Charpak et al., Nucl. Instr. and Methods A **274** (1989) 275.

[25] M. Izycki et al., Nucl. Instr. and Methods A **310** (1991) 98.

[26] M.M. Aggarwal et al., Nucl. Instr. and Methods A **372** (1996) 143.

[27] M.M. Aggarwal et al. (WA98 collaboration), Phys. Lett. B **420** (1998) 169.

[28] H. Baumeister et al., Nucl. Instr. and Methods A **292** (1990) 81.

[29] R. Hwa and K. Kajantie, Phys. Rev. D **32** (1985) 1109.

[30] M.M. Aggarwal et al. (WA98 collaboration), Phys. Rev. Lett. **81** (1998) 4087.

[31] R. Albrecht et al., Nucl. Instr. and Methods A **276** (1989) 131.

[32] T.C. Awes et al., Nucl. Instr. and Methods A **279** (1989) 479.

[33] Y.Y. Lee, *The Trigger System for WA98*, GSI Sci. report, 1995.

[34] M.M. Aggarwal et al. (WA98 collaboration), "Systematics of Transverse Energy Production in ^{208}Pb Induced Collisions at 158 GeV/nucleon", UT/ORNL WA98 Preprint.

[35] R. Brun and F. Carminati, *GEANT Detector Description and Simulation Tool*, CERN Program Library, Long Writeup W5013, March 1994.

[36] J.M. Rubio, *Transverse flow from m_T spectra in Pb+Pb collisions at 158 GeV/c per nucleon*, PhD thesis, Université de Genevè, 1997.

[37] G.E. Brown, J. Stachel and G.M. Welke, Phys. Lett. B **253** (1991) 19.

[38] B. Nilsson-Almqvist and Evert Stenlund, Comp. Phys. Comm. **43** (1987) 387.

[39] E. L. Hjort et al., Phys. Rev. Lett. E **79** (1997) 4345.

[40] T. Svensson, PhD thesis, Lund University, 1999.

Paper I

ELSEVIER

Nuclear Instruments and Methods in Physics Research A 413 (1998) 92–104

NUCLEAR INSTRUMENTS & METHODS IN PHYSICS RESEARCH Section A

Fabrication and test of a 70 000 channels electronic pad readout system for multi-step avalanche chambers

L. Carlén[a], K. El Chenawi[a,*], J. Dalstra[b], J.R. Fransens[b], S. Garpman[a], H.-Å. Gustafsson[a], H. Hasper[b], B. Kolb[c], H. Löhner[d], S. Louw[d], M. Martin[e], Y. Miake[f], H. Naef[e], P. Nilsson[a], J. Nystrand[a], A. Oskarsson[a], L. Österman[a], I. Otterlund[a], E. Perrin[e], L. Rosselet[e], J.M. Rubio[e], K. Söderström[a], N. Solomey[e], E. Stenlund[a], T. Svensson[a]

[a] *Division of Cosmic and Subatomic Physics, Lund University, Box 118, SE-22100 Lund, Sweden*
[b] *Centrum voor Technische Informatica (CTI), PO Box 7080, NL-9701 JB Groningen, The Netherlands*
[c] *Gesellschaft für Schwerionenforschung (GSI), D-64220 Darmstadt, Germany*
[d] *KVI, University of Groningen, NL-9747 AA Groningen, The Netherlands*
[e] *University of Geneva, CH-1211 Geneva 4, Switzerland*
[f] *University of Tsukuba, Tennoudai, Tsukuba 305, Japan*

Received 10 February 1998

Abstract

A new readout concept based on a custom-design chip containing both analog and digital functions as well as ultra-thin mounting with the chip-on-board technique is presented. The full readout system as well as fabrication and testing is described. A 70 000 channels system based on this concept was installed in the WA98 experiment at the CERN SPS. The performance of the readout electronics is presented.

PACS: 29.40.CS; 29.40.GX; 07.50.QX

Keywords: Pad readout; Electronic; VLSI; ASIC; Chip-on-board

1. Introduction

The very large multiplicities of charged particles produced in ultra-relativistic heavy-ion collision experiments presently under study at the CERN SPS provide new experimental challenges. The charged particle density in the tracking chambers of the WA98 experiment is for the most central collisions about 30 particles/m^2. This is comparable to the expected densities in the tracking detectors in the heavy-ion experiments at the colliders RHIC and LHC. These large multiplicities require tracking detectors with high granularity to achieve the necessary two-track resolution and to be able to extract accurate position information for each individual track. A tracking system based on Multistep

* Corresponding author. Tel.: +46 46 222 4767; fax: +46 46 222 4015; e-mail: karim@kosufy.lu.se.

0168-9002/98/$19.00
PII: S0168-9002(98)00385-4

Avalanche Chambers (MSACs) [1–4] equipped with an electronic readout system can fulfill these requirements.

This new readout concept is based on the use of MSACs, equipped with a very large number of readout channels (58 000/m^2). This requires the electronics to be mounted directly onto the detector backplane and the data reduction processors to be close to the detector. It is necessary to use thin printed circuit boards for mounting of the electronics to minimize the secondary interactions in the backplane material. This can be achieved by using the Chip-On-Board (COB) mounting technique, which is often used in commercial home electronics. Here, for the first time, this technique has been applied to large-scale fabrication of electronics in high-energy physics experiments. This paper presents the experiences of mounting and testing a large readout system based on a custom-design readout chip containing both amplifier and analog-to-digital (AD) conversion in the same chip. The electronic performance of the total system as well as the complete readout concept is discussed.

2. System description

The main components of the readout concept are shown in Fig. 1. It consists of the readout chips mounted on the backplane of the chamber, the gateboards on top of the chamber and the data reduction and readout system with DSP-boards based on Digital Signal Processors (DSP) at the bottom of the chamber. The compressed data are transferred to the VME-based data acquisition system at a 10 m distance from the detector.

The MSAC detector is a parallel-plate avalanche chamber with two amplification stages [5,6] operated at an amplification of about 10^5. The liberated electrons are collected on the pads which are connected to the readout chips. The charge cloud, when reaching the padplane, has a typical extension of 5 mm, covering several pads.

The readout chip [7] is a specially designed Application Specific Integrated Circuit (ASIC) for readout of MSACs. It consists of 16 parallel charge integrating amplifiers, an analog multiplexer, a six bit nonlinear flash ADC and a memory. The chip is

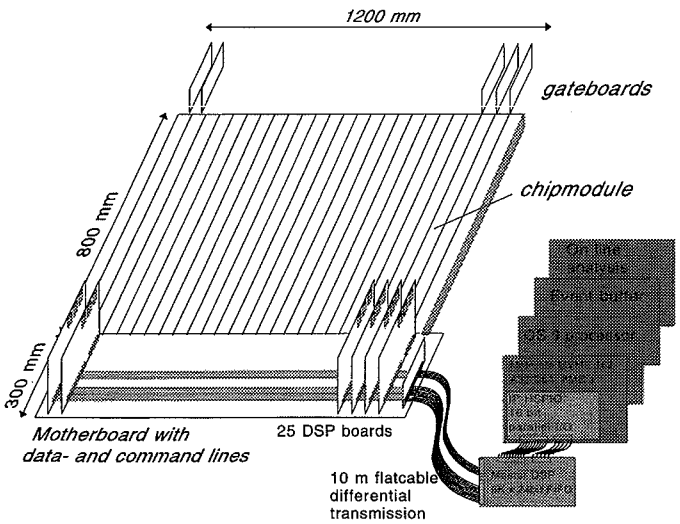

Fig. 1. Schematic drawing of the readout concept.

supplied with analog and digital voltages and gate signals from the gate boards. The DSP boards (see Section 4) supply two reference voltages, one clock and one reset signal to each column of chips. The two reference voltages set the lower and upper limits of the flash ADC, thus determining the sensitivity of the ADC scale. The basic functions of the chip are schematically shown in Fig. 2. The first level data processing is performed by signal processors placed on the DSP boards on the chamber.

3. Backplane assembly

3.1. Printed circuit boards

The chips were mounted on $48 \times 206\,\mathrm{mm}^2$, 220 μm thick FR4, printed circuit boards (called chipboards). One side of the board contained the pad structure shown in Fig. 3b. The size of the pads was 1 mm in the horizontal and 17 mm in the vertical direction. The pads were staggered with a $\frac{1}{3}$ overlap in the vertical direction. The chosen pad structure was based on simulations [5] to have the optimum position resolution in the horizontal direction which is the bending plane of the dipole magnet in the WA98 tracking system. The vertical resolution needs only to be sufficiently good to ensure unambiguous tracking.

The electron cloud was, due to the staggering, in most cases sensed on several pads in both directions. This allows the center of gravity of the electron cloud to be determined accurately in both directions.

The other side of the board housed three columns of 12 chips each, making a total of 36 chips on a board. The connections between the pads and the chip were done through plated-through holes. In addition, all communication lines were placed on the chip side of the board. These lines are divided into three identical groups, each supporting one of the three chip columns. The circuit layout is shown

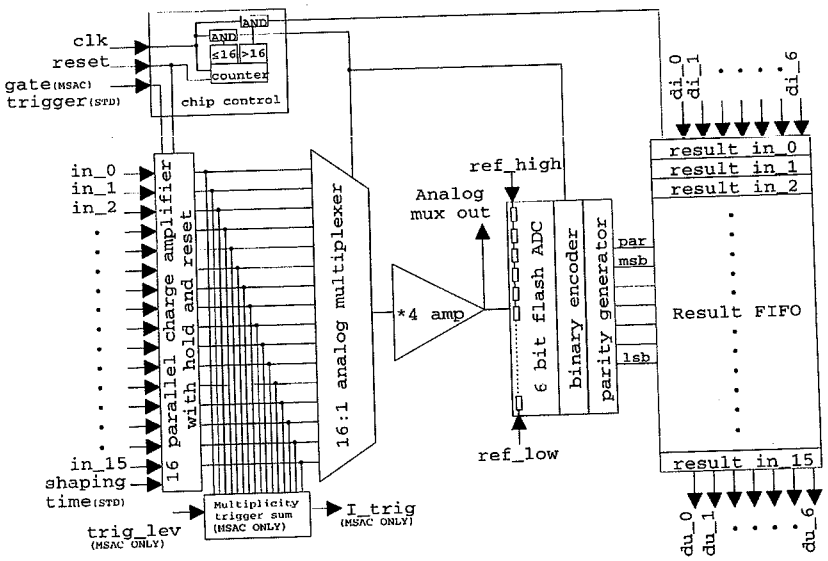

Fig. 2. Schematic block scheme of the readout chip.

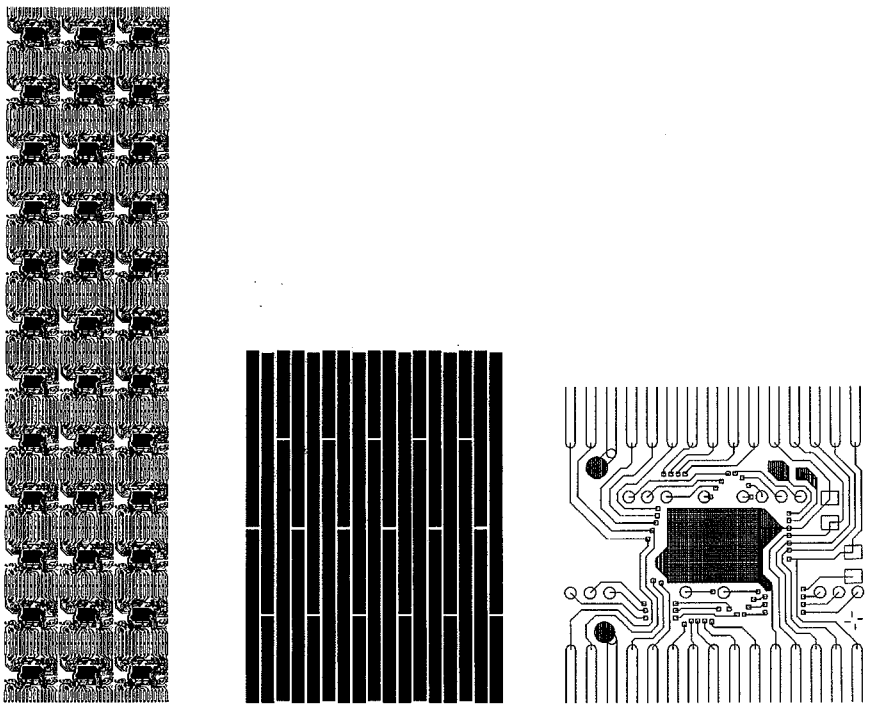

Fig. 3. Printed circuit board for mounting of the readout chips. (a) Chip side of the board showing the communication lines and chip positions and (b) Magnified part of pad side (padsize $1 \times 17\,mm^2$) and (c) Magnified view of the area around one chip.

in Fig. 3a. Fig. 3c is a magnified view of the trace layout around one chip. Each column has traces for digital and analog supply voltages, two ground lines, two reference voltages for the chips, seven data output lines, clock and reset signals. All chips in a column share these lines.

The TTL gate signals to the preamplifiers of the chips start the integration of the charge collected on the pads. The edges of the gate signals may induce charge on the pads and add to the collected charge, thus affecting the sensitivity of the system. To minimize the influence of the gate signals on the pads, two precautions were taken. One was to distribute the gate signals from separate printed circuit boards, one for each chip column. These gateboards, made from FR4 with dimensions $5 \times 206\,mm^2$ and a thickness of $110\,\mu m$, feed the gate lines and were glued on top of the chipboard. The gate lines were shielded from the chipboard by an extra ground plane. The second precaution was to distribute two signals identical in shape but with opposite polarity on the gate board, thus essentially canceling the effect of the two pulse edges.

3.2. *Chip-on-board mounting and testing procedure*

Each chip was delivered wafer tested and cut out from the wafer. The wafer testing rejected about

15% of the chips on a wafer, predominantly located near the wafer edge. The chips were mounted with the COB technique which means that the naked chips were glued onto a grounded pad (diepad) on the board and the electrical connections were made by ultrasonic wirebonding. The COB assembly was done in automatic bonding machines by a commercial company [8], which also had developed techniques for replacing bad chips. Fig. 4 shows a naked chip mounted on the board. Each chip has 40 bondwire connections. Bypass capacitors were mounted at several places on DC lines on the boards. Due to the thickness constraint, a multilayer circuit board was prohibited. Since the pads take up one surface of the board, only one side is available for circuit traces and chips. The COB assembly allows very flexible circuit solutions since the bondwires from the chip can jump over many traces. In this design we have also made use of bondwires making jumps between two locations on the board. There was no need for a groundplane to shield the digital lines (except for the gate signals as mentioned in Section 3.1) since the charge inputs are gated off when the digital operation starts.

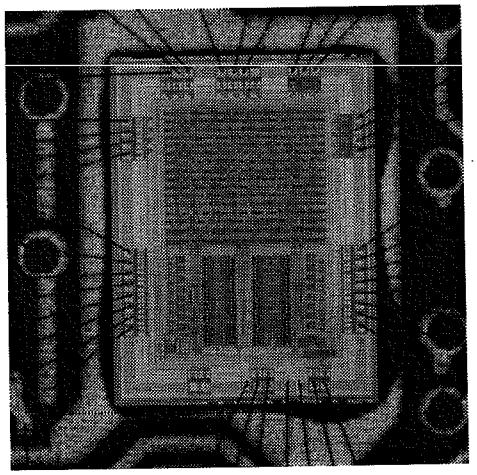

Fig. 4. Naked chip mounted with the COB technique. The chip size is $3.7 \times 4.2\,mm^2$. The bondwires and some of the plated-through holes to the pad side are seen.

A fraction of the chips accepted by the wafer test may still have errors. For testing purposes the boards were delivered with the chips uncovered. Uncovered chips could be replaced while sealed (globbed) chips could not be removed and exchanged. One board containing 36 chips was tested at a time. The tests were done in a semi-automatic way using a PC and Labwindows software [9] for control and readout.

The testing procedure included a check of:

- supply currents,
- digital control and readout of the three chip columns,
- the AD conversion by analyzing DC levels,
- proper functioning of all 16 channels.

The full testing procedure was applied to 5760 chips mounted on 160 boards. The serial architecture of the chip control and readout complicated the testing procedure. An error in one chip influenced and sometimes prevented the test of the chips placed behind it in the readout chain. This could result in several iterations before such a board passed the test. About 40 boards (25% of the total number of boards) passed the test procedure without errors. Approximately, 60 boards (38%) passed the tests after one iteration with replacement of 1 or 2 chips or repair of 1 or 2 bad wirebondings. Two iterations with a replacement of several chips or the repair of several bad bondings were required for about 40 boards (25%). The last 20 boards (12%) required three or more iterations. The serial architecture is the main reason for many iterations.

The total number of rejected chips that failed the acceptance tests was about 300 corresponding to about 5% of the total number of tested chips. This together with the 15% rejected chips from the wafer tests resulted in a total yield of the chip production of about 80%. This yield is fairly satisfying for a chip of the present size. About 180 chips had some kind of bonding error which corresponds to about 3% of the total number of tested chips. These bonding problems were almost always related to two particular bond connections. One was the connection from the separate gate board to the chip and the other was one extremely long bondwire connection on the board.

The boards that passed the acceptance test were sent for sealing of the naked chips. This was done by a globtop which is a layer of epoxy protecting the chips and bondwires from dust and mechanical damage. One full board mounted with 36 chips is shown in Fig. 5. The total thickness of the board averaged over the full area corresponds to about 0.3% of a radiation length in accordance with the design specifications. The time to assemble and test 160 boards was about six weeks, corresponding to about 1 h of testing per board on the average. The chips, once tested and sealed, have not shown any significant failure rate during 2 months of continuous operation.

3.3. Assembly and mounting in the chamber

Three chipboards and two endcards were connected together composing a chipmodule. The connection between the boards and the endcards was achieved by jointcards soldered to the boards and endcards. These connections were checked from the electrical point of view before installation. A module contains three readout chains each having 36 chips. One of the endcards was connected to the motherboard through a 17 pin connector [10] carrying the digital and analog supply voltages, the ground and two gate signals to each readout chain. This end of the chipmodule was called the gate end. The other endcard was connected to the motherboard through two 24 pin connectors [11] carrying two reference voltage lines, one ground line, 7 data output lines, one clock and one reset line for each chip column. A complete readout module is shown in Fig. 6. The black spots are the chips covered with globtop.

The modules were mounted vertically inside the gas volume of the chambers between two meshes protecting the readout electronics from sparks and external pickup in the chamber. The upper (gate) end of the module was fixed by a screw and the flatness of the module was maintained by a spring-loaded fixation at the lower end of the module.

The motherboards on each side were glued into the chamber frame and carried all connections to the outside of the chamber. The part of the motherboard on the gate end, outside the gas volume of the chamber, was holding the gate and supply voltage distribution cards (gateboards). The gate signals to the chips were standard TTL signals and the digital and analog supply voltages were each

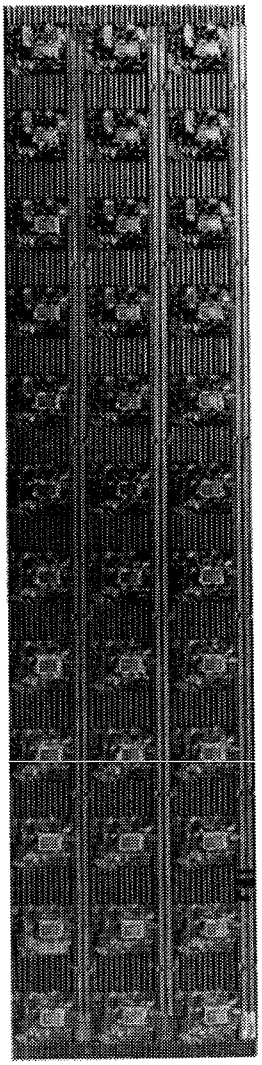

Fig. 5. Fully assembled board containing 36 naked chips.

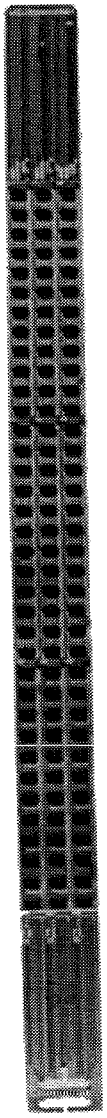

Fig. 6. A complete readout module.

+ 5 V. The voltage drops over the 600 mm long lines on a board were about 200 mV and the currents drawn were about 4 and 1 mA per chip on the analog and digital lines, respectively. This resulted in a power dissipation of about 54 W/chamber giving rise to an increased temperature in the flowing gas of about 2°C. The motherboard on the DSP side housed the electronics for distributing the reference voltages, clock, reset and signal processors which will be described in detail in the next paragraph.

4. The DSP system

4.1. Requirements

The design of the chip readout system was based on the requirements imposed by the multistep-avalanche pad chamber and the WA98 data acquisition system. In order not to contribute significantly to the overall event readout time, the event builder should, not later than a few milliseconds after an event trigger, have access to the data.

This amount of time had to include the reduction of the data volume. Event simulation codes showed that in the most central Pb + Pb reactions at 158 A GeV only 4% of the pads would deliver signals above their pedestal levels. During normal data taking, only such zero-suppressed data, together with the associated pad identity numbers are delivered to the event builder. Since the pedestal values differed between the pads, and also showed a slow change with the overall conditions of the chamber, individual values should be determined by measurements. Thus, different modes of readout should be possible. It was also required that the readout system should have a simple data and control interface, well suited not only for connecting to VME but also to microprocessors and general digital I/O PC boards during development and test.

4.2. Layout of the system

Parallel processing of primary data is exploited to the limit: each of the three vertical columns of chips on a module is handled by a separate DSP. In

order to maintain the correspondence with the three readout chains per module, three DSPs are mounted on a detector DSP board. Each detector DSP board is coupled to the motherboard at the bottom end of the readout chain in the pad chamber by a 96 pin EUR connector. Along the bottom runs a 64 line flat cable differential bus for data/command transmission and a 6 line daisy chain cable for signals between neighboring detector DSP boards. The arrangement is schematically shown in Fig. 7.

Each DSP controls the chips of its chain, reads out the data for each pad, compares with individual threshold values and finally, if above the threshold, delivers a six bit non-zero ADC value together with a 18 bit wide individual pad identity number. A 2*k* deep, 24 bit wide, fast FIFO for each DSP is the local destination for the data. The output sides of the FIFOs are connected via differential drivers to the bus cable which ends in a global 8*k* deep FIFO located on a master DSP board, located up to 10 m from the chamber, close to the data destination. Separate clocks on each detector DSP board are used to transmit the data sequentially from the FIFO buffers of the individual slave DSPs with a clock speed of 10 MHz.

4.3. Detector DSP board

The board layout contains three identical segments, one for each of the three readout chains. One such segment is schematically shown in Fig. 8. The DSP board is realized in a four-layer design with conventional hole mounted assembly. The two outer layers carry connections between the components, the two inner layers serve as ground and the voltage plane.

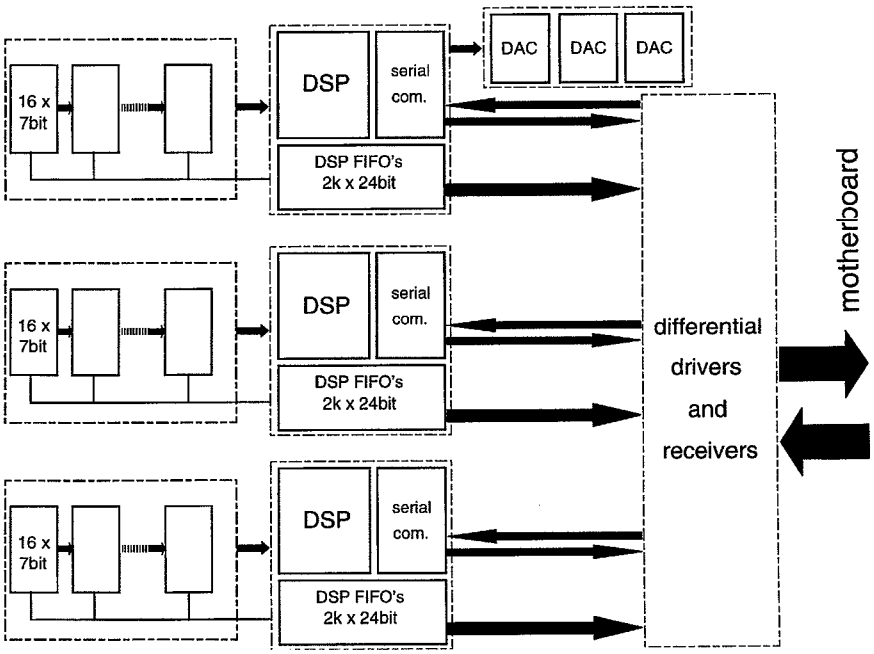

Fig. 7. The layout of the detector DSP board.

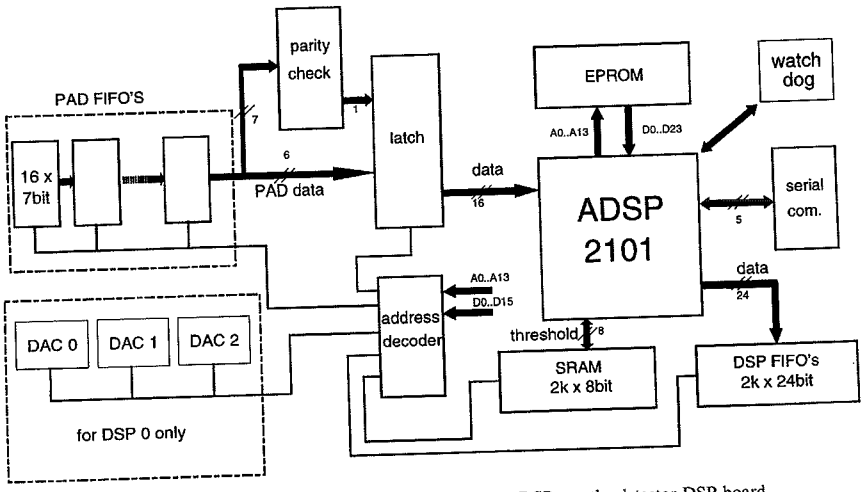

Fig. 8. The electronics block scheme for one of the three DSPs on the detector DSP board.

The main component in each segment is the ADSP2101 digital signal processor from Analog Devices. This DSP has a 16 bit data bus and a 24 bit program bus. After a power-up reset, the DSP loads its program from an EPROM. To prevent a possible deadlock situation a so-called watch dog is built in which resets the DSP if the program runs out of normal flow. After a readout signal is received from the master trigger electronics, each detector DSP sends 16 clock pulses, one for each pad, to control the analog multiplexer, the flash ADC and shift register, parallel to all chips in a chip chain. The clock pulse frequency is chosen between 50 and 500 kHz for optimum resolution. Subsequently, the digitized pad signals are stored in the 16 channels deep seven bit wide chip FIFO buffers. During the readout process the 7 bit data from the chip FIFOs are read by the DSP and the threshold value for the current pad is fetched from a static RAM. Depending on the readout mode a 24 bit data word with/without threshold subtracted or with/without parity check included will be stored in the 2k deep and 24 bit wide DSP FIFO.

Three DACs with 12 bit resolution and 5 V range are used to supply the trigger level voltage to the chips and ADC high/low reference voltages which are common for a chain of chips. The level accuracy of 2.5 mV is well below the ADC resolution of about 26 mV. The DACs are controlled on each detector board by one of the DSPs via the serial communication port.

4.4. Master DSP board

The master DSP board, shown in Fig. 9, serves as a communication junction for data and control communication. It carries one DSP, differential receivers and an 8k deep 24 bit wide "master FIFO buffer". All communication to or from the readout system is maintained via 16 bit data and 20 command and status lines in parallel. The pad data stream is totally controlled by status signals without any action by the DSP. The master DSP decodes commands for threshold and DAC settings, readout mode and conversion time of the chip ADCs and then distributes the information to and from the 75 detector DSPs via serial transmit and receive lines.

4.5. Performance

The readout time is estimated for the worst-case event with about 32 ADC values per DSP above

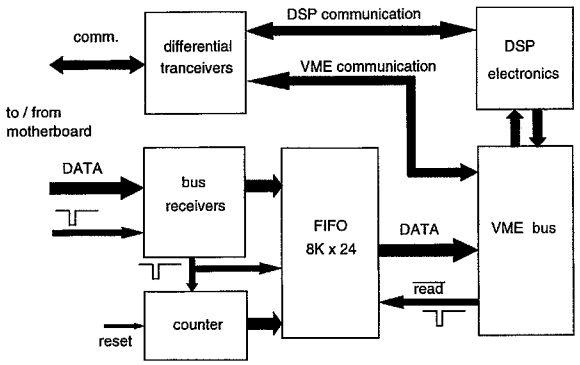

Fig. 9. The layout of the DSP/VME interface board.

threshold, which corresponds to 200 charged particles detected in the whole pad chamber. The time needed to read out a full chain of chips connected to one DSP and to process the data is about 180 μs, based on three clock cycles of 80 ns per word. Adding 16 × 2 μs conversion time and some initializing commands, the minimum time needed to store all data in the DSP FIFOs is approximately 220 μs. Thirty-two ADC values per DSP above threshold and 25 DSP boards each having three DSPs give 2400 data words to be transferred from the DSP buffer to the master buffer which takes another 240 μs at the readout speed of 10 MHz. The readout time thus amounts to roughly 460 μs. A test measurement on the DSP ready signal on the detector board for events with 32 ADC values per DSP above the threshold confirmed the expected transfer time of about 300 μs to the DSP FIFOs. Transfer of all pad values is sometimes required, e.g. for the measurement of the ADC pedestals in the "pedestal mode". Then the transfer of data runs in full speed until the master buffer is full. After that the transfer is controlled by the master "FIFO full" flag depending on the VME readout speed.

4.6. CPV version

Besides the pad chamber, the DSP readout system was applied to the about 10 m^2 large streamer tube wall [12] which served as charged particle veto detector for the photon calorimeter in WA98. This system used a version of the frontend chip, which had a modified analog part but identical digital part [7]. The detector wall was covered by about 50 000 pads. A varying number of 60–70 chips were connected via readout chains of up to 8 m length to one of the three DSPs on each of the 17 detector boards. As compared to the 1 m long readout chains required for the avalanche pad chamber, the larger padsize and thus less dense package of chips required much longer signal lines. The major problem appeared to be the attenuation of the clocksignal over the length of the readout chain. Fast signal repeaters were implemented accordingly. In addition, the termination of the transmission lines was much more critical than required for the short distances of 4 cm between neighboring detector boards on the pad chamber.

5. The VME system

5.1. General

The data acquisition system (DAQ) [13] of the WA98 experiment exploited the possibility of distributed computer power, parallel processing and

modularity offered by VME. Seen from the data acquisition system, the readout of the two MSACs behaved as one remote slave process which for each event was given the address and width of a buffer. The number of data words is transferred to the main DAQ by the slave process upon the end of its task. The slave process then waited for the next external trigger by polling.

At the recognition of a trigger, a veto level was set to inhibit pile-up and control start signals were sent to the FIFO chain. As soon as the master FIFO was not empty, the transfer of 24 bit data to the current event buffer could run at full CPU speed until the FIFO empty flag raised. Besides the event data stream, individual thresholds for each pad channel, trigger levels and reference voltages were communicated by the slave process.

5.2. The hardware

The slave process was executed in a Motorola MVME162 CPU board with a 25 MHz 68 040 processor. This board can host two 32 data bit wide "Industry Pack (IP) modules" [14], i.e. printed circuit boards, about the double size of a credit card, with standardized mechanical, electrical and logical interface towards the host and 50-pin flat cable connectors for external use. The complete MSAC VME data handling system is shown in Fig. 10.

The detector readout system assumed one chain for each MSAC. A 32 bit IP module with bus transceiver and latch circuits controlled by an AMD MACH 210 10 ns PAL was designed. As described above, the 24 bit data output from the master FIFO was separated into two 16 bit transfers by the control logic on the master DSP board.

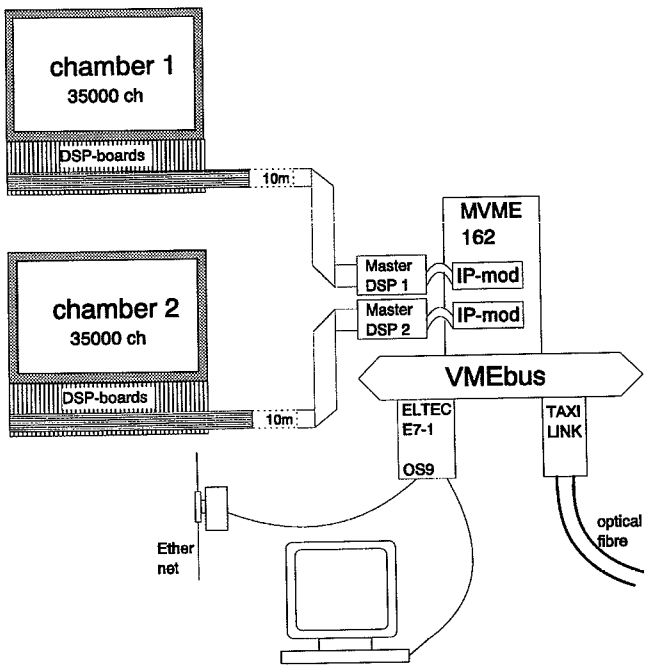

Fig. 10. The complete MSAC VME data handling system.

In order to reduce CPU clock cycles, the full-width was reconstructed within one normal IP clock cycle of 125 ns and sent to the event buffer as 32 bit data.

6. Electronic performance tests

The performance of the Multistep Avalanche Chambers equipped with this readout system will be described in a forthcoming paper. Here we concentrate on the electronic noise performance. The test results presented here were taken in a bench test with one complete readout module containing 1728 readout channels. The digitalization of the data is done in a six bit nonlinear flash ADC [7]. The first 16 steps of the ADC have a linear response while the remaining 48 steps have a quadratic response. The choice of the linear response at the low end of the scale is to have the same sensitivity regardless of the value of the pedestal. The reference voltages were thus chosen such that the pedestals of all channels were in the linear region of the ADC scale. During the tests this corresponded to values of the reference voltages of 1.7 and 3.2 V, respectively. These settings of the reference voltages correspond to a sensitivity of the ADC of about 3 fC/step on the linear part of the scale.

The system was operated with a random trigger to record the pedestal values and widths due to the noise of the full electronic system. The uniformity within one chip is satisfactory except for three channels located underneath the gate lines on the gate board. The TTL gate signal induces charge on the pads even though a signal of opposite polarity was run parallel to the gate signal to minimize the effect. The induced charge causes a slight broadening of the pedestal peaks for these three specific channels. Evidently, the screening effect of the groundplane is not enough to prevent influence from the gatepulses.

The mean value and width of each pedestal distribution, as shown in Fig. 11, were determined from Gaussian fits. Fig. 11a shows the distribution of the mean values of the pedestal peaks for all channels on a module. The used settings of the reference voltages resulted in a distribution of the mean values peaked around channel 11 with a width of about three channels. This number is a measure of the channel-to-channel variation of the system. Fig. 11a clearly demonstrates the good uniformity of the pedestal values over the full board. Fig. 11b shows the distribution of the widths of the pedestal peaks for all channels on a module. The main peak corresponds to the pads not affected by the induced charge from the gate signal. The mean value of this peak as well as the width, determined from a Gaussian fit to the distribution, are 1 and 0.3 channels, respectively. The second peak in Fig. 11b corresponds to the pads underneath the gate lines. This peak shows a larger

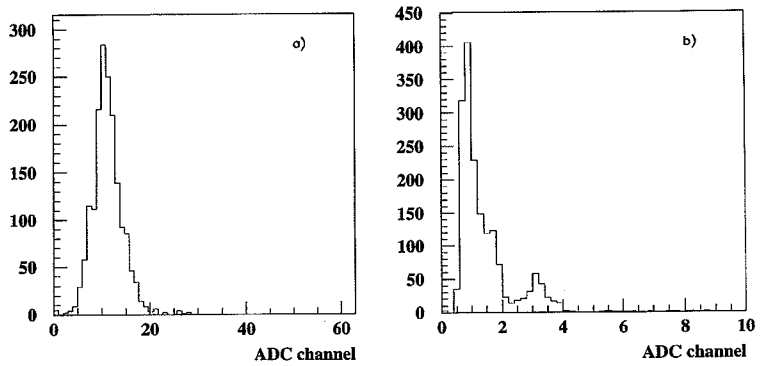

Fig. 11. Distributions of the mean values (a) and the widths (b) of the pedestal peaks for all chips on a board.

mean value (three channels) and a larger width (0.5 channels) as compared to the main peak. A different routing of the gate signal would most probably solve the problem of the induced charge on the pads thus resulting in a single-peak located at the position of the main peak of Fig. 11b.

The threshold value of each channel is determined online from the pedestal distributions. The numerical procedure was to sum the content of each pedestal distribution, starting at channel zero, until 90% of the integral was accumulated. The upper end of this channel was chosen as the threshold of that specific channel. This procedure resulted in a threshold setting equal to the mean value of the pedestal distribution plus 1.5 channels on the average. With the actual reference voltage settings it corresponds to a sensitivity of about 4.5 fC. This results in a few percent fired pads, due to noise. Choosing the threshold at the mean value plus 0.5 channels would increase the sensitivity to about 1.5 fC but at the expense of about 30% fired pads which was unacceptable due to the heavy load on the DAQ.

Two MSAC detectors, equipped with complete readout systems, were installed and operated in the WA98 tracking system at the CERN SPS. One chamber contained 36 288 readout channels (21 chipboards) and the other 34 560 readout channels (20 chipboards). The performance of the electronics, mounted inside the gas volume, was consistent with the test results obtained in the bench tests.

7. Summary

A 70 000 channels pad readout system for multistep avalanche chambers, based on a specially designed readout chip, was installed and operated in the WA98 experiment at the CERN SPS. The requirement of minimal thickness was achieved by the use of the COB mounting technique. This is the first time this technique is used for large-scale fabrication of electronics in a high-energy physics experiment. Experiences from design, construction and mounting and results from testing procedures have been discussed. The performance tests of the full system confirm the design goals of high uniformity, reliability and sensitivity. The achieved numbers were a few fC for the channel to channel variation and about 4.5 fC as a lower detection limit of the collected charge. No chips have failed during several weeks of running under experimental conditions. The design of the DSP readout system was based on the requirement of about 4% occupancy. This amount of data should be available by the VME system no later than after a few ms after the event trigger. This goal was achieved with a powerful zero-suppression already at the detector. The zero-suppressed data was transferred to the VME-based WA98 data acquisition system via 32 bit custom designed IP modules.

Acknowledgements

This work was supported by the Swedish National Science Research Council (NFR), the Swedish Board for Planning and Coordination of Research (FRN), the Dutch Stichting voor Fundamenteel Onderzoek der Materie (FOM) and the Swiss National Fund.

References

[1] A. Breskin et al., Nucl. Instr. and Meth. 161 (1979) 19.
[2] A. Breskin et al., Nucl. Instr. and Meth. 178 (1980) 11.
[3] G. Charpak et al., Nucl. Instr. and Meth. A 274 (1989) 275.
[4] M. Izycki et al., Nucl. Instr. and Meth. A 310 (1991) 98.
[5] L. Carlén et al., Nucl. Instr. and Meth. A 391 (1997) 492.
[6] L. Carlén et al., Nucl. Instr. and Meth. A, accepted for publication.
[7] C. Barlag et al., Nucl. Instr. and Meth. A 406 (1998) 299.
[8] Xicon AB, IDEON SE-205 12, Malmö, Sweden.
[9] National Instruments, 6504 Bridge Point Pky, Austin, TX 78730-5039, USA.
[10] MOLEX 22-01-2175.
[11] AMP 1.0 FPC connector 2-487951-4.
[12] R. Albrecht et al., Nucl. Instr. and Meth. A 276 (1989) 131.
[13] B.W. Kolb, M.L. Purschke, GSI Scientific Report 1994, GSI 94-1, March 1995, ISSN 0174-0814, p. 291.
[14] IndustryPack and IP are trademarks of GreenSpring Computers, Inc.

Paper II


ELSEVIER

Nuclear Instruments and Methods in Physics Research A 412 (1998) 361–373

NUCLEAR INSTRUMENTS & METHODS IN PHYSICS RESEARCH Section A

Performance of multi-step avalanche chambers equipped with two-dimensional electronic readout

L. Carlén[a], K. El Chenawi[a,*], K. Enosawa[b], S. Garpman[a], H.-Å. Gustafsson[a], M. Kurata[b], H. Löhner[c], M. Martin[d], Y. Miake[b], Y. Miyamoto[b], H. Naef[d], P. Nilsson[a], S. Nishimura[b], J. Nystrand[a], A. Oskarsson[a], L. Österman[a], I. Otterlund[a], E. Perrin[d], L. Rosselet[d], J.M. Rubio[d], S. Sato[b], K. Söderström[a], N. Solomey[d], E. Stenlund[a], T. Svensson[a], S. Vörös[d], K. Yagi[b], Y. Yokota[b]

[a] *Division of Cosmic and Subatomic Physics, Lund University Box 118, SE-22100 Lund, Sweden*
[b] *University of Tsukuba, Tennoudai, Tsukuba 305, Japan*
[c] *KVI, University of Groningen, NL-9747 AA Groningen, Netherlands*
[d] *University of Geneva, CH-1211 Geneva 4, Switzerland*

Received 10 February 1998; accepted 26 February 1998

Abstract

We have developed large area multi-step avalanche chambers with electronic readout for tracking in a very high multiplicity environment in the WA98 experiment at the CERN SPS. The operational characteristics of the detection system is reported. The reconstruction efficiency of the chambers varies with the density of charged particles in the range of 91–96%. The position resolution has been found to be 0.5 and 1.7 mm in the horizontal and vertical directions, respectively.

PACS: 29.40.CS; 29.40.GX; 07.50.QX

Keywords: Multi-step avalanche chamber; MSAC; Pad readout; Electronic; Tracking; Position resolution; Efficiency

1. Introduction

The main goal of the WA98 experiment [1] is to investigate highly excited nuclear matter by measuring photons and hadrons in Pb + Pb collisions at 158 A GeV. Two spectrometer arms (Fig. 1) placed after a large 2 Tm dipole magnet, measure hadrons around midrapidity. The right arm consists of six Multi-Step Avalanche Chambers (MSACs) [2–6] with optical readout and a Time-Of-Flight (TOF) wall, while the left arm contains two MSACs and two planes of streamer tube detectors all with electronic pad readout [7,8] and a TOF wall. This paper describes the MSACs equipped with a novel electronic pad-readout

* Corresponding author. Tel.: 46 46 222 4767; fax: 46 46 222 4015; e-mail: karim@kosufy.lu.se.

0168-9002/98/$19.00
PII: S0168-9002(98)00412-4

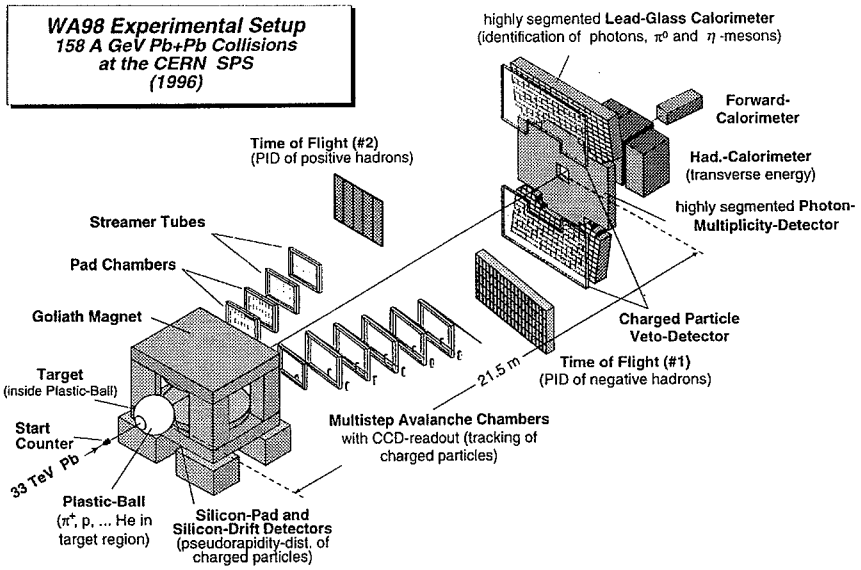

Fig. 1. View of experiment WA98.

system and their performance under experimental conditions. These chambers will be referred to as the pad chambers.

For many of the proposed hadron observables (for example particle interferometry, transverse momentum spectra, mass-shift of the ϕ-meson, etc.) it is crucial to be able to perform reliable tracking in a high particle density environment. Combinatorial problems prohibit detectors with position sensitivity in only one dimension. Position sensitivity in two dimensions provides space points of tracks without ambiguity. Combinatorial difficulties, however, may arise when space points are combined to reconstruct tracks. Accurate track coordinates are required to master such difficulties with a minimum number of tracking stations. A charged particle track passing through any chamber must be registered with high efficiency and low contamination due to noise. Spurious hits may be registered e.g. due to electronic noise or X-ray and γ radiation. Excellent position resolution in two dimensions can compensate for unavoidable limitations in detection efficiency or the discrimination of spurious hits.

In experiments like WA98 studying rare signals, the aim is to operate at highest possible event rates. Currently Time Projection Chambers (TPC) are the most advantageous detectors for tracking at high multiplicity due to the continuous three-dimensional track images. However, a drawback of a TPC is the long drift and readout times. Our approach has been to build a large acceptance tracking system based on planar tracking stations, read out with high granularity. The space points obtained along the tracks retain superior pattern recognition, characteristic of three-dimensional tracking. The MSACs were chosen because of their high gain (allowing simple readout electronics), their position sensitivity in two dimensions and their inherent drift delay which allows gated operation at high event rates.

The basic principle of the pad chamber is to create avalanches from electrons that are liberated by the primary ionization caused by a charged

particle traversing the gas volume of the chamber. The resulting electron cloud is collected on small readout pads. Due to diffusion, the cloud of electrons will spread out and by choosing an appropriate pad size, the electron cloud will be collected on several pads. Thus, the centroid of the electron cloud can be determined with a position resolution well below the size of the pads.

Due to the vertical magnetic field, the momentum was obtained from the trajectory, projected onto the horizontal plane. Thus it was desirable to have the best position resolution in the horizontal direction (ca. 1 mm), while the vertical coordinate, which is basically of importance for pattern recognition, would be sufficiently well determined with a more modest resolution (ca. 3 mm).

In order to optimize the readout system, a series of prototype tests were performed providing input for system simulations [9]. It was shown that pads with the size of $1 \times 17\,mm^2$, arranged as in Fig. 2, would be geometrically adequate to sense the electron cloud on several pads in both directions. The very large number of pads (70 000) needed to cover the total detector area (two pad chambers) put extraordinary demands on the readout electronics. The front-end electronics had to be placed directly onto the backplane of the detector. Since the dimensions of the pads are of the same order as the desired position resolution, it is sufficient to read out the pulse height of each channel with a non-linear 6-bit ADC. Low-power, highly integrated front-end electronics could thus be used which made the large number of channels affordable. We describe the readout chips, and the full electronic system in separate papers [7,8]. Here we discuss the chamber-related aspects of the readout electronics and the operational experiences from two, full-scale chambers used in the Pb-beam experiment in 1996.

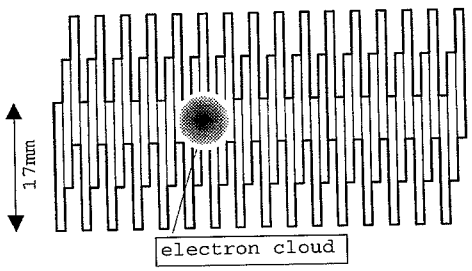

Fig. 2. Schematic illustration of the pad plane.

2. The multi-step avalanche chamber

2.1. Description

The MSAC is made of eight parallel mesh planes dividing the detector volume into different gaps. The stainless-steel meshes have wires with 50 μm diameter and 500 μm pitch. The meshes were glued onto frames made of a light composite material, vetronite and honeycomb. The chambers ($120 \times 100\,cm^2$ in size) were designed and built by the University of Geneva, Switzerland [6]. A schematic drawing of the chamber is shown in Fig. 3. The chamber has double mylar windows, flushed with Argon to prevent air and water vapour to reach the active volume of the chamber where a mixture of Neon 97% and Ethane 3% was flushed at 20 l/h. It was found (see Section 2.3) that even a very small contamination of water vapour strongly reduced the net yield of electrons in the chamber.

An ionizing particle traversing the chamber, liberates electrons in the ionization gap (I). The electrons drift towards the first amplification gap (A1), where an avalanche with an amplification up to a factor 10^3 in the high electric field between the meshes is obtained. The electrons reach the gate gap (G) after a drift time of about 700 ns. During this time the trigger electronics generates the gate signal for the chamber. Gap G has a reversed field of about 100 V/cm. When the gate arrives, a pulse of about 200 V and 2 μs length is applied to mesh 4 which changes the field direction in G to allow the electrons to drift through. The second amplification gap (A2) provides a slightly lower amplification than A1. The last two gaps are drift gaps of equal width and the meshes 7 and 8 serve the purpose of protecting and shielding the pad plane from sparks in A2 and pickup from the high voltage gating of the chamber. Finally, the electrons are collected on the pad plane which consists of rectangular gold-plated copper pads, each $1 \times 17\,mm^2$ arranged in a staggered pattern as shown in Fig. 2.

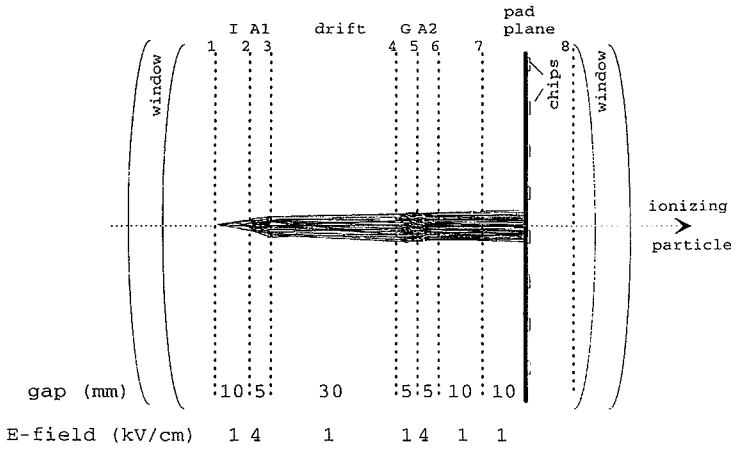

Fig. 3. Schematic drawing of the chamber.

The gain and transport of the electrons through the chamber is strongly dependent on the electric field between the meshes. A uniform response over the whole detector area requires flat and parallel meshes. This was obtained by placing spacers between the meshes in the amplification gaps. A lower amplification within 5 cm around the edges of the chamber was found. This was due to a slightly increased gap width close to the frame. Thus, the chamber was not instrumented in this area. Spark breakdown at the spacers was a limiting factor when operating the chamber with P10 (Argon +10% Methane) gas. This made it necessary to operate the chamber with a gas mixture that allowed avalanche multiplication at much lower voltage. A mixture Neon + Ethane (3%) made it possible to operate the chambers without sparks at the spacers. The quencher concentration used was lower than desired, resulting in a poorer gain with this gas mixture (at tolerable spark risk) than revealed by the prototype work with P10.

2.2. Sparks

To obtain the highest possible gain in the chamber it is necessary to apply as strong an electric field in the amplification gaps as possible. The limitation is due to the breakdown of the electric field resulting in a spark. Three different types of sparks are observed. (1) Sparks not in coincidence with the gate, at the edges or at specific points between the meshes due to mechanical imperfections, predominantly in A1 which has the strongest field. (2) Sparks not in coincidence with the gate, randomly distributed over the chamber area due to e.g. dust and radioactive impurities in the gas. This is also most likely to happen in A1 due to the stronger field. (3) Sparks in A2, in coincidence with the gate, originating from the ionization caused by a particle from a triggered collision, followed by a two-step amplification.

In order to increase the gain in A2, mesh 6 was also pulsed, which gave an increased field strength of about 200 V/cm when the cloud of electrons passed. Due to this, sparks of the first two types were eliminated in A2. The reduction in spark risk for the third type of sparks was not evident. The high-voltage gates of meshes 4 and 6 were identical in time but they had opposite polarity. By tuning the risetimes and amplitudes of the gate pulses one could minimize the electromagnetic influence from the gate pulses on the pads. High-voltage resistors

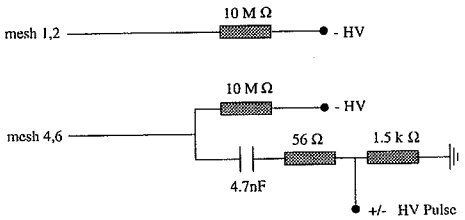

Fig. 4. Schematic drawing of the resistors and capacitors connected to the meshes.

and capacitors according to the schematic in Fig. 4 were applied to the meshes. The capacitors also ensured fast recovery time ($\sim$ 800 ms) after a spark.

2.3. Gas contamination

During the first operation with the chambers in the experiment, less gain was observed than in the test setup. A similar effect was also observed for the MSACs with optical readout and it was carefully studied for those. A major difference in the experimental setup compared to the laboratory setup was the necessity to keep the gas bottles about 25 m away from the chambers using plastic tubes for the gas distribution. A stainless steel tube and a plastic tube, 15 m long, were mounted in parallel to estimate the contamination of O_2 and H_2O [10]. A Teledyne O_2 and a Shaw H_2O analyzer were connected in parallel at the end of each tube. Argon was flowing through the tubes with a flow of 7.5 cm^3/s. Measurements were done over a period of one week for each tube. The H_2O contamination stabilized at about 120 and 3 ppm for the plastic and steel tube, respectively. From this result we can estimate the contamination, by assuming that it is proportional to the tube diameter, the tube length and inversely proportional to the flow. Thus, for our 25 m long plastic tube we expect a contamination of about 1500 ppm H_2O. The conclusion drawn from this analysis is that the amount of H_2O is non-negligible and plastic tubes were changed to stainless-steel tubes. This resulted in an increased charge collected at the pad plane by a factor of 2 at a given spark rate and particle density. We attribute the improvements mainly to reduced attachment losses with electronegative molecules (e.g. O_2), in particular, in the 2 cm drift from A2 to the pad plane, where the losses cannot be compensated by an increased gain in A2, as was the case for losses in the 3 cm drift gap.

3. The readout electronics

We emphasize the following chamber qualities and their implications on the designed readout system:

- The chamber itself has a position response, which is equal in both dimensions. We have optimized the readout to achieve a better position resolution in the horizontal plane (the bending plane of the magnet). We have also chosen a pad geometry which allows the electron cloud to be shared on several neighbouring pads, thus providing a unique and very safe cluster recognition.
- The high chamber gain, up to 10^5, allows readout with a moderate gain amplifier.
- The short duration of the inherently delayed charge-signal allows a gated, charge-integrator amplifier design. This provides a very noise-immune operation since the amplifier input is closed most of the time. The gate signal determines precisely the time of the charge collection. The timing is adjusted so that only electrons emanating from ionizations in the ionization gap are collected. There is also no need for complicated amplifier design for pulse-tail cancellation.

Taking all this together, we have been able to produce a low-cost, low-power readout system that can be implemented for a very large number of channels. The concept provides excellent conditions for clean measurements at high multiplicity. Due to the very low power consumption of 1.5 mW per channel for amplifier, AD-converter and data readout, it was possible to place the front-end electronics inside the gas chamber without any additional cooling. This allowed an extremely thin

(0.3% of a radiation length) backplane construction. The electronic readout system is described in Ref. [8].

The MSACs also provide some drawbacks. The main obstacle is their known tendency to spark. The most problematic sparks occur in the second amplification gap, for cases when the local charge becomes unusually large. Such sparks (see Section 2.2) are energetic and violent and they are a potential risk for damaging the readout electronics. In order to protect the electronics from the electromagnetic shock, in case of a spark, we have placed one mesh between the last mesh of the second amplification gap and the pad plane. Since the information is carried by the cloud of electrons this mesh allows the information carriers to continue their drift to the pad plane, while induction from sparks is effectively screened.

This additional mesh is crucial for the safe operation of the electronics in this dangerous environment. During six weeks of continuous data taking, no chips were damaged, in spite of sometimes frequent sparking. An additional grounded mesh was placed behind the readout electronics in order to shield against external pickup. It was experienced though, that parts of the electronics placed outside the chamber was strongly influenced by the sparks. Therefore, aluminum shield boxes had to be built around the data processing electronics, mounted on the outside of the chamber frame.

Another important feature of this type of chamber is the high-voltage gating, with a 200 V negative signal on mesh 4, in time for the passage of the electron cloud. Similarly, in order to achieve increased chamber gain, the second amplification step was pulsed with a 100 V positive pulse on mesh 6. Ideally, these gate pulses should end immediately after the passage of the cloud. However, the trailing edge of the gate pulse would then appear close to the leading edge of the chip-gate and thus provide a potential source of noise. Therefore, the chamber gate was kept open until the chip-gate indicated the termination of the charge collection.

The electromagnetic influence of the high-voltage gate pulses on the pads is effectively screened by the shield meshes. However, noise is generated on the ground lines which induces noise, in particular, on those pads located close to the ground traces. This is seen in Fig. 5 which shows the average pedestal value of all 36 chips in a readout chain. The pedestals of channels 2, 10, 11 in each chip are systematically shifted compared to the rest of the channels. The pads corresponding to the shifted channels are located next to the ground lines of the circuit board and under the shield plane of the chip-gate card. The channels belonging to the first and last chip of a readout chain show a large pedestal shift as can be seen in Fig. 5, since there the pads are located close to a large grounded area on the endcards.

By fine tuning of timing, risetime and amplitude of the two gate pulses (mesh 4 and mesh 6) one could minimize the influence from the gating of the chamber. This was however hard to achieve and maintain. A longer drift time between the last amplification gap and the pad plane would have reduced the influence of the chamber gating on the charge collection in the chips.

The first 16 steps of the ADC scale are linear while the remaining 48 steps have a quadratic response. In spite of the channel to channel variation due to external pickup, the pedestals could be adjusted inside the linear range of the ADC scale. No broadening of the pedestal peaks was observed due to operation of the electronics in the chamber, compared to bench tests of the electronics alone [8]. The influence of the chamber gate, however, broadened the pedestal peaks. We define the sensitivity as the minimal additional charge, at which the ADC value exceeds the threshold value. The threshold value is subtracted online by the zero-suppression processors [8]. The sensitivity of 4.5 fC achieved in the full-read-out system is the same as found in the bench tests. At this sensitivity, we observe an excellent noise performance and efficient online zero-suppression. Less than 1% of the channels show non-zero values due to noise. Thus, accidental cluster formation due to noise is negligible. For this reason we could very well have increased the sensitivity, but then it would have been impossible to accomodate the channel-to-channel variation of the pedestals inside the linear part of the ADC scale, (except for channels on chip 0 and 35).

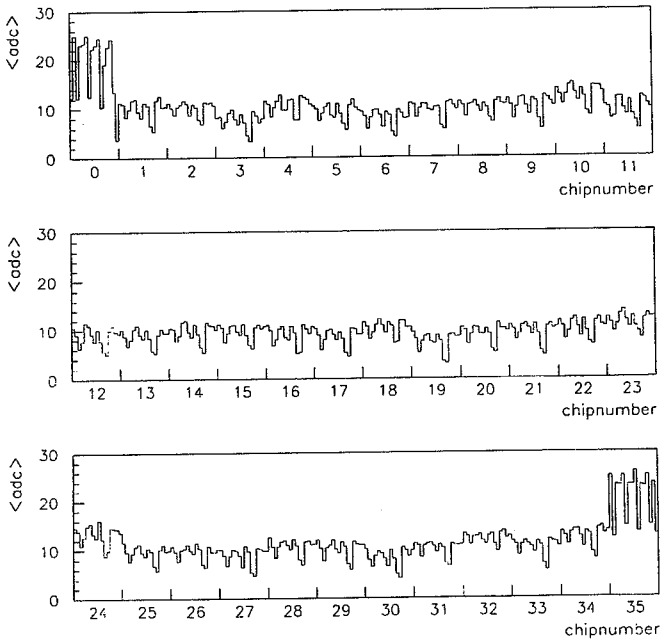

Fig. 5. The average pedestal value of 36 chips in a readout chain. Each chip contains 16 channels. Channels 2, 10, 11 within a chip are systematically shifted compared to the rest of the channels.

4. Results

4.1. MSAC operation

Two pad chambers were employed in the WA98 experiment at the CERN SPS in 1996. The chambers were instrumented with about 35000 readout channels each. We report here mainly on the performance of the chambers in this experiment with Pb-beam. Some aspects are also illustrated by data from measurements with secondary proton and muon beams from the SPS. Unfortunately, the time scale for the development of these chambers did not allow a dedicated beam test which would have been advantageous for precise determination of the position resolution. We thus deduce the resolution as well as the efficiency from experimental data.

As mentioned, the limitation in gas gain in the chamber is due to the spark rate in gap A2. The risk that an avalanche develops into a spark is a local effect in the direct vicinity of the charged particle track. One can therefore expect that the spark risk per traversing particle should be constant, at a given gain, regardless of the number of tracks passing through the chamber at the same time. This hypothesis is supported by the experiences at high multiplicity with Pb-beam where up to 50 charged particles pass through the chambers in a central collision. If we have a spark rate of one spark per 1000 single-track events, we expect one spark per 20 events in central Pb–Pb collision at the same gain. Due to this high spark rate the chambers were operated at less than half the proton-beam gain in order to have about one spark per 100 events. This

operation point is determined as a compromise between inefficiency due to signals being below threshold and inefficiency due to the whole chamber being insensitive for a while after each spark. The latter source of loss is easier to live with as it is just a loss of statistics, comparable to e.g. computer deadtime. We also know when a chamber is affected by a spark and can take that into account in the analysis.

Fig. 6 shows the number of found tracks (central collisions only) as a function of the time after a spark. No events at all are collected during the first 400 ms. This is due to the extended computer deadtime when the large spark events are processed (software limited to 45 000 ADC values from both chambers). Evidently, it takes another 400 ms until the chamber has completely restored the strong electric fields for full efficiency.

4.2. Cluster properties

Fig. 7 is a snap shot of the hit pattern in one chamber for a central Pb + Pb collision. The left edge of the detector is at 9.5° from the beam and the right edge at 20°. Pads (narrow stripes in this representation) with an ADC value above threshold have been marked. All fired isolated pads are regarded as being caused by noise. Since their number is small, the probability for finding two horizontally adjacent pads fired due to noise is on the level of a few percent. Thus, even a cluster of two pads is a candidate for a valid particle hit and a cluster with at least three pads is a highly probable hit. Further discrimination of accidental clusters due to noise can be achieved by analysing the charge content and profile of the cluster which has a symmetric Gaussian shape for particle hits. In

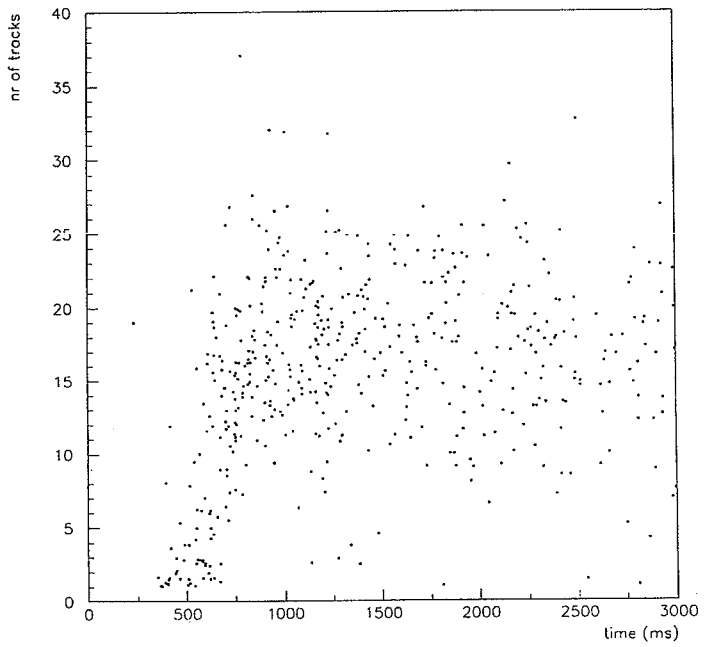

Fig. 6. The number of found tracks as a function of the time after a spark for central Pb + Pb collisions.

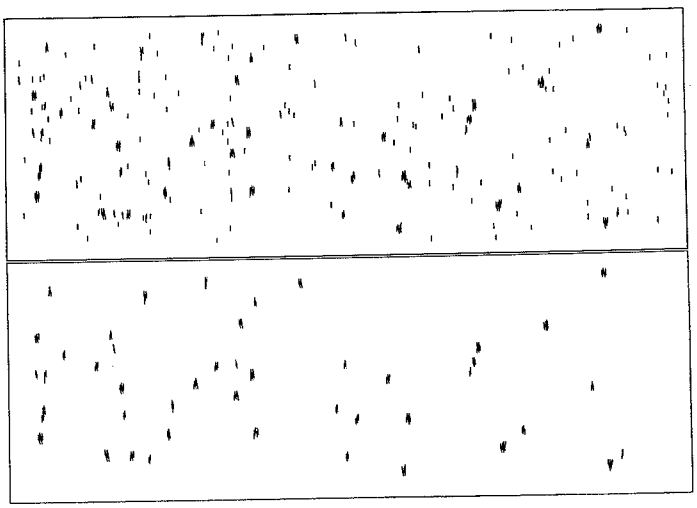

Fig. 7. A snap shot in one chamber of a central Pb + Pb collision. The upper panel shows the raw data while only pads belonging to accepted clusters appear in the lower panel. The panels display the full instrumented area of the chamber. The scale in x has been multiplied by two.

Fig. 7 the left part of the chamber is more densely populated than the right. This is due to the strongly forward-peaked angular distribution of charged hadrons.

As seen in Fig. 7 some clusters have an empty pad. This is due to incorrect online determination of the threshold value which sets a too high cutoff for the pads which due to pickup from the chamber gate have wider pedestals. The pedestals for the undisturbed channels are stable within ± 1.5 fC (our measurement accuracy). The external pickup conditions are not as stable and new threshold values were thus in general taken once per day.

As understood from Fig. 7 the low-noise background and the large amount of cluster information makes it straightforward to identify clusters corresponding to a charged-particle track. First-order cluster finding is basically a one-dimensional (horizontal) problem due to the pad geometry. A small fraction of found clusters may be caused by X-rays, γ-rays and neutrons. Such background only causes a valid signal if detected in coincidence with the event trigger. In heavy ion collisions this background can be fairly high, however, it did not cause a specific problem due to the strict demands that can be applied on the positions in the track reconstruction owing to the good two-dimensional position resolution.

Fig. 8 and Fig. 9 summarize the properties of clusters in one chamber corresponding to tracks which are unambiguously identified in the other tracking planes of the tracking system. Fig. 8 shows the distribution of the summed charge for clusters caused by a charged particle. The ADC scale has been calibrated and linearized before the sum is formed. The shape of the curve reflects the Landau distribution and the most probable value is at 160 fC which corresponds to 10^6 electrons. From this we deduce a net gain in the chamber of about 1.5×10^5. This is a factor two lower than the operational gain that was used for tests with muons and β-source.

Fig. 9 shows the distribution of the cluster size for clusters with at least three fired pads. One finds that five fired pads is the most probable cluster size. This is quite consistent with expectations from

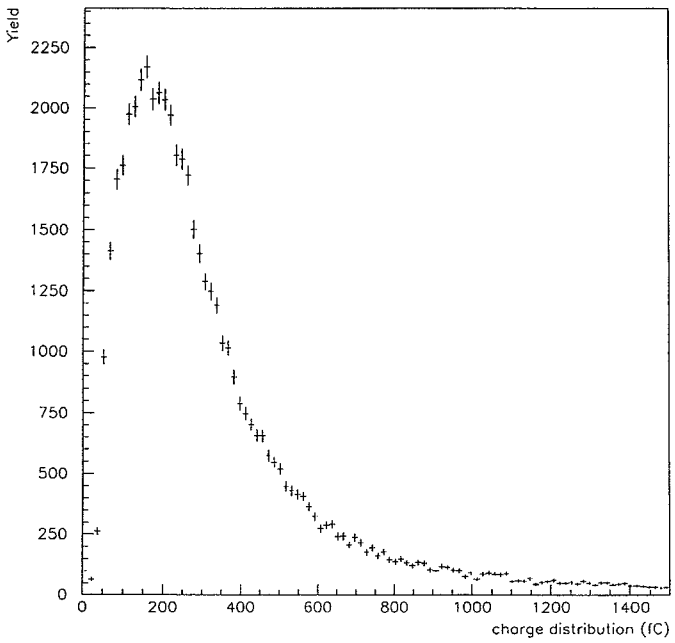

Fig. 8. The charge distribution for clusters belonging to reconstructed tracks in the tracking system.

simulations and bench tests which showed typical sizes of the electron clouds of 5 mm diameter. Since clusters can also include neighbouring pads in the vertical direction, the typical one-dimensional cloud size is a little less than 5 mm.

There is a correlation between cluster size and the total charge in the cloud, due to the threshold cutoff. Thus, Fig. 9 also reflects the Landau distribution of the initial ionization process. The fact that 3- and 4-pad clusters are less likely than 5-pad clusters indicates a good efficiency.

4.3. *Efficiency*

The detection efficiency was measured in the secondary muon background at the SPS and it was found to be 96% at a tolerable spark rate (1 per 1000 events). The efficiency of the chambers during experimental conditions with Pb-beam was studied by defining a good track from coordinates in one-pad chamber, two planes of streamer tube detectors and the time-of-flight scintillator array and then find the probability to observe a hit at the expected position in the pad chamber under study. This procedure revealed an efficiency (average over several weeks of data taking) of 91% for the best chamber. The other chamber had wider pedestals for some modules due to unstable grounding conditions and was thus more difficult to operate. With this chamber we observed an average efficiency of 81%. The ADC sum spectra (Fig. 8) as well as the cluster sizes (Fig. 9), are similar for both chambers. This indicates that they have similar intrinsic detection efficiency and we attribute the difference in performance to the unstable readout conditions caused by noise due to the gate pulses.

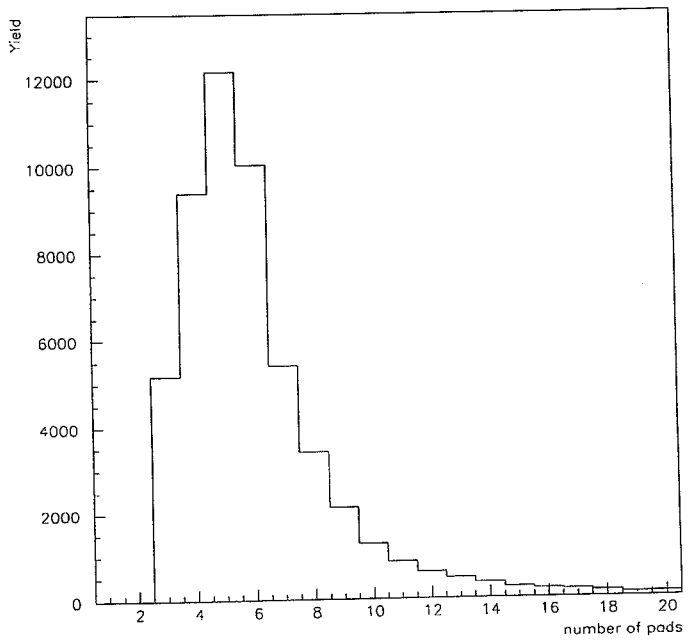

Fig. 9. Number of fired pads for clusters belonging to reconstructed tracks in the tracking system.

4.4. Position resolution

The position resolution was determined under data-taking conditions with a proton beam and the magnetic field switched off. Thus, well-isolated and straight-line tracks passed through the chambers. The chamber gain was adjusted similar to the gain during the Pb-beam run. Straight tracks were defined by the target position and the measured hit position in pad chamber 2. Subsequently, the expected position in pad chamber 1 was interpolated. The deviations between all hits in chamber 1 and the predicted hit are histogrammed in Fig. 10. Correctly associated tracks show up as the Gaussian peaks above the combinatorial background. The widths of the peaks are broadened due to the finite size of the target spot, the position resolution in pad chamber 2 and the multiple scattering in the air between the target and the chambers. Unfolding these effects yields an intrinsic position resolution of the chamber of 0.5 mm in the horizontal and 1.7 mm in the vertical direction. The two-track resolution has been estimated by simulations [9] and reveals that two tracks separated by 3.5 mm in the horizontal direction are resolved in 50% of the cases. The corresponding distance in the vertical direction is 8 mm. Due to the measured position resolution, not taken into account in the simulations, these distances are somewhat larger in reality.

5. Summary and outlook

The first experience in data taking with the pad chambers has proven that they provide clean and

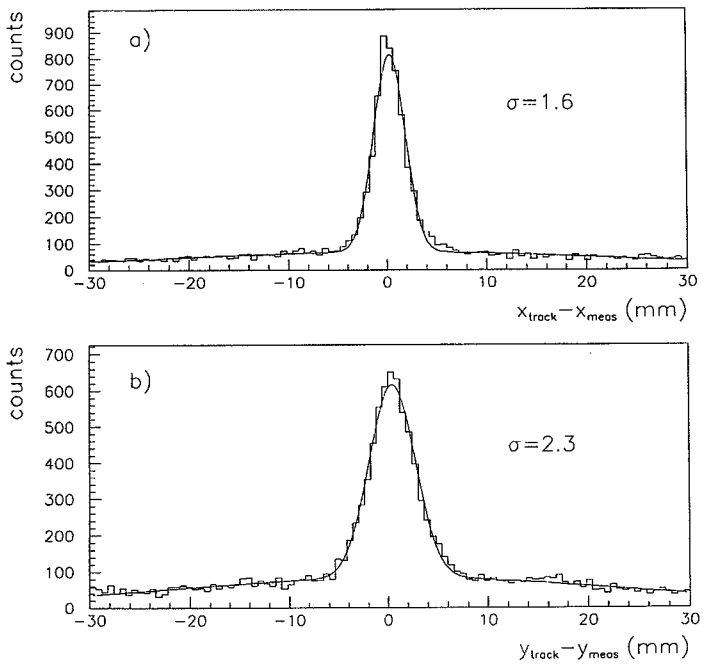

Fig. 10. Measured position resolution in the horizontal x-direction (upper part) and in the vertical y-direction (lower part).

reliable space-point information in a large aperture tracking system. The good performance for tracking at high particle density was demonstrated. The position resolution is equal to ± 0.5 mm in the horizontal direction and ± 1.7 mm in the vertical direction and the two track resolution in both directions is good. Each hit is characterized by rich information: charge content, charge profile, cluster size etc, which gives unique possibilities to acquire reliable track coordinates. The unique features of this readout system make these chambers advantageous for many purposes, either as stand-alone detectors as in our case, or as a pattern recognition complement, for a more conventional tracking system, hampered by combinatorial ambiguities when used at high multiplicity.

Due to the clean data provided by this system, the online data reduction was efficient. In spite of 70 000 channels in operation, electronic noise and pickup give rise to only about 300 pad values above threshold i.e. about 1 kbyte of data. The data readout and zero suppression allowed data of a full event from the pad chambers to be available at the event builder in less than 5 ms.

Considerable improvement in performance might be achieved by changing two essential features of the pad chambers:

- The gas with only 3% quencher content made the chamber operation difficult and the spark risk was substantially larger (at a given gain) than if a more standard gas mixture could have been used. We expect to be able to operate at larger gas gain with a larger quencher concentration. Even a factor 2 larger gain would bring the efficiency closer to 100%. The operation and

tuning of the chamber and the electronics would in that case become much less critical.

- Most problems encountered occurred for pads located close to ground traces on the chipboard, due to the high voltage pulsing of the chamber. This problem may be cured by rearranging the ground lines on the chipboards. In addition, the chamber gate should be seperated in time from the charge collection in the chips by a longer drift distance after the second amplification gap.

Acknowledgements

This work was supported by the Swedish National Science Research Council (NFR), the Swedish Board for Planning and Coordination of Research (FRN), the Dutch Stichting voor Fundamenteel Onderzoek der Materie (FOM), the Swiss National Fund, the Japanese Research-in-Aid for Scientific Research of the Ministry of Education, Science and Culture and the University of Tsukuba Special research Projects.

References

[1] Proposal for a Large Acceptance Hadron and Photon Spectrometer, CERN/SPSLC 91-17, SPSLC/P260.
[2] A. Breskin et al., Nucl. Instr. and Meth. 161 (1979) 19.
[3] A. Breskin et al., Nucl. Instr. and Meth. 178 (1980) 11.
[4] G. Charpak et al., Nucl. Instr. and Meth. A 274 (1989) 275.
[5] M. Izycki et al., Nucl. Instr. and Meth. A 310 (1991) 98.
[6] J.M. Rubio et al., Nucl. Instr. and Meth. A 367 (1995) 358.
[7] C. Barlag et al., Nucl. Instr. and Meth. A, 406 (1998) 299.
[8] L. Carlén et al., Nucl. Instr. and Meth. A, accepted.
[9] L. Carlén et al., Nucl. Instr. and Meth. A 391 (1997) 492.
[10] Gas Analysis for Multi-Step Avalanche Chambers, Internal Communication Report from the Geneva group.

Paper III

A large-acceptance spectrometer for tracking in a high multiplicity environment, based on space point measurements and high resolution time-of-flight

L. Carlén[a], K. El Chenawi[a], T. Chujo[b], K. Enosawa[b], S. Garpman[a], H.-Å. Gustafsson[a], M. Kurata[b], K. Kurita[b], H. Löhner[c], M. Martin[d], Y. Miake[b], Y. Miyamoto[b], H. Naef[d], P. Nilsson[a], S. Nishimura[b], J. Nystrand[a], A. Oskarsson[a], L. Österman[a], I. Otterlund[a], E. Perrin[d], L. Rosselet[d], J.M. Rubio[d], H. Sako[b], S. Sato[b], D. Silvermyr[a], K. Söderström[a], N. Solomey[d], E. Stenlund[a], T. Svensson[a], S. Vörös[d], K. Yagi[b], Y. Yokota[b]

a) Division of Cosmic and Subatomic Physics, Lund University
Box 118, SE-22100 Lund, Sweden

b) University of Tsukuba
Tennoudai, Tsukuba 305, Japan

c) KVI, University of Groningen
NL-9747 AA Groningen, The Netherlands

d) University of Geneva
CH-1211 Geneva 4, Switzerland

Abstract

A large acceptance tracking system, specially developed for tracking at very high particle densities encountered in ultra-relativistic heavy-ion collisions is described. The system is a combination of multi-step avalanche chambers equipped with electronic pad readout with high position resolution in two dimensions and streamer-tube detectors with pad readout, with coarser position resolution, that is sufficient for safe pattern recognition. A high resolution time-of-flight system (time resolution better than 90 ps) provides particle identification up to 8 GeV/c for pions and protons and pion/kaon separation up to 4 GeV/c. All detectors in the tracking system are read out with new, high performance integrated circuits. The system can operate at high event rates due to efficient zero suppression. The performance of the system for tracking under real running conditions with Pb-beam at 158 A GeV in the WA98 experiment at CERN is presented.

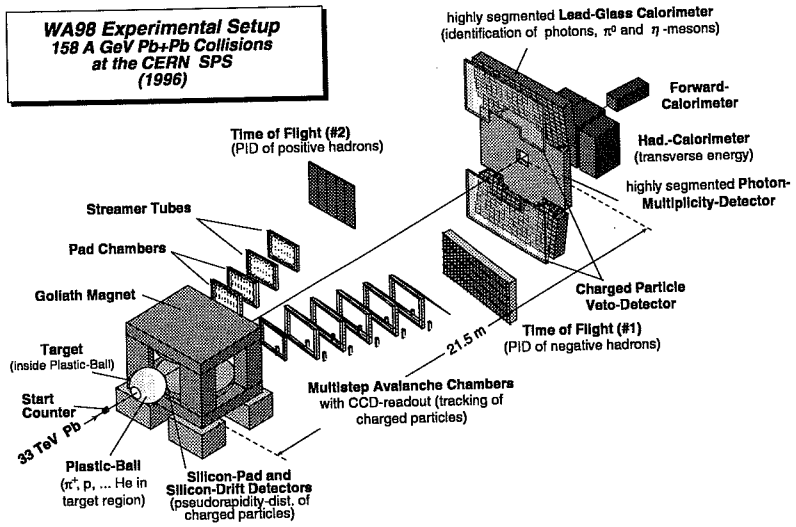

Figure 1: *WA98 experimental setup.*

1. Introduction

The use of heavy nuclei as projectiles in experiments at ultra-relativistic energies at the SPS presents new experimental challenges due to the very large particle multiplicities, which are an order of magnitude larger than encountered with light ion beams.

Some types of measurements, e.g. with high resolution electromagnetic calorimeters, can only cope with the high particle density by increasing the distance to the target since the shower diameter is fixed for a given material. Charged particle tracking, on the other hand, has to be performed as close as possible to the target, in order not to destroy the resolution by multiple scattering. In typical tracking detectors, e.g. gaseous ionization detectors, the ionization event in the gas has very small dimensions. Thus a very high track density can be handled by increasing the granularity in the readout system.

In order to resolve tracks at high multiplicity it is necessary to trace the particles in all three dimensions. In a Time Projection Chamber (TPC), the tracking in three dimensions is exploited to the limit with a continuously recorded track image. A drawback of the TPC is long drift times limiting its use at high collision rates. Thus other methods have to be developed, suitable for use in studies of rare signals. Planar tracking stations using crossed planes of tracking detectors which are position sensitive in only one dimension are inadequate due to combinatorial ambiguities in the determination of the coordinates along a track.

The system described here uses planar tracking detectors with short drift time and position readout in two dimensions. The target-detector distance provides the third coordinate. This technique allows data taking at high collision rates and preserves the good track recognition characterizing tracking in three dimensions.

The system is based upon Multi-Step Avalanche Chambers (MSACs) equipped with an ultra-thin electronic pad readout system with a very large number of channels. These detectors, in the text referred to as "pad chambers", give precise coordinates for momentum measurements while two planes of streamer tube detectors with pad readout provide a coarser coordinate measurement, adequate for track recognition. These systems use a new, specially developed integrated circuit which is used for readout of 83 000 channels in this detector system. The particle identification is done with a high resolution Time-Of-Flight (TOF) detector based on plastic scintillators, read out by Photo-Multiplier-Tubes (PMTs). The readout electronics is based on two custom made chips, the Time-to-Voltage Converter (TVC) and the Charge-to-Voltage Converter (QVC), both equipped with a switched capacitor Analog Memory Unit (AMU).

The tracking system was implemented as the second tracking arm (Fig. 1) in the WA98 experiment and it was used for the first time with the Pb-beam at 158 A GeV at the SPS in 1996. The first tracking arm in WA98 used the same tracking philosophy with planar, large area detectors read out in two dimensions with a very large number of pixels. These detectors are MSACs read out with CCD cameras, equipped with image intensifiers.

The aperture of the second arm tracking system is large, typically allowing about 30 particles per central event to be traced. Thus it is possible to obtain good statistics for single particle observables, and excellent performance can be achieved in studies involving particle correlations, e.g. like-particle intensity interferometry and resonance decay. Recent analysis of the data has shown that it is feasible to reconstruct the Δ^{++} resonance decaying into a pion and a proton.[1] In combination, the two arms allow measurements of decaying resonances into a positive and a negative particle. A particular focus of the experiment is to study the properties of the ϕ-meson from its decay into K^+K^-.

The three detector systems in the second tracking arm are new developments which utilize advanced and unique readout solutions with specially designed integrated circuits which are used here for the first time. The details of the detector systems have been extensively described in separate publications [2, 3, 4], while this paper concentrates on the performance of the system as a whole.

2. The detectors in the second tracking arm

The detector components in the second tracking arm are two planes of pad chambers, two planes of streamer-tube detectors with pad readout and one plane of time-of-flight detectors. Figure 2 shows a schematic top view of the tracking system. The location of the tracking stations with respect to the target and the magnet are indicated. The passage of a high momentum particle with positive p_x and a low momentum particle with a negative p_x through the system is also shown. Outside the magnetic field, the particles move in straight lines.

All five planes provide space coordinates for the traversing particles. The two planes of pad chambers (separated by 1.2 m) determine the direction of each track with high resolution for precise momentum measurements while the two planes of streamer-tube detectors and the TOF wall have sufficient position resolution for safe track reconstruction and for acceptable momentum resolution even if one of the pad chambers is desensitized due to a spark.

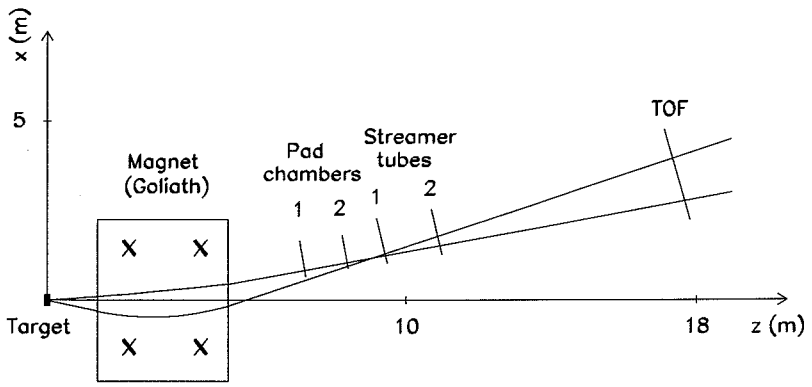

Figure 2: *Overview of the second tracking arm detector system. The flight path from the target to the TOF wall is about 18 meters.*

2.1 The multi-step avalanche chambers with electronic pad readout

The novel readout concept used in conjunction with the pad chambers is based on a custom-designed chip containing both analog and digital functions as well as ultra-thin mounting with the chip-on-board technique.[3] The detection efficiency of the chambers, when they are not affected by a spark, is in the range of 91-96%.[4]

The intrinsic position resolution is 0.5 mm in the horizontal direction and 1.7 mm in the vertical direction.[4] Due to the long flight path (7 m) from the target to the first pad chamber plane we find that the position resolution is limited by multiple scattering rather than the intrinsic position resolution of the detectors. The good position resolution is of great value in the tracking, since the multiple scattering between the pad chamber planes is small, thus allowing restrictive cuts in the track fitting, which is essential for tracking at high multiplicity.

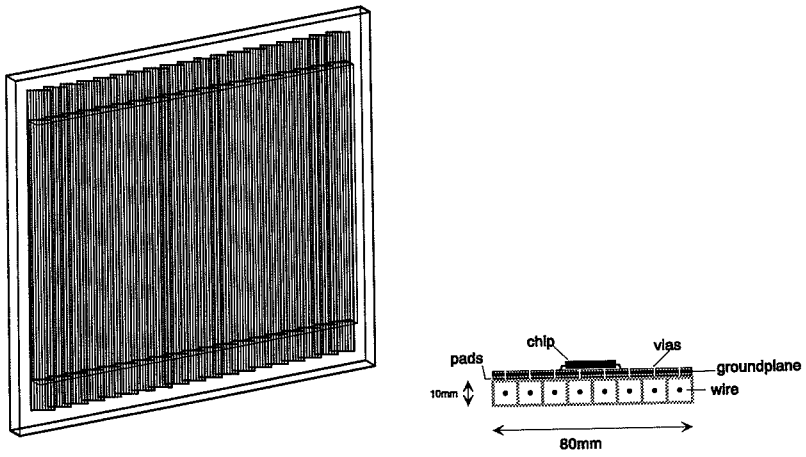

Figure 3: *The streamer-tube detector plane consisting of 19 streamer tubes, tilted with respect to the detector plane, and a cut view of one streamer tube.*

2.2 The streamer-tube detectors with pad readout

Streamer-tube detectors are in widespread use in high energy physics experiments due to their low cost, high gain and rugged construction suitable for large area coverage. Such detectors equipped with pad readout have been used in the earlier generations of the WA98 experiment (WA80 [5] and WA93 [6]), as large area charged particle multiplicity detectors with moderate position resolution. The streamer tubes were then operated at very high gain which allowed readout without further amplification. The amplifier stage of the readout chip developed for the pad chambers was modified in order to make it suitable for readout of pads on the streamer-tube detectors.[2] The streamer tubes could then be operated at lower gain, resulting in more stable operating conditions, still maintaining high efficiency of 90 to 98%.

A printed circuit board, with the sensor pads on one side and the readout chips with supply and readout lines on the other, is attached to the streamer-tube module. The streamer tubes were 1.20 m long and

each module contained 8 wire tubes (Fig. 3). Three connected circuit boards cover the full length of a streamer tube. The readout chips of several streamer-tube modules were connected together to form a long readout chain delivering data to the Digital Signal Processor (DSP) boards. These are of the same design and fabrication as used for the pad chambers.[3]

A large array of these streamer-tube detectors was also used as a charged particle veto detector in front of the high resolution lead glass calorimeter (Fig. 1). The streamer-tube detectors in the second tracking arm were read out with rectangular pads (7x22 mm^2) with the longest side parallel to the tube. The detector modules were positioned at 30 degrees with respect to the detector plane. This served the purpose of minimizing the risk that a particle passes through the tube walls only and not through the gas. These walls occupy 10% of the streamer tube width. The resolution across the wires is in the first approximation determined by the wire distance (the tube pitch is 10 mm), but improved by the tilted arrangement of the detector modules. With the pulse height measurement, it was possible to determine the avalanche positions along the wires with fairly good resolution. The position resolution achieved in the streamer-tube planes has been found to be 3 mm in the horizontal and 6.5 mm in the vertical direction.

2.3 The time-of-flight detectors

The time-of-flight of detected particles provides particle identification when combined with the momentum information. The flight path is about 18 m and together with the extremely good time resolution, (better than 90 ps), this allows particle separation at the 4σ level, up to 4 GeV/c for π/K separation and up to 8 GeV/c for π/p identification.

The time-of-flight measurement is started by a gas Cherenkov counter placed in the beam (time resolution 30 ps [7]) about one meter upstream from the target. The beam intensity with Pb ions is a few 10^5 ions/s which allows time measurement for the passage of individual beam particles. From this setup the time of the collision in the target is obtained.

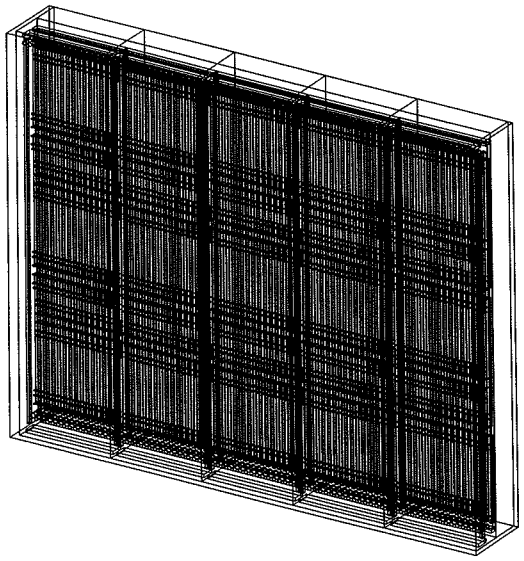

Figure 4: *The time-of-flight detector as it is modeled in GEANT. It consists of five panels, each with 32 columns and 3 rows of scintillators, resulting in a total of 480 scintillator slats.*

The TOF wall (Fig. 4) covers an area 2450 mm wide (160 columns of scintillators) and 1924 mm high (3 rows of scintillators). Therefore, the area is filled with 480 slats of scintillators (BICRON, BC404, 1.5 cm in width, 1.5 cm in depth). Each scintillator slat has PMTs (Hamamatsu, R3478s) on both ends. Scintillators with two different lengths (637.7 mm and 433.9 mm) are assembled in an alternating fashion in order to avoid geometrical conflicts between the PMTs of neighboring slats.

The TOF wall and its electronics is primarily designed to be used in the PHENIX experiment at RHIC.[8] The front-end electronics of the TOF wall was designed to sample the TOF signals at the bunch crossing frequency (9.4 MHz) of RHIC and to store them during the first level trigger latency of 4.24 μs, corresponding to 40 RHIC bunch crossings. The signal timing from the PMT is determined by a leading edge discriminator followed by a TVC. The charge information is converted to a voltage by a QVC. The analogue voltages from the TVC and the QVC

are stored by a switched capacitor AMU which stores the information during the latency and buffers up to five accepted events. The stored voltages are digitized by a 12 bit 1.25 MHz ADC.

The hit position in the vertical direction (along the slats) is derived from the time and amplitude difference observed in the signals, read out in the two ends of the slat. The tracking analysis has revealed a position resolution in the TOF wall of 12.5 mm in the horizontal and 26.4 mm in the vertical directions.

3. Track reconstruction

The track reconstruction procedure has two steps. In the first step, each detector plane is analyzed separately, clusters of fired pads are identified and the information is translated to a global x-y coordinate for each potential hit. Each hit in the four tracking planes (pad chamber 1,2 and streamer tube 1,2; see Fig. 2) is characterized by the number of fired pads and the total charge in the cluster. In the second step, the tracks are found by straight-line fitting to the obtained hit coordinates in at least three of the four tracking planes.

Figure 5 shows the distribution at the vertical coordinate at the target for reconstructed tracks. The width of the distribution has contributions from the finite size of the target spot (roughly 5 mm), the vertical position resolution of the tracking chambers, multiple scattering and non- vertical components of the magnetic field. The restrictive trace-back to the target spot effectively eliminates background from secondary particles produced at the magnet poles, and also ensures reliable track recognition when only three tracking chambers register the track.

Some reconstructed clusters may be due to neutral particles (neutrons, γ- or X-rays). Although the detection probabilities for neutral particles are small in gaseous chambers, this background (which does not form tracks) is sizeable due to the large production crossection in heavy-ion collisions. Due to the good space resolution, allowing very restrictive definition of tracks, this background has not been any significant problem in the tracking.

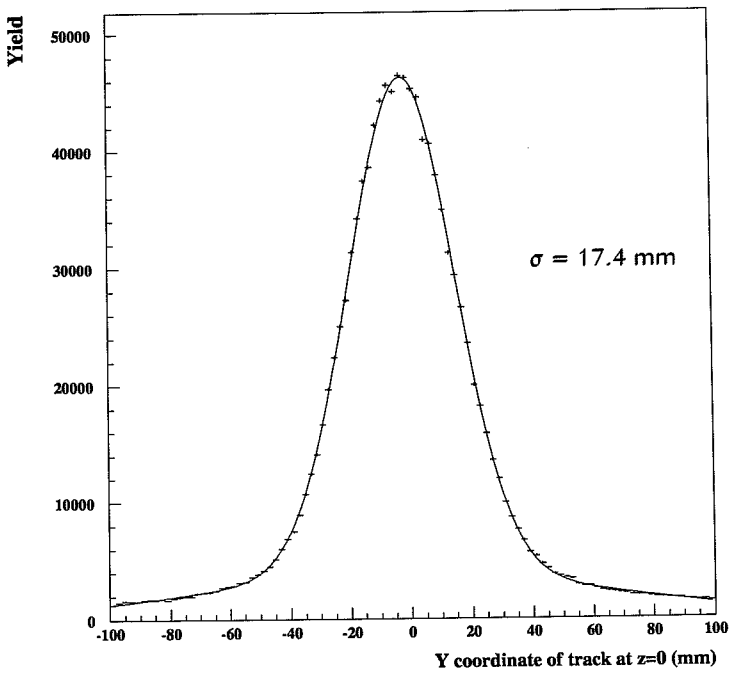

Figure 5: *Reconstructed target vertex (vertical projection), obtained by trace back of all found tracks to the z coordinate of the target.*

The high quality of the track finding is illustrated in Fig. 6 which shows the local efficiency over the area in pad chamber 1. The efficiency is determined by projecting all tracks with particle identification found by coordinates in pad chamber 2, streamer-tube detectors 1 and 2, into pad chamber 1. The probability that a hit is found in pad chamber 1, within a radius of 10 mm (based on the expected position resolution) around the predicted hit coordinate is calculated. The result is corrected for random hits.

The average efficiency over the whole chamber is about 85%. The apparent, general efficiency variation in x, is a consequence of the fluctuations

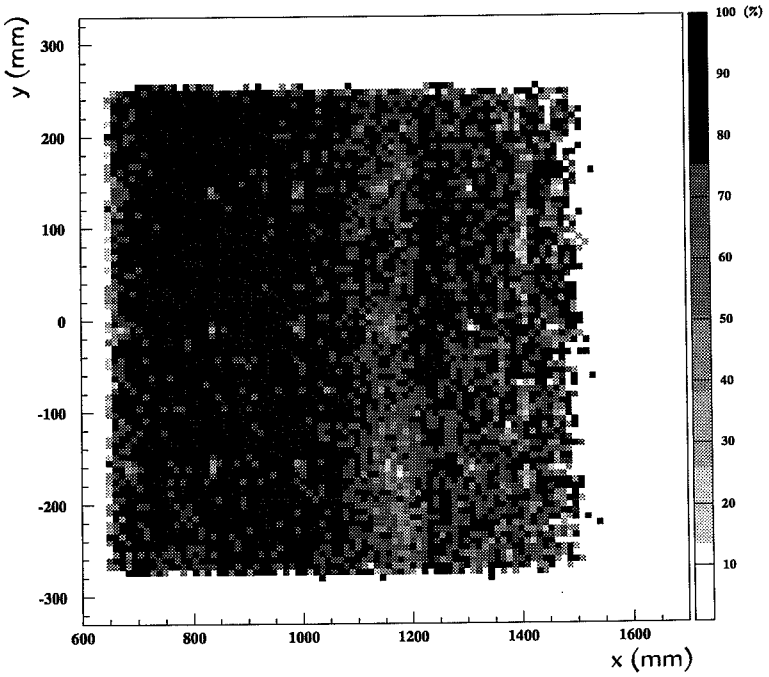

Figure 6: *The local efficiency of pad chamber 1. Black represents the highest efficiency. The reduced efficiency due to a spacer is e.g. seen at (840,140). The spacers form a regular pattern with a 15 cm spacing*

owing to decreasing statistics at large x (large angles). A real reduction in efficiency is observed around x=1150. This is due to unstable running conditions in the readout electronics.

The small white/grey spots (inactive areas) forming a regular pattern illustrate the tracking accuracy. These spots correspond to the positions in pad chamber 1 where the passage of the electron clouds are blocked by spacers between the meshes. The spacers are used to keep the meshes flat and parallel to each other to have a uniform response over the whole detector area. The chamber is thus insensitive at these spots.

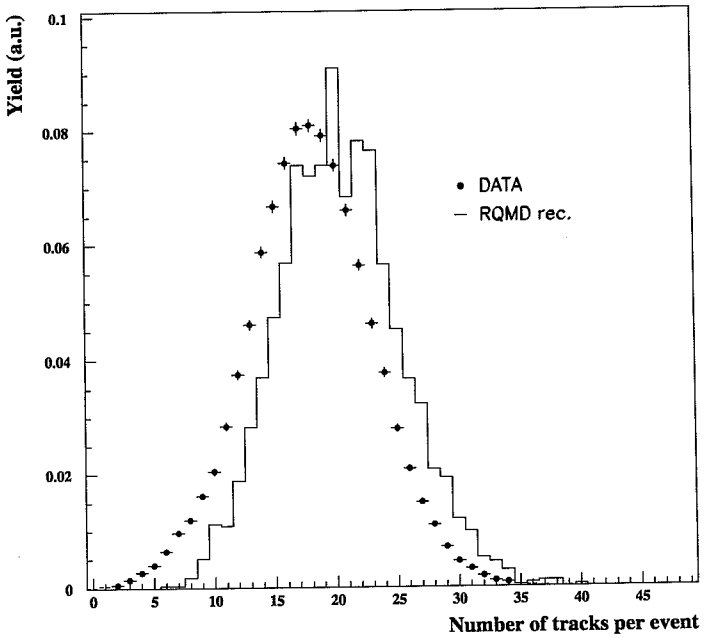

Figure 7: *The multiplicity of reconstructed tracks per event. Data are compared with RQMD events which were filtered through the GEANT acceptance and reconstructed in the same manner as data.*

To estimate the accidental background contribution to the track distribution, two different approaches were pursued. In the first one, an event-mixing technique was utilized. We used the hit information from the four tracking planes and the TOF wall from five different central events of approximately the same multiplicity to reconstruct the tracks. The same reduced χ^2 (< 2.5) and target-association cuts (± 50 mm, see Fig. 5) cuts were applied to the data as well as to the mixed events. It was observed that the contribution from the event-mix relative to data was less than 7% for three-chamber tracks and about 0.1% for four-chamber tracks. If we also require particle identification, the background contribution for three-chamber tracks is reduced to about 2%.

In the second approach, central Pb-Pb events from the RQMD[9] event generator were filtered through the acceptance of the GEANT[10] simulation package. The coordinates from charged pions, kaons and protons traversing at least three out of the four tracking planes and the TOF wall were saved and given as input to the WA98 analysis package. According to the measured average position resolution the hit positions were modified by a Gaussian smearing function, and fake clusters were added. Taking into account the measured chamber efficiencies, a number of good hits were deleted randomly before reconstructing tracks. The obtained number of reconstructed tracks per event is compared with data in Fig. 7. The same cuts as above for the χ^2 and target association have been applied. The track multiplicity from simulations differs from the data by about two tracks per event. The ratio between incorrectly and correctly reconstructed tracks from RQMD is about 7% for three-chamber tracks after these cuts, in agreement with what was found using the mixed event technique described above.

The data used to determine the tracking quality has been acquired with a trigger on central Pb-Pb collisions, i.e. with many tracks passing through the tracking system. Data was acquired at a rate of about 50 central events per second in spite of the very large number of detection channels (83 000). This was possible due to the powerful suppression of data from empty channels in parallel processing at an early stage of the data readout chain. The data rate corresponds to about 1000 recorded tracks per second. The major rate limitation in this experiment was the spark rate (about 1 spark per 100 events) in the pad chambers which had to be kept at a level where the balance between dead time after a spark and the amount of data collected was optimal.

4. Momentum determination and resolution

Using the direction vector of the found track, the momentum of the detected particle can be determined by tracing the track through the known magnetic field of the Goliath dipole-magnet (1.6 Tm). The GEANT simulation package was utilized to estimate the momentum resolution. Particles with known momenta were randomly generated at

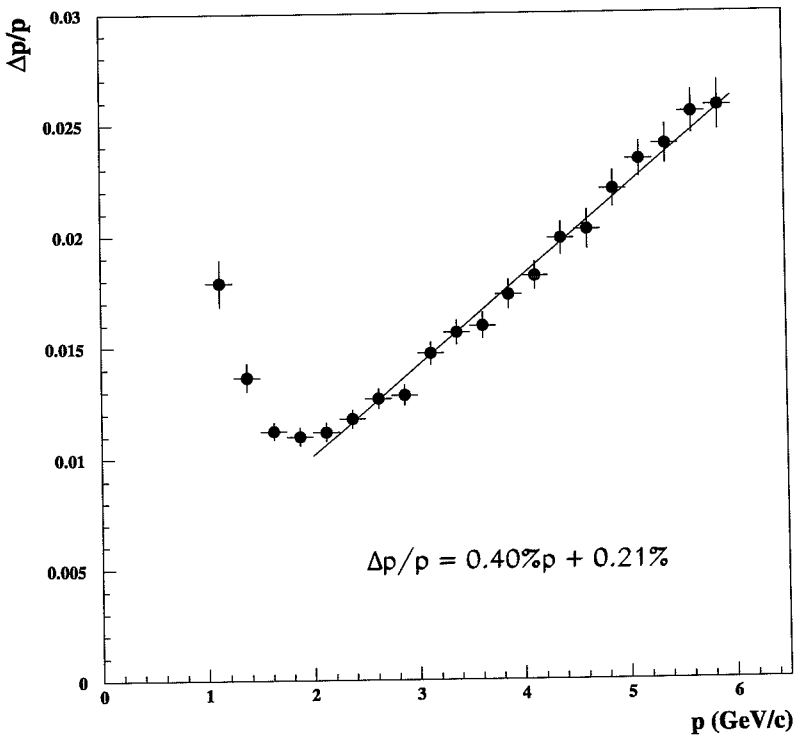

Figure 8: *The relative momentum resolution $\Delta p/p$ as a function of the particle momentum p.*

the target position. If the tracks passed through at least three out of the four tracking planes, the coordinates of the hits were stored. These coordinates, modified by a Gaussian smearing function according to the measured average position resolution of the different detectors, were then given as input to the WA98 analysis package including the measured magnetic-field map. The calculated relative momentum resolution $\Delta p/p$, in the momentum range $1 \leq p \leq 6$ GeV/c is shown in Fig. 8.

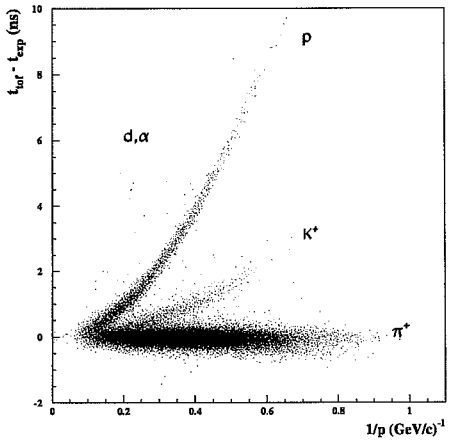

Figure 9: *The difference between the measured (t_{tof}) and expected time (t_{exp}), assuming pion mass as a function of the inverse momentum.*

5. Particle identification

The number of particles with multiple charge entering the tracking system is negligible. Thus particle identification can be restricted to mass separation among singly charged (negative or positive depending on the magnetic field orientation) particles. This is achieved by combining the information of the momentum and velocity measurements. The expected flight time was calculated from the track length (r_{track}), momentum and mass of the particle in the following way

$$t_{exp} = \frac{r_{track}}{c}\sqrt{1+(\frac{m_0 c}{p})^2} \qquad (1)$$

The expected time-of-flight t_{exp} has been calculated on basis of the reconstructed particle momentum assuming that all particles are pions. Among the positively charged particles one can recognize in Fig. 9 the bands of pions, kaons, protons and possibly deuterons inside the acceptance. The lightest particles, the pions, travel with almost the speed of light for all momenta inside the acceptance.

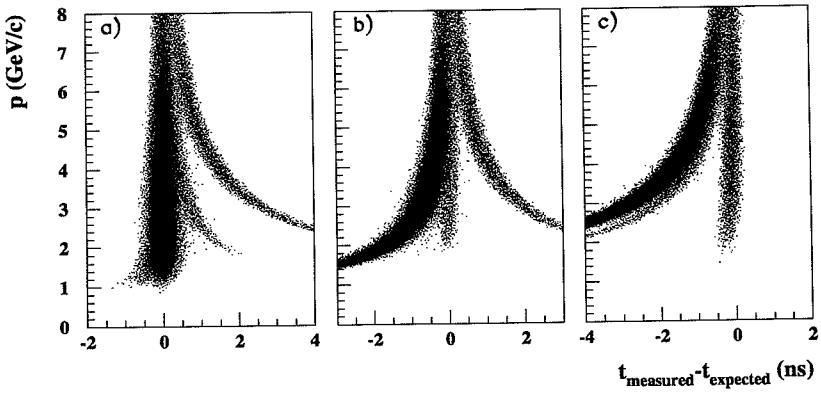

Figure 10: *Particle identification, exploiting the time-of-flight differences shown in Fig. 9 and assuming a) the pion mass, b) the kaon mass and c) the proton mass.*

For particle separation, cuts have been applied on the time-difference variable $(t_{tof} - t_{exp})$ which is calculated from the measured and expected time-of-flight. The flight-time differences for assumed pion (a), kaon (b) and proton (c) masses are shown in Fig. 10 as a function of the particle momentum. The correct particles are found in narrow bands at small time differences. Pions and kaons are no longer separable at momenta above 4 GeV/c. For correctly assumed particle identity the expected time equals the measured time independently of the momentum. From this observation we conclude that the time and momentum calibrations are consistent.

6. Two-track resolution

The fine granularity of the pad chambers allows good performance for tracks passing close to each other in a chamber. This property is of particular interest since some physics observables, e.g. the like-sign par-

ticle interferometry rely on accurate recording of particles with small momentum differences. Figure 11 shows the detection probability as a function of distance between the chamber coordinates in horizontal and vertical direction of an observed track and all other nearby tracks. The plateaus have been normalized to the average detection efficiency. The vicinity of tracks is defined in the x-direction within a narrow y-window ($\pm$17 mm) and in the y-direction within a narrow x-window ($\pm$2 mm). The resulting distribution of differences in the x-direction should be flat (except for physics effects of e.g. particle interference) if all tracks were recorded. Only tracks observed in all four tracking planes are included in this analysis. The resulting two-track resolution can be derived from Fig. 11. At 5 mm distance in the x-direction a track may be observed with 50% chance while the probability increases to the average detection efficiency at a distance of 7 mm. In the vertical direction the two-track resolution is worse due to the much longer pad dimension (17 mm). The momentum difference between two particles corresponding to the minimum distance 7 mm is about 2 and 13 MeV/c for pion pairs at 1 and 8 GeV/c respectively.

7. Acceptance

In a magnetic spectrometer the acceptance in momentum is the same for different particle masses of the same charge. The transverse momentum (p_T) and rapidity (y) are relevant kinematic observables in high-energy physics experiments. Expressed in these variables the regions of acceptance differ for different particle masses. This is a nuisance since one prefers to compare data at the same rapidity i.e. in the same kinematic regime which defines the source of the observed particles.

The particle-dependent acceptance regions are evident in Fig. 12 which shows the location in the $p_T - y$ plane for the different particle species. The sign(p_x) factor is introduced for clarification, as it unfolds the spectrum for particles with negative p_x and momentum low enough to bend over the beam line.

Inside each acceptance region the acceptance correction is strongly dependent on y and p_T as illustrated in Fig. 13 which shows the detection

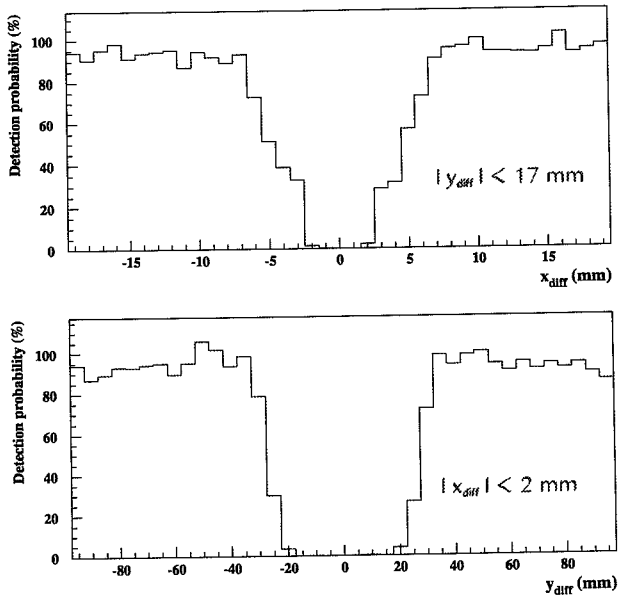

Figure 11: *The detection probability as a function of distance between the chamber coordinates in horizontal (upper panel) and vertical (lower panel) direction of an observed track and all other nearby tracks. The vicinity of tracks is defined by the indicated window in the respective other coordinate.*

probability for pions as it is simulated by GEANT. The acceptance correction can be qualitatively understood by considering particles with p_T near 0. For these particles, if the momentum is such that they enter the arm, the azimuthal coverage will be 2π. Particles with larger p_T, only weakly influenced by the magnetic field, will have an acceptance approaching the geometric azimuthal coverage of the tracking arm.

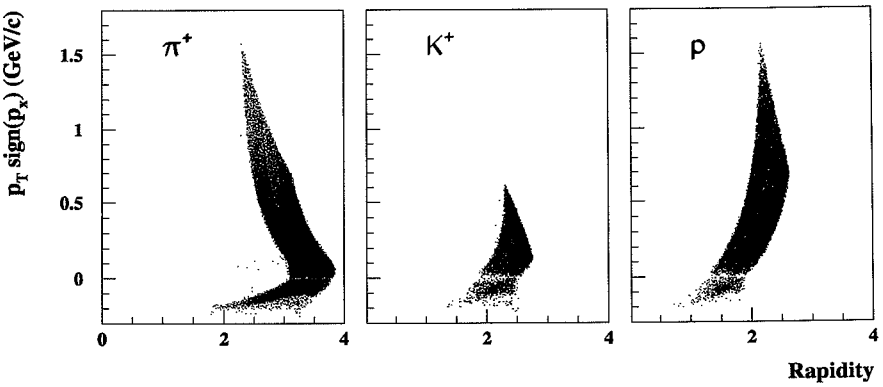

Figure 12: *Acceptance in terms of p_T and rapidity for pions, kaons and protons in data.*

8. Concluding remarks

The described tracking system covers a large detection area with four planes of space-point measuring tracking detectors and a high-resolution time-of-flight wall. The system has been exploited for data-taking in the 158 A GeV Pb-beam with typically 30 charged particles passing through the tracking system in a central Pb+Pb collision.

For the most central collisions, the track density at the small-angle side of the system approaches $100/m^2$ which is comparable to the expected situation in heavy-ion experiments at RHIC and LHC. The possibility to perform straight-line tracking at this particle density using only four space points along the track was demonstrated. Reliable tracking is achieved, in spite of the minimal redundancy, since each point is unambiguously determined and the coordinates are determined with high resolution in both dimensions which allows a restrictive track definition. The momentum resolution was in the range 1-3%. π/K separation was achieved up to 4 GeV/c and p/π separation up to 8 GeV/c.

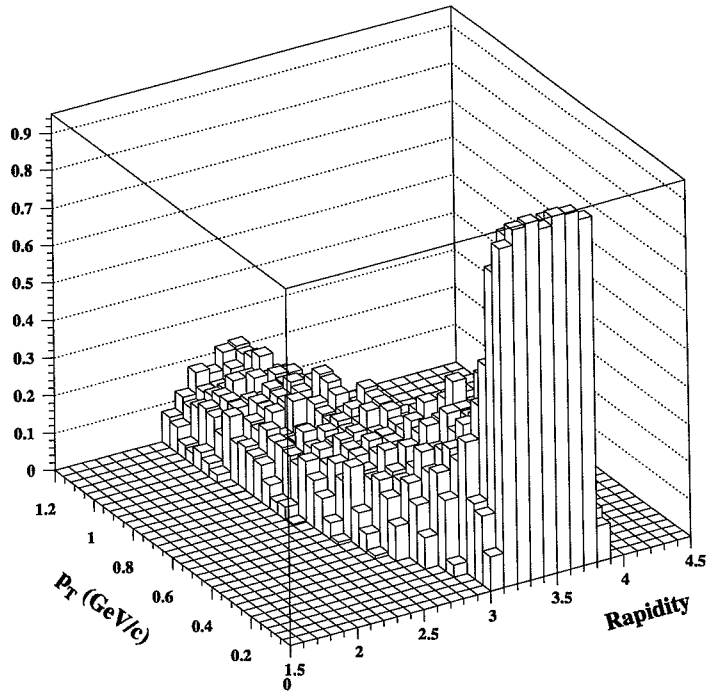

Figure 13: *Simulated detection probability in p_T versus rapidity due to geometrical acceptance for pions with positive p_x.*

The system has proven to produce reliable tracking results at high particle densities. The performance of found tracks and particle identification could be demonstrated already online. The offline analysis which is now in an advanced stage, has proven that high quality spectra of π, K, p and their respective antiparticles, can be obtained. Moreover, results on Δ^{++} and ϕ-meson production (together with arm 1) are obtainable as well as particle correlation studies between pairs of protons, kaons and pions.

Acknowledgments

This work was supported by the Swedish National Science Research Council (NFR), the Swedish Board for Planning and Coordination of Research (FRN), the Dutch Stichting voor Fundamenteel Onderzoek der Materie (FOM), the Swiss National Fund, the Japanese Grant-in-Aid for Scientific Research (Specially promoted Research & International Scientific Research) of the Ministry of Education, Science and Culture and the University of Tsukuba Special Research Projects, JSPS Research Fellowships for Young Scientists.

Bibliography

[1] M.M. Aggarwal et al. (WA98 collaboration), to be submitted (1999).

[2] L. Carlén et al., Nucl. Instr. and Methods A **391** (1997) 492.

[3] L. Carlén et al., Nucl. Instr. and Methods A **413** (1998) 92.

[4] L. Carlén et al., Nucl. Instr. and Methods A **412** (1998) 361.

[5] R. Albrecht et al., Z. Phys. C **55** (1992) 539.

[6] R. Albrecht et al., Nucl. Inst. and Methods A **276** (1989) 131.

[7] T. Chujo et al., Nucl. Instr. and Methods A **393** (1996) 409.

[8] PHENIX Conceptual Design Report, BNL 1993 (unpublished).

[9] H. Sorge, Phys. Rev. C **52** (1995) 3291.

[10] R. Brun and F. Carminati, *GEANT Detector Description and Simulation Tool*, CERN Program Library, Long Writeup W5013, March 1994.

Paper IV

Δ^{++} abundance in 158 A GeV ^{208}Pb+^{208}Pb interactions at the CERN SPS

M.M. Aggarwal,[1] A. Agnihotri,[2] Z. Ahammed,[3] A.L.S. Angelis,[4] V. Antonenko,[5] V. Arefiev,[6] V. Astakhov,[6] V. Avdeitchikov,[6] T.C. Awes,[7] P.V.K.S. Baba,[8] S.K. Badyal,[8] A. Baldine,[6] L. Barabach,[6] C. Barlag,[9] S. Bathe,[9] B. Batiounia,[6] T. Bernier,[10] K.B. Bhalla,[2] V.S. Bhatia,[1] C. Blume,[9] R. Bock,[11] E.-M. Bohne,[9] Z. Böröcz,[9] D. Bucher,[9] A. Buijs,[12] H. Büsching,[9] L. Carlen,[13] V. Chalyshev,[6] S. Chattopadhyay,[3] R. Cherbatchev,[5] T. Chujo,[14] A. Claussen,[9] A.C. Das,[3] M.P. Decowski,[18] H. Delagrange,[10] V. Djordjadze,[6] P. Donni,[4] I. Doubovik,[5] S. Dutt,[8] M.R. Dutta Majumdar,[3] K. El Chenawi,[13] S. Eliseev,[15] K. Enosawa,[14] P. Foka,[4] S. Fokin,[5] V. Frolov,[6] M.S. Ganti,[3] S. Garpman,[13] O. Gavrishchuk,[6] F.J.M. Geurts,[12] T.K. Ghosh,[16] R. Glasow,[9] S. K.Gupta,[2] B. Guskov,[6] H. Å.Gustafsson,[13] H. H.Gutbrod,[10] R. Higuchi,[14] I. Hrivnacova,[15] M. Ippolitov,[5] H. Kalechofsky,[4] R. Kamermans,[12] K.-H. Kampert,[9] K. Karadjev,[5] K. Karpio,[17] S. Kato,[14] S. Kees,[9] H. Kim,[7] B. W. Kolb,[11] I. Kosarev,[6] I. Koutcheryaev,[5] T. Krümpel,[9] A. Kugler,[15] P. Kulinich,[18] M. Kurata,[14] K. Kurita,[14] N. Kuzmin,[6] I. Langbein,[11] A. Lebedev,[5] Y.Y. Lee,[11] H. Löhner,[16] L. Luquin,[10] D.P. Mahapatra,[19] V. Manko,[5] M. Martin,[4] G. Martínez,[10] A. Maximov,[6] R. Mehdiyev,[6] G. Mgebrichvili,[5] Y. Miake,[14] D. Mikhalev,[6] Md.F. Mir,[8] G.C. Mishra,[19] Y. Miyamoto,[14] D. Morrison,[20] D. S. Mukhopadhyay,[3] V. Myalkovski,[6] H. Naef,[4] B. K. Nandi,[19] S. K. Nayak,[10] T. K. Nayak,[3] S. Neumaier,[11] A. Nianine,[5] V. Nikitine,[6] S. Nikolaev,[6] P. Nilsson,[13] S. Nishimura,[14] P. Nomokonov,[6] J. Nystrand,[13] F.E. Obenshain,[20] A. Oskarsson,[13] I. Otterlund,[13] M. Pachr,[15] A. Parfenov,[6] S. Pavliouk,[6] T. Peitzmann,[9] V. Petracek,[15] F. Plasil,[7] W. Pinganaud,[10] M.L. Purschke,[11] B. Raeven,[12] J. Rak,[15] R. Raniwala,[2] S. Raniwala,[2] V.S. Ramamurthy,[19] N.K. Rao,[8] F. Retiere,[10] K. Reygers,[9] G. Roland,[18] L. Rosselet,[4] I. Roufanov,[6] C. Roy,[10] J.M. Rubio,[4] H. Sako,[14] S.S. Sambyal,[8] R. Santo,[9] S. Sato,[14] H. Schlagheck,[9] H.-R. Schmidt,[11] Y. Schutz,[10] G. Shabratova,[6] T.H. Shah,[8] I. Sibiriak,[5] T. Siemiarczuk,[17] D. Silvermyr,[13] B.C. Sinha,[3] N. Slavine,[6] K. Söderström,[13] N. Solomey,[4] S.P. Sørensen,[20] P. Stankus,[7] G. Stefanek,[17] P. Steinberg,[18] E. Stenlund,[13] D. Stüken,[9] M. Sumbera,[15] T. Svensson,[13] M.D. Trivedi,[3] A. Tsvetkov,[5] L. Tykarski,[17] J. Urbahn,[11] E.C.v.d. Pijll,[12] N.v. Eijndhoven,[12] G.J.v. Nieuwenhuizen,[18] A. Vinogradov,[5] Y.P. Viyogi,[3] A. Vodopianov,[6] S. Vörös,[4] B. Wysłouch,[18] K. Yagi,[14] Y. Yokota,[14] G.R. Young[7]

(WA98 Collaboration)

[1] *University of Panjab, Chandigarh 160014, India*
[2] *University of Rajasthan, Jaipur 302004, Rajasthan, India*
[3] *Variable Energy Cyclotron Centre, Calcutta 700 064, India*
[4] *University of Geneva, CH-1211 Geneva 4,Switzerland*
[5] *RRC "Kurchatov Institute", RU-123182 Moscow, Russia*
[6] *Joint Institute for Nuclear Research, RU-141980 Dubna, Russia*
[7] *Oak Ridge National Laboratory, Oak Ridge, Tennessee 37831-6372, USA*
[8] *University of Jammu, Jammu 180001, India*
[9] *University of Münster, D-48149 Münster, Germany*
[10] *SUBATECH, Ecole des Mines, Nantes, France*
[11] *Gesellschaft für Schwerionenforschung (GSI), D-64220 Darmstadt, Germany*
[12] *Universiteit Utrecht/NIKHEF, NL-3508 TA Utrecht, The Netherlands*
[13] *Lund University, SE-221 00 Lund, Sweden*
[14] *University of Tsukuba, Ibaraki 305, Japan*
[15] *Nuclear Physics Institute, CZ-250 68 Rez, Czech Rep.*
[16] *KVI, University of Groningen, NL-9747 AA Groningen, The Netherlands*
[17] *Institute for Nuclear Studies, 00-681 Warsaw, Poland*
[18] *MIT Cambridge, MA 02139, USA*
[19] *Institute of Physics, 751-005 Bhubaneswar, India*
[20] *University of Tennessee, Knoxville, Tennessee 37966, USA*

Abstract

The Δ^{++}-resonance production in (158 A GeV) ^{208}Pb+^{208}Pb collisions at the CERN SPS has been studied. The Δ^{++} production was estimated from the invariant mass spectrum of $p\pi^+$-pairs by subtracting a mixed event background. The abundance of Δ^{++} in central collisions is compared with a thermodynamical model and other experiments at lower energies.

1. Introduction

The best way to study nuclear matter under extreme conditions in the laboratory seems to be through energetic heavy-ion collisions. It has been suggested that some of the particles or resonances produced in such collisions may have a memory of the early stages of the interaction, where temperatures and densities are considerably larger than in normal nuclear matter. Some particles may thus have properties that differ from those observed under normal circumstances.

One of those objects is the Δ-resonance, which apart from playing a role in particle production and interaction dynamics, may probe the conditions in heavy-ion collisions at early freeze-out times and high freeze-out densities.[1] The Δ-resonance is known to be readily produced in photon[2]- lepton[3]- and hadron[4]- induced nuclear interactions and the cross sections for production of Δ-resonances in elementary nucleon-nucleon collisions are large[5]. In heavy ion collisions the $\Delta(1232)$ resonances are thus expected to be formed in the early, compressed stage of the collision.

Recently, results on $\Delta(1232)$ production in nucleus-nucleus collisions at 95 A MeV (GANIL[6]), at 1 and 2 A GeV (FOPI collaboration SIS/GSI[7]) and at 13.7 A GeV (E814 collaboration AGS[8]) have been reported.

2. Experimental procedures

The fixed target experiment WA98[9] is a large-acceptance photon and hadron spectrometer designed to study ultra-relativistic heavy-ion collisions. Charged particles, produced in the interactions traverse a large magnet and are deflected into two tracking arms, horizontally placed on both sides of the beam which allow for momentum determination and particle identification. For the Δ^{++} measurements, reported in this paper, we use data from the second tracking arm which focuses on positively charged particles. This tracking arm consists of two planes of Multi-Step Avalanche Chambers (MSACs) and two planes of streamer

tube detectors, all equipped with electronic pad readout and a highly segmented Time-Of-Flight (TOF) wall.[10, 11, 12] Figure 1 a) shows a schematic drawing of the second tracking arm as seen from above, with two tracks entering the acceptance. Here the z-axis is pointing along the beam and the x-axis is parallel to the bending plane of the magnet. The position resolution of the MSACs were σ_x=0.5 mm in the horizontal direction, and σ_y=1.7 mm in the vertical direction whereas the streamer tube detectors had an intrinsic resolution of σ_x=3.0 mm and σ_y=6.5 mm. The time resolution of the TOF wall was better than 90 ps and its spatial resolution was σ_x=12.5 mm and σ_y=26.4 mm. Figure 1 b) and 1 c) show p versus $t_{tof} - t_{exp}$ assuming pion and proton mass, respectively. p is the momentum, t_{tof} the measured flight time of the particle and t_{exp} the expected flight time calculated from the track length and momentum of the particle. Separation between different particle species, especially for pions and protons, is good over a wide range of momentum. Kaons and pions are no longer separable at momentum above 4 GeV/c. We thus have a small contamination of kaons among the pions at larger momenta since we use pions and protons up to 8 GeV/c in the analysis. First, the momenta of the particles are calculated assuming a uniform magnetic field and straight line fits through the tracking arm. The momenta are then iteratively corrected using GEANT[13] simulations with the real field. The momentum resolution, $\Delta p/p$, is limited by the multiple scattering in the air between the target and the detectors, the intrinsic detector resolution and by the uncertainties in the momentum reconstruction. Based on GEANT simulations we estimate $\Delta p/p$ to be about 1% at 2 GeV/c and 2% at 5 GeV/c.

The most interesting events are those where the bulk of the nuclear matter interacts, i.e. the most central events. A trigger based on the transverse energy as measured by the Mid-Rapidity Calorimeter (MIRAC) is used to enhance central collisions. The trigger selects about 10% of the most central events. This hardware selection is combined with a software transverse energy cut at 326 GeV. To reject beam particles with charge different from Pb and possible event pile-up, lower and upper cuts in the ADC and TDC values from the start-counters, placed in the beam, were performed.

During and shortly after electrical discharges, the MSACs exhibited re-

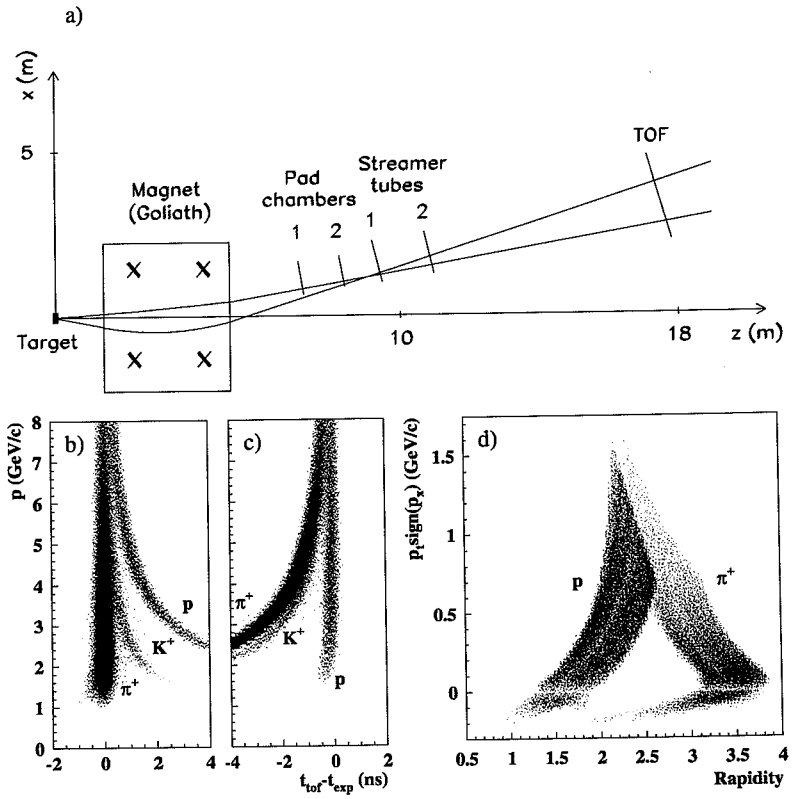

Figure 1: a) *Overview of the tracking arm with two tracks within the acceptance.* b) *Particle identification bands calculated assuming that all particles have the pion mass.* c) *as in* b) *assuming proton mass.* d) *The geometrical acceptance in terms of* p_t *and rapidity for protons and* π^+.

duced efficiencies. This has been discussed in a previous paper.[10] Thus events recorded within a short time after such a discharge, are removed from the analysis.

The tracking procedure connects hits in at least three out of four tracking planes, by means of straight line fits, and combines a track with a valid time measurement in the TOF wall at the correct position. Due to the excellent two-track resolution and two-dimensional position resolution of the tracking planes, this procedure works well without any ambigui-

ties in spite of the large track multiplicity within the acceptance. Cuts have been applied on the hit association in the TOF wall and on the vertical distance between the track extrapolation and the interaction point. Finally the particle identity is obtained by cuts in the $t_{tof} - t_{exp}$ up to momentum 8 GeV/c, where the separation no longer can be done as seen in Fig. 1 b) and c). At momentum larger than 4 GeV/c no separation between kaons and pions is possible. The small amount of contaminating kaons give only marginal effects on the extracted Δ^{++} yield and the contamination is also present in the event mix.

Figure 1 d) shows the geometrical acceptance of the second tracking arm in terms of transverse momentum p_t and rapidity for protons and pions. Notice the sign(p_x) factor introduced for clarification, which unfolds the spectrum for particles with negative p_x and momentum low enough to bend over the beam line.

Although the tracking efficiency in the four tracking planes was about 90%, technical problems with the time measurement in the TOF wall reduced the particle identification efficiency considerably.

For all pairs of identified p and π^+, the invariant mass, M_{inv}, was calculated from

$$M_{inv} = \sqrt{(E_\pi + E_p)^2 - (\overline{p}_\pi + \overline{p}_p)^2}$$

The mass resolution of the pπ^+-pair, estimated from the momentum resolution, is 10-20 MeV. An invariant mass spectrum of such pairs (real spectrum) will consist of one part where the pion and the proton are coming from the same Δ^{++}-decay and an essentially uncorrelated combinatorial background. Due to the high multiplicity of protons and pions, the combinatorial background will be by far the dominant contribution to the invariant mass spectrum. To account for this combinatorial background, the invariant mass spectrum was calculated also with protons and pions taken from different events (mixed event). To extract the fraction ξ, of Δ^{++}, $N_{\Delta++}$, among the pπ^+-pairs, N_{pair}, we assume that the mixed event invariant mass spectrum has the same shape as the combinatorial background in the real spectrum. This assumption has been verified by studies of ratios between real spectra and mixed event spectra. To reduce the statistical errors, the mixed event spectrum contains about ten times the statistics in that of the real spectrum. The

real spectrum, $F(M_{inv})$ can then be written as

$$F(M_{inv}) = N_{ev} \cdot N_{pair}(\xi \cdot BW(M_{inv}, M_0, \Gamma) + (1-\xi)g(M_{inv})) \quad (1)$$

BW(M_{inv}, M_0, Γ) is a modified Breit-Wigner function, corrected for our geometrical acceptance, normalized to unity. M_0 and Γ are the peak position and width respectively of the modified Breit-Wigner function. Note that neither the real spectrum nor the mixed event spectrum are corrected for acceptance. N_{ev} is the number of events and $g(M_{inv})$ is the unit normalized mixed event spectrum. The modified Breit-Wigner function is given by

$$BW(M_{inv}, M_0, \Gamma) \propto \frac{q^3}{(q^3+\mu^3)} \frac{1}{((M_{inv}-M_0)^2 + (\Gamma/2)^2)}$$

where q is the momentum of the proton (or pion) in the rest-frame of the pair and μ=180 MeV/c.[14] The real spectrum can now be fitted using Eq. 1, treating ξ, M_0 and Γ as free parameters.

Figure 2 a) shows the geometrical acceptance for Δ^{++} obtained from FRITIOF[15] events filtered through GEANT, i.e. for Δ^{++} where both decay particles fall inside the acceptance of the arm. The spectrum is unfolded in the same way as in Fig. 1 d). Figure 2 b) shows the invariant mass spectrum of

$$F(M_{inv}) - N_{ev} \cdot N_{pair} \cdot (1-\xi)g(M_{inv}),$$

i.e. the real spectrum with the background subtracted. Also shown is

$$N_{ev} \cdot N_{pair} \cdot \xi \cdot BW(M_{inv}, M_0, \Gamma),$$

i.e. the acceptance-corrected modified Breit-Wigner function obtained from the best fit.

3. Results

The extracted number of Δ^{++} has to be corrected for acceptance and inefficiencies. Table 1 summarizes the different correction factors and the final results. k_{eff} for Δ^{++} is the probability for both the pion and proton

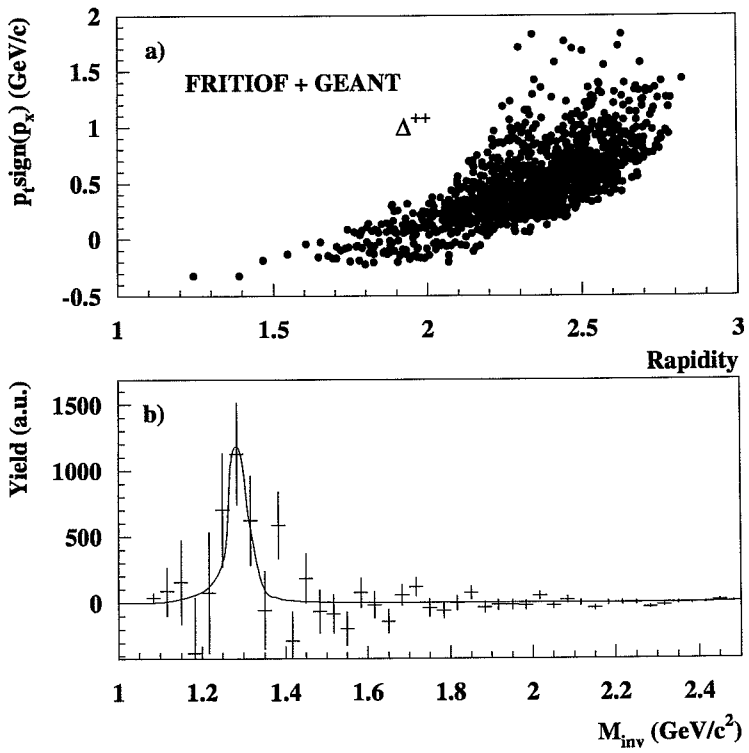

Figure 2: a) *The geometrical acceptance for* Δ^{++} *obtained from Fritiof events.* b) *The extracted* Δ^{++} *resonance together with the corresponding acceptance-corrected modified Breit-Wigner.*

from the Δ^{++}, entering the arm, to result in valid tracks. k_{eff} for Δ^{++} is obtained as the product of the efficiency factors for protons and pions, which are the same. The k_{geo} factors correct for the limited azimuthal coverage of the arm estimated by GEANT simulations. Finally the k_{pid} factors relate to the above mentioned inefficiencies in the TOF wall.

Table 1 also gives the corrected number of protons and Δ^{++} within the arm and for full azimuthal coverage. Within our acceptance RQMD2.3[16]

119677 Central events	Protons	Δ^{++}
Particles observed	120906	2461±1105
Particles/Event (uncorrected)	1.01027	0.02056
Tracking efficiency, k_{eff}	0.8777	0.7704
Identification efficiency, k_{pid}	0.6168	0.3804
Particles/Event (eff. corrected)	1.8662	0.0702
Geometrical acceptance, k_{geo}	0.1127	0.0163
Particles/Event (full ϕ)	16.56	4.30

Table 1: *Summary of the different correction factors and results.*

predicts about 2.4 protons/central event and FRITIOF7.02 predicts about 5.5 protons/central event. Thus our proton multiplicities seem to be in good agreement with RQMD, whereas FRITIOF seems to overestimate. Only a small contribution of baryon number is present in deuterons and weakly decaying hyperons, where the decay proton might be lost in the tracking due to the secondary vertex being far from the interaction point.

The extraction of the Δ^{++} signal is by no means trivial as the peak is broad and the combinatorial background is large. Three different extraction methods were applied to simulated data to investigate the influence of the methods on the reconstructed number of Δ^{++}.[17] The method described above proved to be the most robust for different projectiles p, Si and Pb upon Pb target at the relevant beam energy.

4. Discussion and conclusions

The ratio of $\Delta(1232)$/nucleons has been studied and an increase as a function of incoming beam energy has been established.[7] In a thermal model this can be interpreted as an increase of the freeze-out temperature which determines the relative population of the nucleonic resonances. The same ratio can be estimated from our data. To obtain the total number of $\Delta(1232)$ resonances, i.e. Δ^{-}, Δ^{0}, Δ^{+} and Δ^{++}, we multiply the number of Δ^{++} by an isospin factor 4. In the same way,

the number of nucleons, including those from resonance decays, can be estimated by multiplying the measured number of protons with a factor two. No correction for the isospin assymetri is applied, since this, in a first approximation, affects the nucleons and the Δ-resonances in the same way. The $\Delta(1232)$/nucleons ratio obtained from our analysis is 0.52, i.e. 52% of the nucleons at central rapidities originate from a $\Delta(1232)$ resonance. Figure 3 shows our results in comparison with similar results from experiments at lower beam energies. Note that the target and projectile rapidities are separated by 5.8 units at 158 A GeV. In this experiment the influence of spectator matter is thus much less than at lower beam energies.

Regarding the statistical error of the found ratio we would like to point out that this is to the first order given by the statistical fluctuations in the number of combinatorial pairs under the resonance peak. In our case this error coincides with the error obtained in the fitting procedure. It is thus impossible to obtain the ratio with higher accuracy with the given statistics, independent of the extraction method used. It should also be pointed out that the error reported in [8] for the 14.6 A GeV data (here we use their error given for the absolute number of Δ^{++} found) is smaller than the error estimated from their combinatorial background.

A study of the systematic errors introduced, based on event generators, extraction methods and variation of cuts implied on the data, reveals that they are considerably smaller than the obtained statistical errors. The systematic errors can thus be neglected in the results.

Our obtained value of the $\Delta(1232)$/nucleon ratio can be compared to the ratio obtained from thermal model calculations, assuming chemical and thermal equilibrium. In such a calculation the maximum ratio obtained is around 0.33.[18] Furthermore this ratio is obtained over a large range of temperatures and baryon densities, used as input to the calculations. It should however be pointed out that the experimental ratio contains, apart from those $\Delta(1232)$ accounted for by the model, present at freeze-out, also some $\Delta(1232)$ decaying prior to freeze-out. An experimental ratio larger than the calculated one is thus to be expected. For this and other reasons, e.g. the saturation of the ratio as a function of temperature, it is premature to use the experimentally extracted ratio for

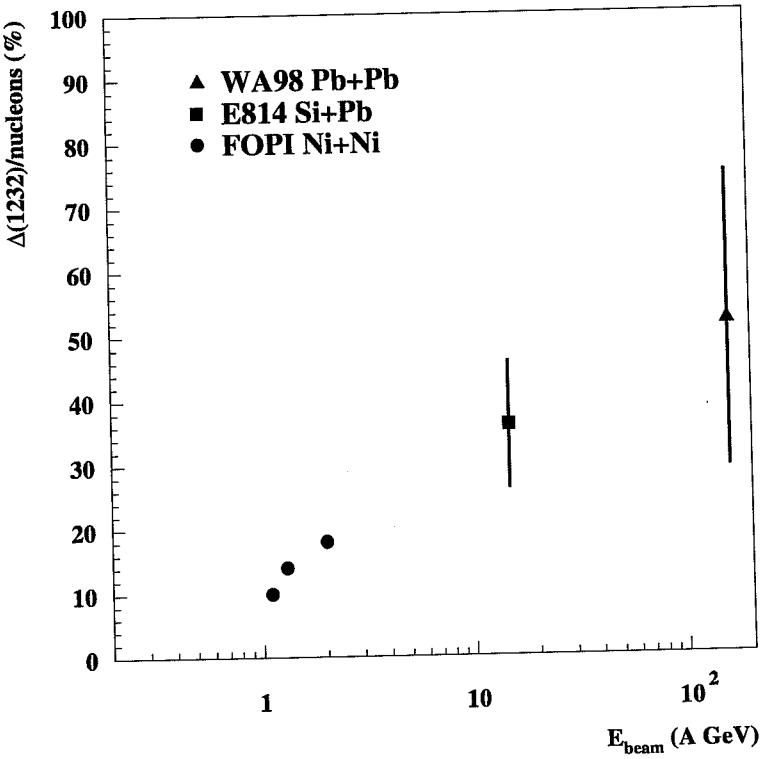

Figure 3: *The ratio* $\Delta(1232)$*/nucleons as a function of beam energy/nucleon.*

a precise temperature estimation and any temperature above 120 MeV seems to be in qualitative agreement with the obtained ratio.

Acknowledgements

This work was supported jointly by the German BMBF and DFG, the U.S. DOE, the Swedish NFR and FRN, the Dutch Stichting FOM, the Stiftung für Deutsch-Polnische Zusammenarbeit, the Grant Agency of

the Czech Republic under contract No. 202/95/0217, the Department of Atomic Energy, the Department of Science and Technology, the Council of Scientific and Industrial Research and the University Grants Commission of the Government of India, the Indo-FRG Exchange Program, the PPE division of CERN, the Swiss National Fund, the INTAS under Contract INTAS-97-0158, ORISE, Grant-in-Aid for Scientific Research (Specially Promoted Research & International Scientific Research) of the Ministry of Education, Science and Culture, the University of Tsukuba Special Research Projects, and the JSPS Research Fellowships for Young Scientists. ORNL is managed by Lockheed Martin Energy Research Corporation under contract DE-AC05-96OR22464 with the U.S. Department of Energy. The MIT group has been supported by the US Dept. of Energy under the cooperative agreement DE-FC02-94ER40818.

Bibliography

[1] S.A. Bass et al., Phys. Rev. C **50** (1994) 2167.

[2] J.M. Laget, Phys. Rep. **69** (1981) 1.

[3] J.S. O'Connell and B. Schroöder, Phys. Rev. C **38** (1988) 2447.

[4] R.E. Chrien et al., Phys. Rev. C **21** (1980) 1014.

[5] J.P. DeBrion et al., Phys. Rev. Lett. **34** (1975) 910.

[6] A. Badalà et al., Phys. Rev. C **54** (1996) R2138.

[7] B. Hong et al. (FOPI collaboration), Phys. Lett. B **407** (1997) 115.

[8] J. Barrette et al. (E814 collaboration), Phys. Lett. B **351** (1995) 93.

[9] WA98 collaboration, *Proposal for a large acceptance hadron and photon spectrometer*, 1991, Preprint CERN/SPSLC 91-17, SPSLC/P260.

[10] L. Carlén et al., Nucl. Instr. and Methods A **412**, (1998) 361.

[11] L. Carlén et al., Nucl. Instr. and Methods A **413**, (1998) 92.

[12] L. Carlén et al., submitted to Nucl. Instr. and Methods A.

[13] R. Brun and F. Carminati, *GEANT Detector Description and Simulation Tool*, CERN Program Library, Long Writeup W5013, March 1994.

[14] E.L. Hjort et al. , Phys. Rev. Lett. E **79** (1997) 4345.

[15] B. Nilsson-Almqvist and Evert Stenlund, Comp. Phys. Comm. **43** (1987) 387.

[16] H. Sorge, Phys. Rev. C **52** (1995) 3291.

[17] K. El Chenawi, PhD thesis, Lund University, 1999.

[18] G.E. Brown, J. Stachel and G.M. Welke, Phys. Lett. B **253** (1991) 19.